DISS. ETH NO. 23291

Experimental study on collision efficiency and contact freezing

A thesis submitted to attain the degree of

DOCTOR OF SCIENCES of ETH ZURICH

(Dr. sc. ETH Zurich)

presented by

BABAN NAGARE

M. Sc., University of Pune
born on 9 September 1982
citizen of India

accepted on the recommendation of

Prof. Dr. Ulrike Lohmann, examiner
Prof. Dr. Thomas Leisner, co-examiner
Dr. Claudia Marcolli, co-examiner

2016

To Bai, Appa and family

Abstract

Atmospheric ice nucleation determines the number concentration of ice crystals and their sizes. These microphysical properties are responsible for the cloud optical thickness, cloud lifetime and precipitation efficiency of the clouds. In mixed phase clouds between temperatures of 237 K and 273 K, ice forms with the help of ice nucleating particles (INPs) by heterogeneous nucleation. Contact freezing is least understood amongst the known heterogeneous mechanisms of ice nucleation. To understand the microphysical properties of mixed phase clouds, contact freezing may be one of the key elements because it is reported to occur at higher temperatures than other heterogeneous mechanisms of ice formation. However, it is not clear whether the collision process itself or the position of the INP on the surface of the droplet leads to the enhancement of freezing efficiency.

Quantifying contact freezing necessitates the knowledge of the collision efficiencies between droplets and INPs for mixed phase cloud temperatures. The collision efficiency between droplets and INPs was determined with contact freezing experiments using the ETH Zurich CoLlision Ice Nucleation CHamber (CLINCH). Collision efficiency was determined for 80 μm diameter droplets and 200 and 400 nm silver iodide particles as INPs by observing the frozen fraction of droplets for different concentrations of INPs and two different residence times of the droplets in the chamber. The upper and lower range of the collision efficiency for 800 nm kaolinite particles was also estimated. A brief review of theoretical models for collision efficiency is provided and the theoretical collision efficiency is compared with the experimentally determined collision efficiencies for mixed phase cloud temperatures. Experimentally determined collision efficiency was found to be an order of magnitude higher than the theoretical one. Theoretical schemes were developed and applied mostly for rain conditions at T $>$ 0 °C. This thesis provides the first dataset of collision efficiencies acquired below 273 K. More such experiments with different droplet and particle diameters are needed to improve our understanding of collision processes acting together.

To understand the relative importance between immersion freezing and contact freezing, the comparison between freezing efficiencies is provided for silver iodide, ATD and kaolinite particles. The frozen fraction of droplets by contact freezing was observed at two different residence times of the droplets in the chamber for 200 nm silver iodide, 400 and 800 nm kaolinite and ATD particles. The freezing efficiencies for contact freezing were calculated by estimating the number of collisions between the droplets and particles using the collision efficiency determined in the first part of this thesis. This efficiency is compared with the immersion freezing efficiency from the IMCA/ZINC chamber. The experiments show that silver iodide particles produced by our method are much less efficient in terms of onset temperature for contact freezing than for immersion freezing. ATD particles showed

similar onset temperatures in both freezing modes while 800 nm kaolinite particles showed 3 K higher onset temperature in contact mode. For ATD and kaolinite particles, freezing efficiencies in CLINCH determined at 2 s residence time were smaller than at 4 s, which is in disagreement with a collisional contact freezing process but in accordance with contact freezing inside-out or immersion freezing.

Zusammenfassung

Atmosphärische Eisnukleation bestimmt die Anzahlkonzentration von Eiskristallen und ihre Grösse. Diese beiden mikrophysikalischen Variablen wiederum bestimmen die optische Dichte von Wolken, ihre Lebenszeit und ihre Niederschlagseffizienz. In Mischphasenwolken mit einer Temperatur zwischen 237 und 273 K findet Eisbildung durch heterogene Nukleation an Eiskeimen statt. Kontaktgefrieren ist der am wenigsten verstandene Prozess unter den bekannten heterogenen Eisbildungsmechanismen. Er könnte einer der Schlüsselelemente zum Verständnis der mikrophysikalischen Eigenschaften einer Mischphasenwolke sein, da er schon bei höheren Temperaturen als andere heterogene Eisbildungsmechanismen stattfindet. Es ist allerdings nicht klar, ob der Kollisionsprozess selber oder ob die Position des Eiskeims auf der Oberfläche des Tröpfchens zu einer Erhöhung der Gefriereffizienz führt.

Die Quantifizierung von Kontaktgefrieren erfordert die Kenntnis der Kollisionseffizienz zwischen den Tröpfchen und den Eiskeimen bei Mischphasentemperaturen. Die Kollisionseffizienz zwischen Tröpfchen und Eiskeimen wurde durch Kontaktgefrierexperimente mit der ETH Zürich Eisnukleationskammer CLINCH bestimmt. Die Kollisionseffizienz wurde für Tröpfchen mit einem Durchmesser von 80 μm und Silberiodidpartikel als Eiskeim mit einem Durchmesser von 200 und 400 nm durch Beobachtung der Gefrierfraktion der Tröpfchen bei verschiedenen Eiskeimkonzentrationen und zwei verschiedenen Aufenthaltsdauern in der Kammer ermittelt. Es wurde auch die Ober- und Untergrenze der Kollisionseffizienz für Kaolinitpartikel mit einem Durchmesser von 800 nm bestimmt. Theoretische Modelle zur Kollisionseffizienz werden kurz zusammengefasst und die theoretische Kollisionseffizienz experimentell ermittelten Werten für Mischphasentemperaturen gegenübergestellt. Die experimentell bestimmte Kollisionseffizienz ist eine Grössenordnung grösser als die theoretische. Die theoretischen Modelle wurden meistens für Niederschlagsbedingungen bei Temperaturen über 0 °C entwickelt und angewendet. Diese Arbeit dagegen enthält den ersten Datensatz von Kollisionseffizienzen unter erworben 273 K. Noch mehr solcher Experimente mit verschiedenen Tröpfchen- und Eiskeimgrössen werden gebraucht, um unser Verständnis über Kollisionsprozesse zu verbessern.

Um zu verstehen wie wichtig Immersionsgefrieren und Kontaktgefrieren relativ zueinander sind, wird die Gefriereffizienz dieser beiden Prozesse für drei verschiedene Eiskeime (Silberiodid, ATD und Kaolinite) miteinander verglichen. Die Gefrierfraktion der Tröpfchen durch Kontaktgefrieren wurde für zwei verschiedene Aufenthaltsdauern in der Kammer für Silberiodidpartikel mit einem Durchmesser von 200 nm, Kaolinitpartikel und ATD-Partikel mit einem Durchmesser von 400 und 800 nm beobachtet. Die Gefriereffizienz von Kontaktgefrieren wurde berechnet indem die Anzahl der Kollisionen zwischen Tröpfchen und Partikel mit der Kollisionseffizienz aus dem 1. Teil dieser Arbeit

bestimmt wurde. Diese Effizienz wird mit der Gefriereffizienz von Immersionsgefrieren aus Experimenten mit der IMCA/ZINC Kammer verglichen. Die Kontaktgefrierexperimente zeigen, dass mit unserer Methode produziertes Silberiodid im Vergleich zum Immerionsgefrieren sehr viel weniger effizient ist, wenn man die Temperatur vergleicht, bei der Gefrieren einsetzt. ATD Partikel zeigen in beiden Gefriermoden eine ähnliche Temperatur, bei der Gefrieren einsetzt, während 800 nm Kaolinitpartikel im Kontaktgefrierfall bei 3 K höheren Temperaturen anfangen zu gefrieren. Bei den ATD und Kaolinitpartikeln sind die Gefriereffizienzen, die mit CLINCH bestimmt wurden, kleiner bei einer Aufenthaltsdauer von 2 s im Vergleich zu 4 s. Das widerspricht dem Kollisionskontaktgefrierprozess, wäre aber in Übereinstimmung mit dem Kontaktgefrierprozess von innen nach aussen (“inside-out”) oder Immersionsgefrieren.

Contents

Abstract v

Zusammenfassung vii

1 Introduction 1
- 1.1 Atmospheric aerosol and climate . . . 1
- 1.2 Clouds in the climate system . . . 2
- 1.3 Ice nucleation in the atmosphere . . . 3
  - 1.3.1 Homogeneous ice nucleation . . . 4
  - 1.3.2 Heterogeneous ice nucleation . . . 7
- 1.4 Contact freezing . . . 9
- 1.5 Outline of the thesis . . . 12

2 The Collision Ice Nucleation Chamber 15
- 2.1 Instrument details . . . 15
- 2.2 Ice optical Detector (IODE) . . . 16
- 2.3 Droplet size evolution in CLINCH . . . 19
- 2.4 Collision efficiency . . . 20
- 2.5 Droplet size sensitivity of E and N . . . 24
- 2.6 Other instruments . . . 24

3 Comparison of measured and calculated collision efficiencies at low temperatures 27
- 3.1 Introduction . . . 27
- 3.2 Theory . . . 29
  - 3.2.1 Collision efficiency . . . 29
  - 3.2.2 Brownian diffusion, interception and impaction . . . 30
  - 3.2.3 Phoretic forces . . . 33
- 3.3 Experimental setup . . . 35
  - 3.3.1 Instrumentation . . . 35
  - 3.3.2 Aerosol preparation . . . 36
  - 3.3.3 Charge measurement . . . 37
  - 3.3.4 Experimental procedure . . . 38
- 3.4 Experimental results . . . 38

3.5 Comparison of the different formulations of collision efficiency 40
3.5.1 Temperature dependence of thermophoretic collision efficiency 42
3.5.2 Charge dependence of electrophoresis 43
3.5.3 The total collision efficiency E_{Tot} 45
3.6 Comparison with previous experimental work 45
3.7 Discussion 47
3.7.1 Discrepancies between theoretical and experimentally derived collision efficiencies 47
3.7.2 Implications for contact freezing 49
3.7.3 Implications for atmospheric aerosol scavenging 50
3.8 Summary and conclusions 51

4 Comparing contact and immersion freezing from continuous flow diffusion chambers 53
4.1 Introduction 53
4.2 Experimental setups and procedures 56
4.2.1 Instrument description 56
4.2.2 Aerosol generation and sampling 57
4.2.3 Particle sprinkling experiment 57
4.3 Experimental results 57
4.4 Freezing efficiencies 59
4.4.1 Calculation of freezing efficiency from frozen fraction 59
4.4.2 Freezing efficiency of silver iodide particles 61
4.4.3 Freezing efficiency of ATD particles 63
4.4.4 Freezing efficiency of kaolinite particles 64
4.5 Discussion 64
4.5.1 Collision efficiency 64
4.5.2 Contact freezing process 66
4.6 Summary and conclusions 70
4.7 Wetting of particles 72

5 Conclusions and Discussion 73
5.1 Outlook and Comments 74

A Charge measurement 75

B Elemental composition of a silver iodide particle 77

List of symbols 79

List of Figures 82

List of Tables 83

References **85**

Acknowledgements **97**

Curriculum vitae **99**

Chapter 1

Introduction

1.1 Atmospheric aerosol and climate

Atmospheric aerosols are colloids of particulate matter suspended in the atmosphere. Aerosol particles can be solid, liquid and mixtures of solid and liquids. The sources of aerosols are natural as well as anthropogenic. Soil dust, sea salt, biological particles, volcanic ash etc. are natural aerosols while particulate matter emitted through chimneys of industries, vehicle exhaust, domestic heating etc. are anthropogenic aerosols (Seinfeld and Pandis, 2006). They can also form in the atmosphere when gas to particle conversion takes place. Aerosols are categorized based on their size into four modes: nucleation, Aitken, accumulation and the coarse mode. Nucleation mode (particle diameter (d_p) < 0.01 μm) particles are freshly emitted or in situ formed particles in the atmosphere. These particle have short lifetimes as they coagulate to form Aitken and accumulation mode particles. Aitken mode particles have diameters between 0.01 and 0.1 μm. The coarse mode particles ($d_p > 1$ μm) are mostly dust particles which are blown by the wind, large sea spray and mechanically generated particles from agricultural or mining activities. Pollens emitted by plants also fall in this category. The coarse mode particles have high sedimentation velocities and do not stay suspended in the atmosphere for a long time. Accumulation mode particles ($0.1 < d_p < 1$ μm) are the most important ones in the atmosphere since they have the longest lifetime.

Aerosol particles play an important role in the radiative budget of the climate system (Boucher, 2015). They scatter the incoming solar radiation and can also absorb incoming solar radiation (e.g. black carbon). Aerosols also scatter and absorb longwave radiation emitted by the Earth and the atmosphere. Figure 1.1 shows radiative forcing due to different drivers of climate change. A negative radiative forcing indicates energy lost from the climate system (cooling) and positive radiative forcing indicates gain of energy by the climate system (warming). Scattering and absorption of the radiation by aerosols is known as the aerosol direct effect. Aerosol forcing due to aerosol- radiation interaction is associated with high level of understanding as shown in Fig. 1.1. The absorption of solar radiation by aerosols such as black carbon is more than compensated by scattering of solar radiation by mineral dust, sulphate, nitrate and organic carbon particles. Absorption of radiation by aerosols can influence the stability of the atmosphere. Heating of the atmosphere by absorbing the aerosols impacts the relative humidity and therefore cloud formation. This effect is known as the semi direct effect. The

effective radiative forcing due to aerosol-radiation interaction is -0.45 Wm^{-2} with an uncertainty range of -0.95 to $+0.05$ Wm^{-2} and associated with a medium level of understanding (IPCC, 2013).

The influence of aerosols on cloud microphysics is referred to as the radiative forcing due to aerosol cloud interaction (IPCC 2013, formerly: aerosol indirect effect). Some of the aerosol particles in the atmosphere serve as cloud condensation nuclei (CCN) and/or ice nucleating particles (INP) to form either liquid droplets or ice crystals, respectively, depending on atmospheric conditions (Pruppacher and Klett, 1997). The cloud droplet number concentration depends on the concentration of CCN and the dynamic condition. An increase in aerosol concentration can lead to the increase in CCN concentration. For a fixed liquid water content, a higher concentration of CCN results in smaller droplets and higher droplet number concentration. This effect increases cloud reflectivity and is referred to as the first indirect effect or Twomey effect (Twomey, 1974). The glaciation indirect effect (Lohmann, 2002) is based on similar principles for INP as the first indirect effect for CCN. As shown in Fig. 1.2, aerosol number concentration would increase the INP number in the atmosphere, thereby increasing the ice particle number. Glaciation of a cloud will increase precipitation and decrease cloud lifetime and cloud albedo. The concentration of CCN or/and INP also influences cloud life time through enhancing or suppressing precipitation formation. This effect is known as the second indirect effect. The effective radiative forcing due to aerosol cloud interaction is estimated to be -0.45 Wm^{-2} with an uncertainty range of -1.2 Wm^{-2} to 0 Wm^{-2} (IPCC, 2013).

1.2 Clouds in the climate system

Clouds are visible manifestations of different atmospheric processes. They are not only important for precipitation but are also an important medium of heat transfer in the atmosphere. They are also an important regulator of the earth's radiation budget with about 60 % of earth's surface is covered with clouds (Lohmann and Feichter, 2005). Clouds scatter the incoming solar radiation and thus have a cooling impact on the climate. They also absorb the outgoing long wave radiation and trap the energy in the atmosphere leading to a warming of the climate system. The radiative properties of clouds depend on the phase of water inside the cloud and the temperature of the cloud. Low level clouds have a cooling effect on climate because they reflect large amounts of shortwave radiation back to space and emit longwave radiation at a similar temperature to that of earth. Arctic stratus clouds are an exception to this because they reflect less radiation back to space than they reflect towards the earth. Despite of their low altitude, they are responsible for a net heating of the climate system. Cirrus clouds absorb some long wave radiation emitted from lower levels of the atmosphere and the earth and emit little radiation due to their low cloud top temperatures. Cirrus clouds are semitransparent for shortwave radiation, thus have a small albedo effect and their green house effect dominates (Lohmann et al., 2016). Deep convective clouds have a near zero radiative effect because the albedo effect and the green house effect almost balance each other. The radiative forcing of mixed phase clouds depends on their ice and liquid water content. In the case of shallow mixed phase stratus cloud, a four fold increase in the ice number concentration can reduce the liquid water path by half (Ovchinnikov et al.,

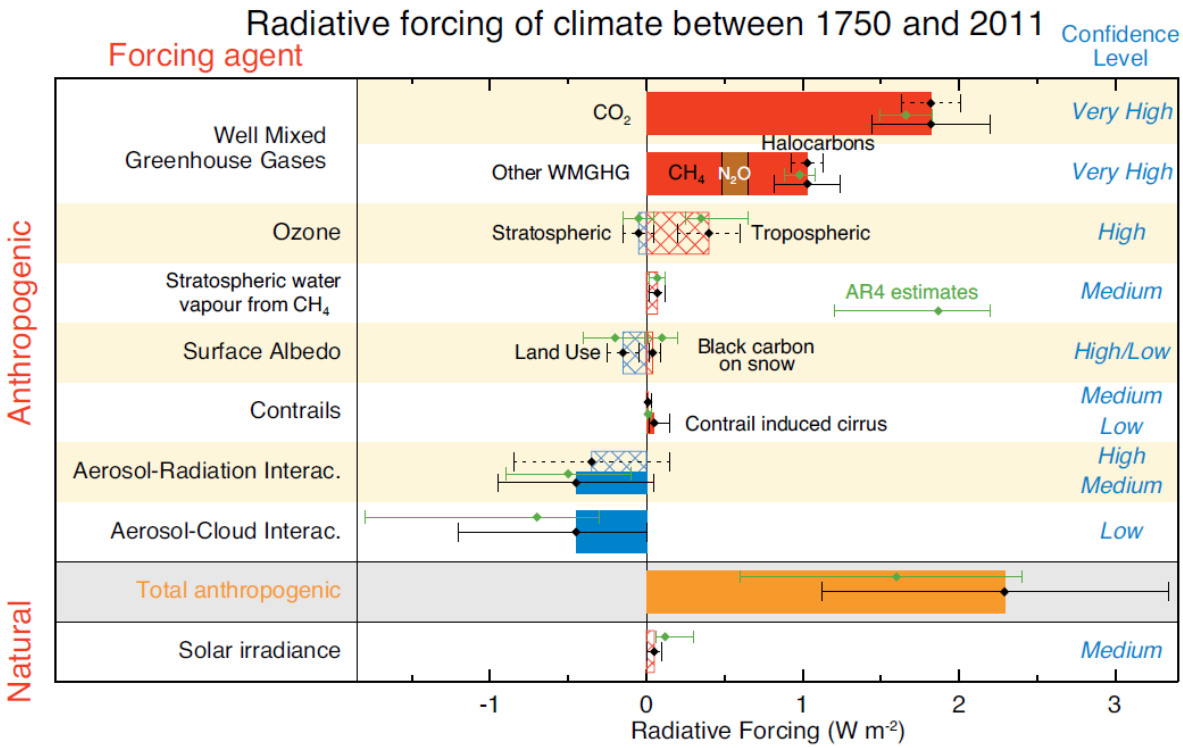

Figure 1.1: *Radiative forcing (RF) and effective radiative forcing (ERF) during the industrial era between 1750 and 2011 with the associated uncertainty range (solid bars are ERF, hatched bars are RF, green diamonds and associated uncertainties are for RF assessed in AR4). Adapted from IPCC (2013).*

2011). The glaciation rate in mixed phase clouds can influence the lifetime of the cloud and there by the radiative properties.

The short wave cloud radiative effect amounts to -47.3 Wm^{-2} and the long wave radiative effect to 26.2 Wm^{-2}(Boucher, 2015). the net cloud radiative effect on the top of the atmosphere is estimated to be -21.1 Wm^{-2}. This negative radiative forcing by clouds is potentially 5-6 times as large as the positive radiative forcing due to doubling of carbon dioxide concentration from preindustrial conditions (Lohmann et al., 2016).

1.3 Ice nucleation in the atmosphere

As mentioned in the previous section, the radiative properties of clouds depend on the physical properties of the cloud e.g. temperature, cloud cover, optical thickness and phase of water (Lohmann and Feichter, 2005). Clouds form when rising air saturates with respect to water and droplets are formed with the help of CCN. Ice formation in the atmosphere can take place in clouds below temperatures of 0°C. Cloud droplets can be cooled without phase change to a temperature of about -37°C. Formation of ice in the atmosphere can be broadly divided into two categories. Homogeneous nu-

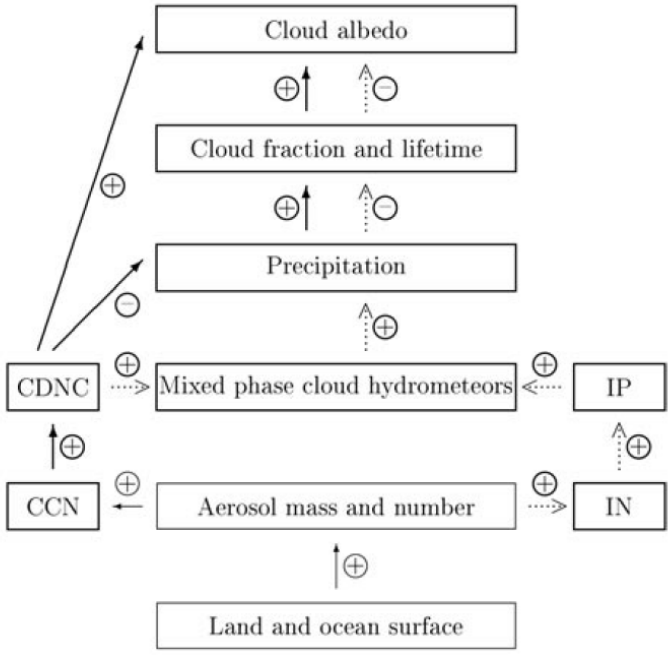

Figure 1.2: *Schematic diagram of the warm cloud indirect aerosol effect (solid arrows) and glaciation indirect aerosol effect (dotted arrows). CDNC, IP and IN are cloud droplet, ice particles and INP number concentration, respectively. Adapted from (Lohmann, 2002).*

cleation of cloud droplets takes place below $-37°$C when cloud droplets freeze spontaneously once this temperature is reached. The freezing point depression further reduces the freezing temperature of solution droplets. Cloud droplets can stay in a liquid state between 0°C and the homogeneous freezing temperature. These droplets are in a thermodynamically metastable state and called supercooled droplets. Freezing of supercooled droplets catalyzed by INPs is called heterogeneous nucleation and takes place between 0°C and the homogeneous freezing temperature.

1.3.1 Homogeneous ice nucleation

Supercooled water droplets freeze spontaneously at -37 °C by homogeneous nucleation where statistical fluctuation in temperature and density lead to inelastic collisions of water molecules forming an ice-like cluster of molecules (Pruppacher and Klett, 1997; Ickes et al., 2015). This cluster is termed ice embryo. The energy barrier associated with this first order phase transition can be thermodynamically described by changes of the Gibbs free energy (Pruppacher and Klett, 1997; Ickes et al., 2015). The formation of an ice embryo involves two competing processes: the formation of an interface between the embryo of the new phase and the surface of the initial phase and the increase in volume of the new phase. The work to form a new surface is positive because energy input is needed while the volume term is negative because energy is released. The change in Gibbs free energy for this

nucleation process can be derived by formulating the following expression for the change in Gibbs free energy ΔG for phase change:

$$\Delta G = n_e(\mu_i - \mu_w) + 4\pi r^2 \sigma_{iw} \tag{1.1}$$

where n_e is the number of water molecules in an ice embryo, μ_i and μ_w are the chemical potentials of molecules of the ice and the water phase, respectively, r is the radius of the ice embryo assuming it to be spherical and σ_{iw} is the interfacial energy between ice and water. The first term in this equation describes the change in the chemical potential due to the phase transition. This difference in chemical potential is expressed as:

$$\mu_i - \mu_w = -k_B T \ln\left(\frac{e_w}{e_i}\right) = -k_B T \ln S_i \tag{1.2}$$

where k_B is the Boltzmann constant, T is the temperature in K, e_w and e_i are saturation vapor pressures over water and ice, respectively, and S_i is the saturation ratio with respect to ice. The number of water molecules in a spherical ice embryo can be calculated with the following equation:

$$n_e = \frac{4\pi}{3}\frac{r^3}{\nu_i} \tag{1.3}$$

where ν_i is the volume of a water molecules in ice.

By inserting Eq. (1.2) and (1.3) in Eq. (1.1) one obtains:

$$\Delta G = -\frac{4\pi}{3}\frac{r^3}{\nu_i} \cdot k_B T \ln S_i + 4\pi r^2 \sigma_{iw}. \tag{1.4}$$

The first term in Eq. (1.4) is the volume term while the second one is the surface term. For the phase transition, the maximum ΔG needs to be found by

$$\left(\frac{\partial \Delta G}{\partial r}\right)_{r=r_c} = 0$$

where r_c is the radius of the critical embryo. Solving for r_c yields,

$$r_c = \frac{2\nu_i \sigma_{iw}}{k_B T \ln S_i}. \tag{1.5}$$

Substituting Eq. (1.5) in Eq. (1.4) for $r = r_c$ yields:

$$\Delta G = \frac{16\pi}{3} \cdot \frac{\nu_i^2 \sigma_{iw}^3}{(k_B T \ln S_i)^2}. \tag{1.6}$$

Fig. 1.3 shows the formation of an ice embryo at 236 K. The volume term contributes negatively to the Gibbs free energy and the surface term contributes positively. In the water droplet ice clusters can grow and dissipate frequently without reaching the critical size r_c. The formation of a spontaneously

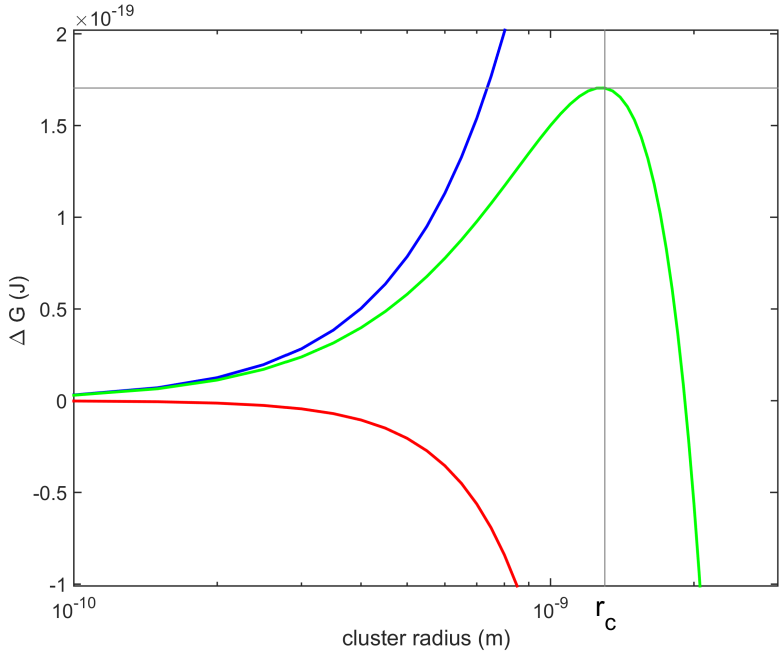

Figure 1.3: *Change in Gibbs free energy at 236* K. *The red line shows the volume term while the blue line represents the surface term. The green line shows the total change in Gibbs free energy to form the ice embryo. The gray vertical line indicates the critical radius r_c above which the ice embryo would continue to grow. The gray horizontal line indicates the energy barrier that needs to be to overcome for an ice embryo to grow. These calculations were performed for $\sigma_{iw} = 25 \times 10^{-3}$ Jm^{-2} and $\nu_i = 3 \times 10^{-29}$ m^3. Values taken from Ickes et al. (2015).*

growing ice germ per volume of water and time which leads to a freezing event is described by the homogeneous nucleation rate J_{hom}. The kinetic part of J_{hom} is governed by the flux of water molecules to the cluster and is given as

$$\Phi = \frac{k_B T}{h} \cdot n \; exp\left(\frac{-\Delta F}{k_B T}\right) \tag{1.7}$$

where h is the Planck constant, Φ is the diffusive flux and ΔF is the activation energy of molecules to diffuse through the liquid-ice interface and n is the number density of water molecules in liquid water ($n = 3.1 \times 10^{-22}$ cm^{-3} (Zobrist et al., 2007)).

With the Gibbs free energy term for the formation of a critical ice embryo and the kinetic term, J_{hom} is written as,

$$J_{hom} = \frac{k_B T}{h} \cdot n \; exp\left(\frac{-\Delta F}{k_B T}\right) exp\left(\frac{-\Delta G}{k_B T}\right). \tag{1.8}$$

Experimentally J_{hom} can be determined by measuring the frozen droplet fraction (FF) per time (t),

$$J_{hom} = -\frac{\ln(1-FF)}{V_{drop}t} \tag{1.9}$$

where V_{drop} is the volume of the droplet.

1.3.2 Heterogeneous ice nucleation

Ice nucleation in the atmosphere can also be catalyzed by special types of aerosol particles called ice nucleating particles (INPs). The criteria for an aerosol particle to act as an INP are thought to be solid or crystalline state, size, lattice structure, molecular bindings with water and active sites (Lohmann et al., 2016). INPs lower the energy barrier of the phase transition to form a critical ice germ. With the help of INPs, ice nucleation can take place at higher temperatures. Ice nucleation can also take place at lower supersaturation i.e. only supersaturation with respect to ice might be required. Depending on the temperature and supersaturation conditions, four different pathways of heterogeneous ice nucleation can be identified (Pruppacher and Klett, 1997).

- *Deposition nucleation*: This is the only pathway of ice nucleation in the atmosphere where no liquid phase is involved. The nucleation takes place when water vapor in the atmosphere gets deposited on the INP. Once the critical ice embryo is formed by vapor deposition, the ice crystal can grow. Deposition nucleation can take place below water saturation and only supersaturation with respect to ice is required.
- *Immersion freezing*: In case of immersion freezing of cloud droplets, the INP first acts as a CCN and droplet freezing takes places when the droplet temperature is lowered to the heterogeneous freezing temperature. The supercooling of a droplet needed for immersion freezing depends on the INP properties. Immersion freezing has been identified as the dominant mechanism of ice formation in mixed phase clouds (Hoose et al., 2010; Murray et al., 2012; Welti et al., 2012).
- *Condensation freezing*: Condensation freezing takes place when water saturated conditions are reached below 0°C and the condensing water freezes on the INP instantaneously.
- *Contact freezing*: Contact freezing occurs when ice nucleation is initiated by the collsion of an INP with the supercooled droplet. The collision efficiency depends on the atmospheric conditions as well as droplet and INP properties (see chapter 2).

Fig. 1.4 shows the typical freezing pathways as a function saturation with respect to ice. It should be noted that all the mechanisms can take place at all temperatures. As shown in the figure, a droplet goes through heterogeneous nucleation conditions while rising with an air parcel before it can freeze due to homogeneous freezing.

In the case of heterogeneous nucleation, the energy barrier of nucleation is lowered compared to homogeneous nucleation. The difference in energy barrier for homogeneous freezing and heterogeneous freezing is accounted for by a geometric factor f, which is also termed as the contact angle parameter. When an ice embryo forms on an INP, the required number of water molecules to form

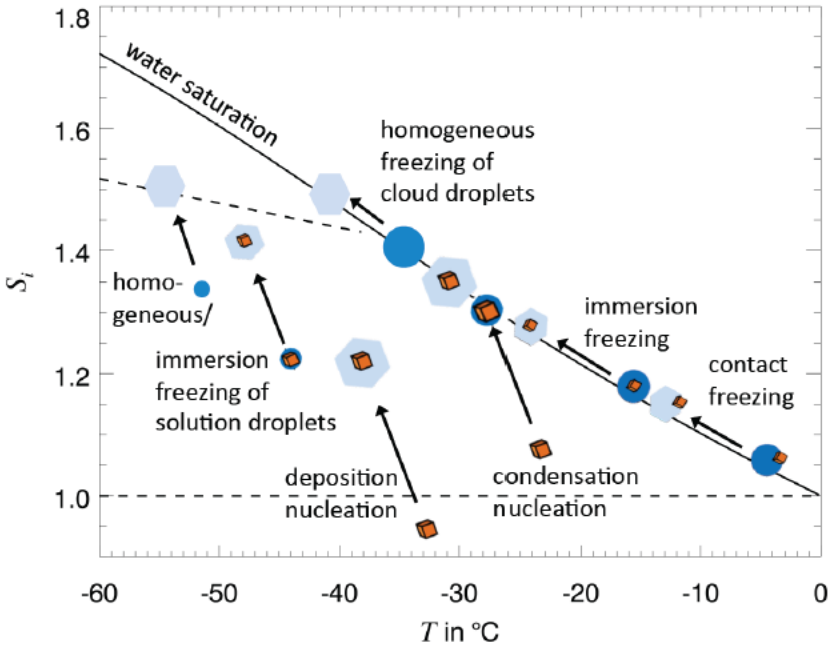

Figure 1.4: *Schematic representation of the different nucleation modes. Adapted from Hoose and Möhler (2012).*

the ice embryo are reduced. The resulting change in Gibbs free energy for heterogeneous nucleation is given as:

$$\Delta G_{het} = f(\theta)\Delta G \tag{1.10}$$

where ΔG_{het} is the change in Gibbs free energy for heterogeneous nucleation, and θ is the contact angle between the INP and the ice phase. The contact angle θ can have a value between 0° and 180°. The geometric factor for heterogeneous nucleation is given as follows:

$$f(\theta) = \frac{(2+\cos\theta)(1-\cos\theta)^2}{4}. \tag{1.11}$$

For a flat surafce, θ can be expressed in terms of the interfacial tensions between the different phases by the Young equation:

$$\cos\theta = \frac{\sigma_{w,INP} - \sigma_{i,INP}}{\sigma_{iw}}, \tag{1.12}$$

where $\sigma_{w,INP}$ and $\sigma_{i,INP}$ are the interfacial tensions between water and INP and ice and INP, respectively, and σ_{iw} is the interfacial tension between water and ice.

Fig. 1.5 shows the lowering of ΔG in the presence of an INP with different contact angles at 253 K.

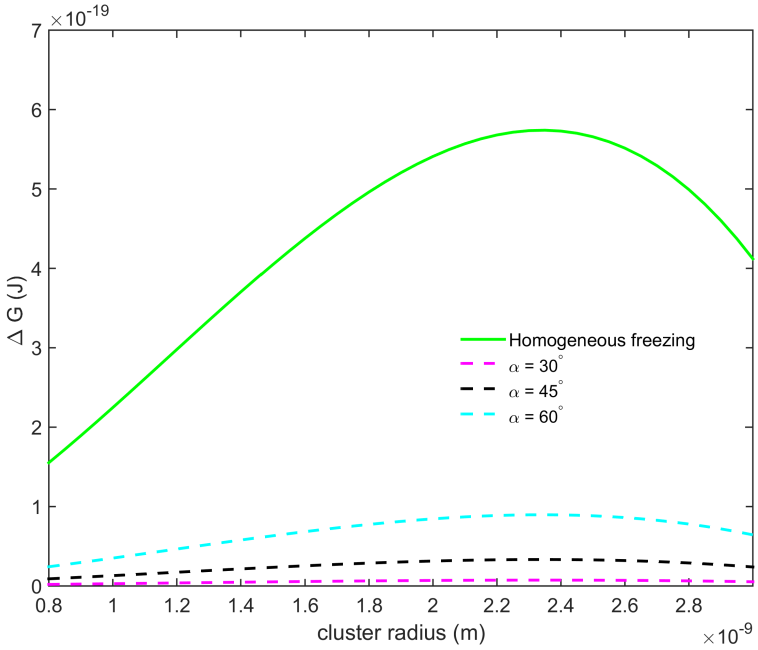

Figure 1.5: *Nucleation energy barrier for homogeneous freezing and heterogeneous freezing with contact angles of* 30°, 45° *and* 60°. *These calculations are performed using* $T = 253$ K, $\sigma_{iw} = 25 \times 10^{-3}$ Jm^{-2} *and* $\nu_i = 3 \times 10^{-29}$ m^3.

The heterogeneous nucleation rate is defined as:

$$J_{het} = \frac{k_B T}{h} \cdot n_s \, exp\left(\frac{-\Delta F}{k_B T}\right) exp\left(\frac{-\Delta G_{het}}{k_B T}\right) \tag{1.13}$$

where n_s ($\approx 10^{15}$ cm^{-2}) is the number density of water molecules at the INP/water interface (Zobrist et al., 2007; Marcolli et al., 2007).

In the mixed-phase cloud regime, immersion freezing and contact freezing are the most important freezing pathways given that both of these can start from liquid droplets (Hoose et al., 2008). The first temperature of freezing or onset temperature of freezing becomes an important parameter in mixed-phase clouds because of the Bergeron-Findeisen process. In the mixed phase cloud regime, ice crystals can grow at the expense of water droplets due to the lower saturation vapor pressure over ice than over liquid water. Glaciation of mixed-phase clouds proceeds at a faster rate once some ice crystals have formed which can result in faster precipitation formation.

1.4 Contact freezing

Contact freezing is probably the least understood pathway of ice formation in the atmosphere. Various experimental studies (Niehaus et al., 2014; Fornea et al., 2009; Svensson et al., 2009; Gokhale

and Spengler, 1972; Levin and Yankofsky, 1983) have observed higher onset temperatures by 2 to 8 °C for the same INPs in contact freezing mode compared to immersion freezing. Ladino et al. (2011b), concluded that there are some hints for contact freezing to be more efficient than immersion freezing. Hoffmann et al. (2013a) observed contact freezing to dominate over immersion freezing on the timescale of their experiment. Therefore understanding the mechanisms behind contact freezing becomes important.

Fig. 1.6 shows the position of an INP while the droplet freezes by contact nucleation. In panel (a) the INP has collided with the surface of the droplet from the outside and is not immersed. Considering this situation, Cooper (1974) proposed a mechanism for contact freezing in which the subcritical embryos can form on the surface of the INP even though the air is subsaturaturated with respect to water. Relying on classical nucleation theory, the critical radius of an ice embryo for deposition nucleation should be larger than for immersion freezing. Therefore, Cooper (1974) conjectures that INPs may possess on their surface ice embryos larger than the critical size for an embryo immersed in water so that such ice embryos may nucleate ice when the INP comes in contact with a cloud droplet. Fukuta (1975a) proposed an alternative mechanism for contact nucleation, where freezing occurs when the supercooled water spreads over the INP surface. As the INP comes into contact with the droplet, the air-liquid-nucleus boundary line moves along the INP surface and the INP surface is wetted with the bulk water. When the bulk water starts to propagate over the INP, a transient high free energy zone will be formed which lowers the free energy barrier for nucleation. This freezing mechanism refers to the case depicted in panel (a) of Fig. 1.6.

Durant and Shaw (2005) and Shaw et al. (2005) observed higher freezing temperatures when the INP was making contact with the surface of the droplet as shown in panel (b) of Fig. 1.6. They termed this mode contact freezing inside-out. Cantrell and Heymsfield (2005) noted that the causes for this mechanism are unknown and different from what has been proposed either by Fukuta (1975a) or Cooper (1974). Fornea et al. (2009) also observed contact freezing inside-out for atmospheric aerosols containing ash, soot, and soil. Sear (2007) using a theoretical model observed that the nucleation rates were four orders of magnitude larger at the contact line than they were anywhere else. He found also that classical nucleation theory predicts a low free energy barrier at the contact line unless there is complete wetting. Another thermodynamical model proposed by Djikaev and Ruckenstein (2008) corroborated the findings of Sear (2007). Suzuki et al. (2007) found from their experiments that the temperature at which nucleation occurred at a contact line shows a dependence on the contact angle which is not linear. The importance of the contact line for contact freezing was refuted by Gurganus et al. (2011, 2013) who observed in their experimental studies no preference of nucleation at the contact line. The same group also studied the contact freezing (Gurganus et al., 2014) with nanotextured substrates and found that the preferred nucleation site was the nanotextured surface. Their observations are consistent with enhanced nucleation at sharp corners or so called active sites. Djikaev and Ruckenstein (2008) proposed that the line tensions associated with the three phase contact lines may play a similar role as the surface tension. The line tension of three phase contact gives rise to an additional term in the formation free energy of the cluster. They also proposed that whether

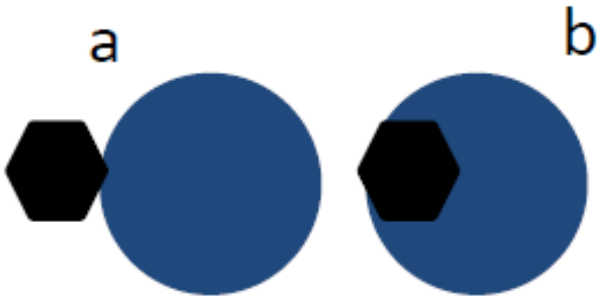

Figure 1.6: *Position of INP for contact freezing. Panel (a) denotes the more classical approach (e.g., Ladino et al., 2011b) while panel (b) shows approach proposed by Shaw et al. (2005).*

contact freezing will be enhanced compared to immersion freezing, and whether this will occur for particular foreign particles will depend on the interplay between the surface tensions and line tensions involved in the process. Based on this work by Djikaev and Ruckenstein (2008), Gurganus et al. (2014) proposed that a line tension term should be subtracted while calculating the energy barrier of crystallization or nucleation as it can change the shape of ice embryo for the minimum surface energy. They also proposed that pores resonant with the critical nucleus size, or distortion and curvature of the contact line lead to a reduced free energy barrier for nucleation as it can be effective in lowering the energy barrier.

Describing contact freezing in the atmosphere is even more complex due to the complex nature of collision mechanisms between particles and droplets. Even though contact freezing is widely reported to be the nucleation process with the highest freezing temperature, it is limited due to the collision rate between droplets and particles (Hoose et al., 2008). Other limitations of contact freezing in the atmosphere can be the availability of interstitial aerosol particles in the cloud that are able to act as INP. Ladino Moreno et al. (2013) in their review reported that the quantification of the number of collisions between droplet and particles was neglected in many previous studies which makes comparison of the efficiency of contact freezing with that of immersion freezing difficult. Recent studies by Hoffmann et al. (2013a) and Niehaus et al. (2014) have attempted to quantify the number of collisions between droplets and particles required for contact freezing. Hoffmann et al. (2013b) have reported that even though more than one collision is required for contact freezing, it has been the dominant mechanism of freezing on their experimental time scale. Niehaus et al. (2014) have reported that more than 1000 collisions for Arizona test dust particles were required to freeze one droplet at -19 °C.

Apart from laboratory investigations, many field observations, although circumstantially, have indicated that that contact freezing may play a role in natural clouds (Hobbs and Rangno, 1985). Due to the mixing of ambient air into the top of the cloud, contact freezing becomes favorable (Hobbs and Rangno, 1985). This favorable condition is described by Hobbs and Rangno (1985) as the thermophoretic force which can drive sub-micron aerosols into contact with the supercooled droplets

which may have surface temperatures several degree colder than the environment due to evaporation. Young (1974) and Cooper (1974) proposed that rapid glaciation of mixed-phase clouds could be due to the contact freezing. Durant and Shaw (2005) postulated that sudden ice formation of evaporating cloud droplets in wave clouds is due to contact freezing inside-out. Recently Seifert et al. (2011) suggested that contact freezing can be one of the reason for the glaciation of clouds containing volcanic ash. Ansmann et al. (2005) observed ice formation at cloud edges and downdraft region and concluded that contact freezing played an important role in ice formation. Twohy et al. (2010) did not observed any enhance ice nucleation activity in the evaporating downdraft regions of orographic wave cloud.

Modeling study conducted by (Hoose et al., 2010) found immersion freezing to be the dominant ice nucleation mechanism except for uncoated soot particles which can remain unactivated in the cloud. Philips et al. (2007) concluded that condensation freezing and deposition nucleation are the pathways for formation of almost all of the heterogeneous ice and contact freezing has little impact in their model study.

Aerosols may have a significant effect on mixed-phase and ice clouds but the processes governing aerosol interactions with the ice phase are less well-understood than for the liquid phase (Boucher, 2015). This may lead to an uncertainty in radiative forcing due to the limited understanding of the ice initiation processes. In order to understand and quantify ice nucleation in the atmosphere, understanding of contact freezing and its effectiveness relative to other freezing mechanisms need to be quantified. This can also help in describing ice and precipitation formation in the climate models.

Field studies have indicated that liquid water droplets are the prerequisite for ice formation in the atmosphere, implying that deposition nucleation plays a secondary role under mixed phase cloud conditions (Murray et al., 2012). Ansmann et al. (2009) found that for 99 % of the observations of mixed phase clouds over Cape Verde, ice nucleation started from the liquid phase concluding that deposition nucleation and condensation freezing are perhaps unimportant in mixed phase clouds. This leaves immersion freezing and contact freezing to be the most prominent candidates for ice nucleation in mixed-phase clouds.

1.5 Outline of the thesis

This work is a continuation of the previous experimental study on contact freezing by Ladino et al. (2011b) and was targeted accordingly. This thesis is structured as follows:

- The second chapter of this study is dedicated to the experimental design of the current set of collision ice nucleation chamber. Various observations found by previous study might have been because of the technical design of the instruments, which realized at the start if this study. Changes in instrumentation to overcome the criticisms are described. A brief survey of the current state of the art experiments by other groups will be provided. Sensitivity studies of

collision efficiency will be followed in order to provide a larger picture of the droplet particle collision process.

- The third chapter of this thesis deals with the collision efficiency. It was realized that freezing efficiencies > 1 reported by Ladino et al. (2011b) might be due to the fact that the collision efficiency used to calculate freezing efficiency was too low giving too less number of collisions between droplets and particles. The accurate quantification of collision efficiency is crucial in order to quantify contact freezing. This work has attempted to obtain collision efficiencies at subzero temperatures where contact freezing can take place. In this chapter, a review of the collision processes in the context of present work is also provided.
- The fourth chapter of this study deals with the comparison of immersion freezing and contact freezing. The method of comparison is elaborated in the context of freezing efficiency in contact and immersion mode. Freezing efficiencies for silver iodide, kaolinite and Arizona test dust for immersion and contact freezing are compared for two different residence times of droplets in contact freezing experiment.
- This Ph.D. thesis ends with overall conclusions and outlook for future work. Some improvements on the instrumentation and the methodology are suggested for future experiments.

Chapter 2

The Collision Ice Nucleation Chamber

2.1 Instrument details

The CoLlision Ice Nucleation CHamber (CLINCH) was constructed to study collision efficiency between droplets and particles, and to perform contact freezing studies. It has been used previously by Ladino et al. (2011a) and Ladino et al. (2011b) for both of these purposes. Technical drawings and design details are also given in Ladino (2011). We focus here on changes in the contact freezing experiment between Ladino (2011) and this work. The Fig. 2.1 shows a schematic of the experimental set up of CLINCH. It consists of two parallel anodized aluminum plates of 10 cm in breadth which are separated by 1 cm. The whole rectangular configuration can be separated in blocks of 20 cm in length so that the length of the chamber can be varied from 20 cm to 80 cm. Each block has three ports for mounting the detector. The parallel plates also serve as a rectangular ducts for the cooling liquid. They are filled with ethanol as a cooling liquid by the cryostat (Lauda Proline). The temperature of each 20 cm block of the chamber is measured by four thermocouples. The temperature of the chamber can be adjusted from -55 °C to 40 °C. The head of the chamber consists of an orifice with a diameter of 1 cm to mount the droplet generator and a glass window to observe the droplets with the camera (Moticam 2300) attached with lense system (Navitar Zoom 600). A red LED is mounted on the opposite side of the glass window to illuminate the droplet. The LED is operated with a stroboscope of the same frequency as that of the droplet generator. The droplet generator can be mounted on the chamber orifice with a custom designed adapter and O-ring to avoid a leakage in the system. The droplet generator used in this work was procured from Bremen University. The droplet generator can produce droplets with diameters of 80 ± 3.5 μm. The size of the droplets can be measured from the image captured by the camera with a free software ImageJ. Figures 2.2 and 2.3 show the typical droplet image captured by the camera and measured droplet diameter with a precision of 1 μm. While performing an experiment, the walls of the chamber are covered with a thin layer of ice creating an ice saturated environment. The aerosol concentration is measured at the end of the chamber with a condensation particle counter (CPC TSI Model 3772). Particles can be generated in the aerosol generation unit which can either consist of a fluidized bed generator (TSI Model 3400A) where aerosols are generated by dry dispersion (e.g.for mineral dusts) or by an atomizer (e.g. for silver iodide). The generated aerosol particles are passed through a cyclone in order

to remove particles larger than 1 μm. The filtered aerosol particles are then passed through a ionized radiation source (or 'neutralizer', Polonium-210) which imparts particles with a known Boltzmann charge distribution (Hinds, 2012). The 'neutralized' particles then enter the Differential Mobility Analyser (DMA, TSI Model 3081) where they are size selected according to their electrical mobility. After this the size selected particles enter the CLINCH.

2.2 Ice optical Detector (IODE)

The contact freezing experiment performed with the continuous flow diffusion chamber requires differentiation between water droplets and ice crystals. The Ice Optical DEtector (IODE) utilized in this study was developed by Nicolet et al. (2010). IODE discriminates between liquid and frozen droplets relying on the principle of depolarization of polarized light by aspherical objects like ice crystals and was designed to measure ice particles in cloud chambers. When linearly polarized laser light is reflected back from aspherical objects, it obtains a depolarized component. The linear polarized component and the depolarized component are separated using a Wollaston prism which splits the light into parallel and perpendicular polarization components. The depolarization ratio δ can be calculated as (Nicolet et al., 2010):

$$\delta = \frac{I_{\perp}}{I_{\parallel} + I_{\perp}} \tag{2.1}$$

where $I_{\perp}$ and $I_{\parallel}$ are the signal intensities in the perpendicular and parallel channels, respectively. Theoretically δ should be zero for water droplets and increase as the asphericity of the reflecting object increases. In practice, even the depolarization of a perfectly spherical object is not zero and was determined by Lüönd et al. (2010) to have a depolarization ratio of $\delta = 0.07$. This value was confirmed using the IMCA/ZINC (Welti et al., 2012) setup. At the experimental conditions of the contact freezing experiment, the background readings of both $I_{\perp}$ and $I_{\parallel}$ are noted with no droplets, and with only particles inside the chamber. Before classifying particles to be either water droplets or ice crystals, the background signal from the aerosol and walls of the chamber is subtracted. When droplets pass through CLINCH, based on the IODE signals for $I_{\perp}$ and $I_{\parallel}$ and using eq. 2.1, it is determined whether a droplet has frozen. The frozen fraction is determined as:

$$FF = \frac{N_{ice}}{N_{ice} + N_{water}} \tag{2.2}$$

where N_{ice} and N_{water} are the number of ice crystals and water droplets detected by IODE, respectively.

Ladino et al. (2011b) observed using the IODE detector that the frozen fraction and freezing efficiency of contact freezing does not depend on the concentration of the particles. This observation raises questions as the number of collisions between droplets and particles should vary linearly with particle concentration (see Eq. (2.7)). Ladino et al. (2011b) suggests that the independence of freezing efficiency on particle concentration is due to the presence of several droplets simultaneously in

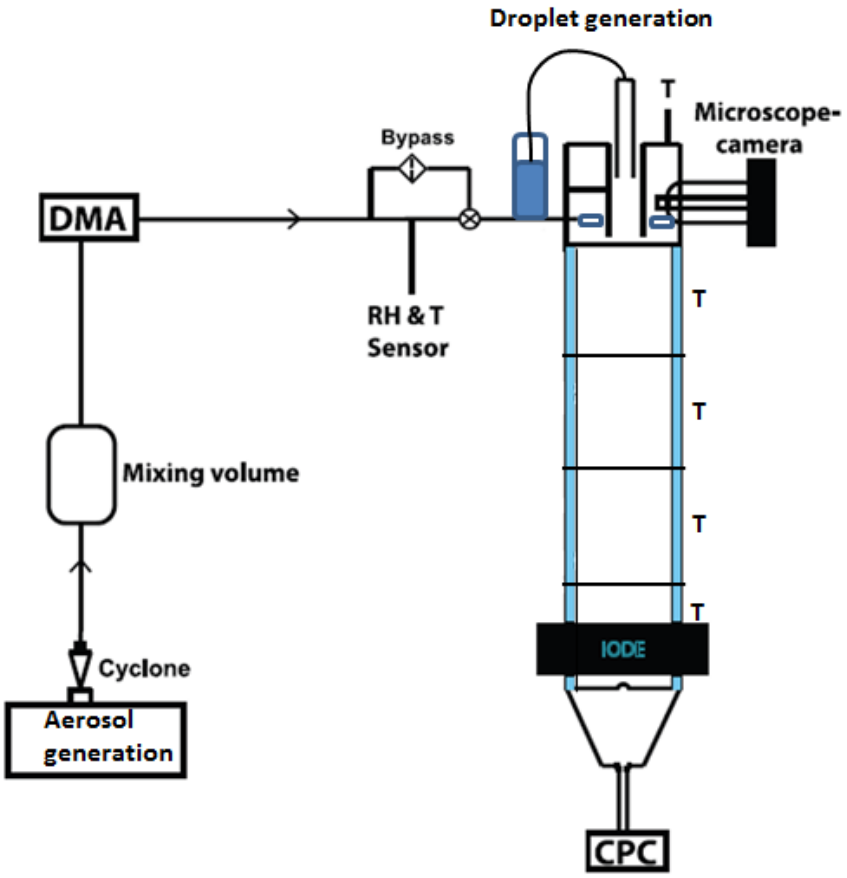

Figure 2.1: *Schematic of the CoLlision Ice Nucleation CHamber. Aerosol generation and size selection with DMA followed by the RH and temperature (T) sensors and the chamber. Droplets are generated at the top center. Modified from Ladino et al. (2011b).*

Table 2.1: *Differences between Ladino et al. (2011b) and this work*

Parameter	Ladino et. al.2011b	This work
Chamber length (cm)	40	80
Initial droplet diameter (μm)	26	80
Droplet residence time (s)	5	2 and 4
Frequency of droplet generation (Hz)	300	100
Distance between two droplet in stream (mm)	0.14	2

laser beam. The laser used was a GaN diode laser operating at 407 nm (Oxxius-405) with 1 mm beam diameter. To avoid the presence of multiple droplets in the laser beam, a laser needs to be used where the beam would have a smaller diameter or a laser with a rectangular beam profile. We installed a laser operating at 402 nm wavelength (Schaefter + Kirchhoff laser Makroliniengenerator13LTM) with rectangular beam profile in the IODE. To validate the principle of IODE and in order to check

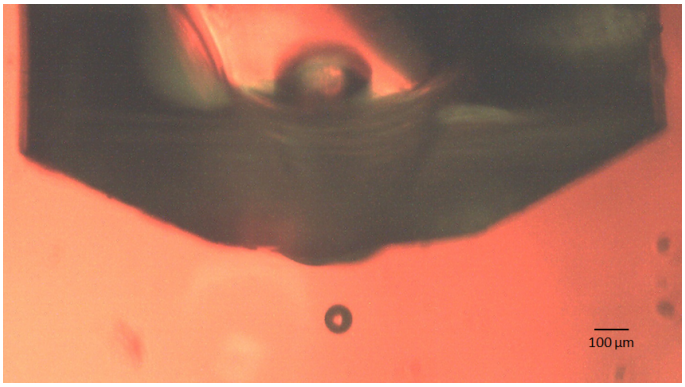

Figure 2.2: *80 µm droplet as observed by the camera.*

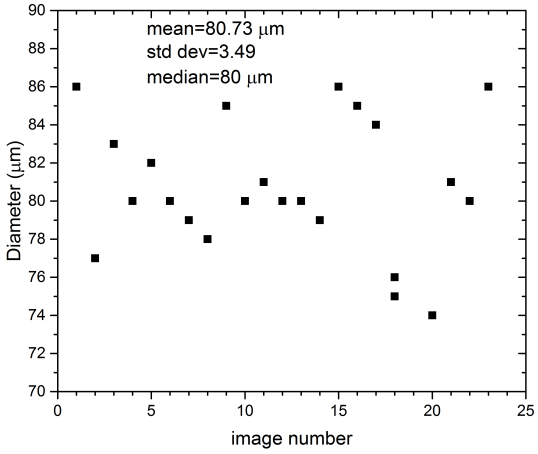

Figure 2.3: *Size measurement of typical droplet images captured by the camera.*

the validity of the discrimination by depolarization ratio, homogeneous freezing experiments were performed with 80 μm diameter droplets with different lengths of CLINCH. In Fig 2.4, it can be seen that, the homogeneous freezing temperature of the droplets is close to the value predicted by classical nucleation theory. The marginally higher freezing temperatures can be attributed to the water subsaturation in the chamber so that where droplet temperature is slightly lower than the chamber temperature due to evaporation.

Fig.2.5 shows the change in relative humidity with respect to water (RH_w) when the relative humidity with respect to ice (RH_i) is kept at 100 % inside CLINCH. It should be noted that the droplet evaporation depends on RH_w and temperature i.e. at the same RH_w, the evaporation rate is higher at higher temperature. In subsaturated conditions like in the CLINCH chamber the droplet evaporates. The significance of this for the collision efficiency is discussed in section 2.4.

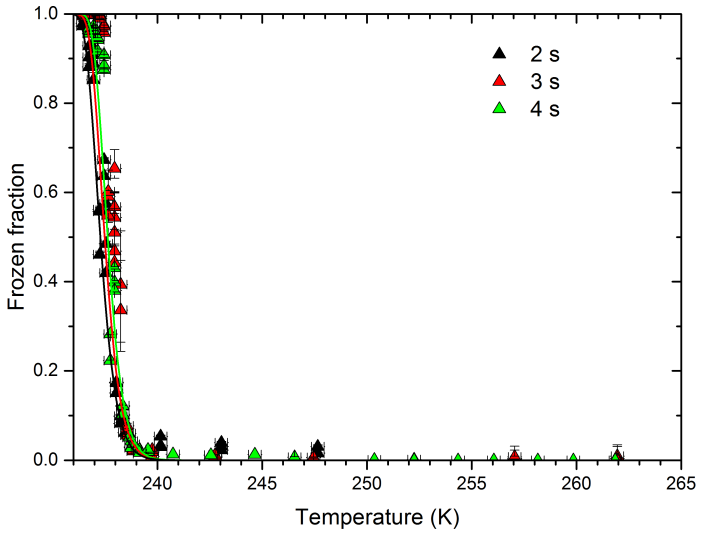

Figure 2.4: *Homogeneous freezing measured with the CLINCH set up for residence times of droplets in the chamber of 2, 3 and 4 s measured with the new laser and evaluated for* $\delta = 0.07$. *Lines indicate the frozen fraction of droplets calculated according to classical nucleation theory for an 80 µm droplet and 2, 3 and 4 s residence times.*

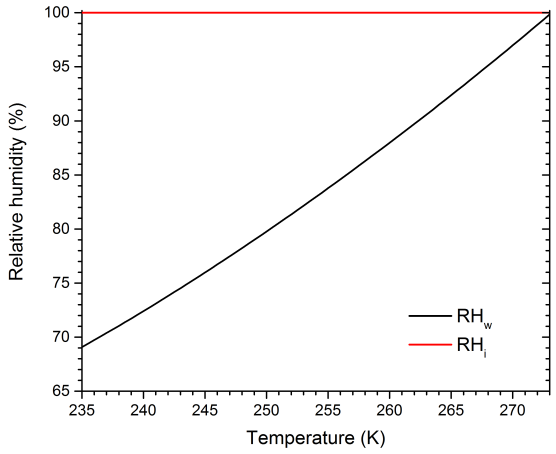

Figure 2.5: *Relative humidity with respect to water* RH_w *in CLINCH as a function of temperature when the CLINCH walls are held at 100 % relative humidity with respect to ice* RH_i.

2.3 Droplet size evolution in CLINCH

The size evolution of droplets at ice saturation can be calculated from Eq. 13-15b of Pruppacher and Klett (1997) as:

$$r_d \frac{dr_d}{dt} = \frac{D_v^* M_w}{R_v \rho_w} \left(\frac{p_a^0}{T_a} - \frac{p_s^0}{T_s} \right), \tag{2.3}$$

where r_d is the radius of the droplet, t is the residence time of the droplet in the chamber, D_v^* is the modified diffusivity of water vapor, R_v is the gas constant for water vapor, ρ_w is the density of water, T_a is the environment temperature, T_s is the droplet surface temperature, p_a^0 is the saturation vapor pressure of the environment and p_s^0 is the saturation vapor pressure at the droplet surface. The temperature of the droplet surface is given by Eq. 13-23 of Pruppacher and Klett (1997):

$$T_s = T_a + \frac{L_e \rho_w}{k_a^*} r_d \frac{dr_d}{dt} \tag{2.4}$$

where k_a^* is the modified thermal conductivity of air and L_e is the latent heat of evaporation.

Figure 2.6 shows the change in size while the droplet falls through the CLINCH chamber. The droplet starts at 281 K. The slightly higher negative slope of the green line indicates that the smaller droplet has a greater evaporation rate. The droplet surface temperature calculations show that the smaller droplet adapts to the conditions at a faster rate than the larger droplet. The 26 μm diameter droplet cools down to the chamber temperature in about 0.1 s while the 80 μm diameter droplet needs about 0.6 s when the temperature of chamber is kept at 235 K.

2.4 Collision efficiency

The collision efficiency (E) is an important parameter in the context of ice nucleation of cloud droplets by contact freezing. E is defined as the fraction of particles that collide with the droplet in the cylindrical volume swept out by a falling droplet. Figure 2.7 shows a schematic of the collision process between a droplet of radius r_d and an aerosol particle of radius r_p. The impact parameter x_o is defined as the maximum horizontal distance between the center of a droplet and the center of an aerosol particle to achieve the collision. Lohmann et al. (2016) defined E as the probability that the collector drop will collide with a particle located at random in the sweep-out volume. Quantitatively E is defined:

$$E = \frac{x_o^2}{(r_d + r_p)^2} \tag{2.5}$$

As shown in Fig.2.7, as the particle approaches the droplet, the particle will follow the streamlines depending on the inertia of the particle. If the particle has high inertia, it does not follow the streamlines, instead collides with the particle. The following collision mechanisms govern the number of collisions between the droplets and the particles (Seinfeld and Pandis, 2012):

- *Brownian diffusion*: Due to the bombardment with the molecules of the air, the aerosol particle undergoes changes in the trajectory of motion. This motion is termed Brownian diffusion. Due to Brownian diffusion, particles can move towards the droplet resulting in the capture of particles by the droplets. Brownian diffusion increases with decreasing particle size, and becomes most effective collision mechanism for particles with $d_p < 0.2$ μm.

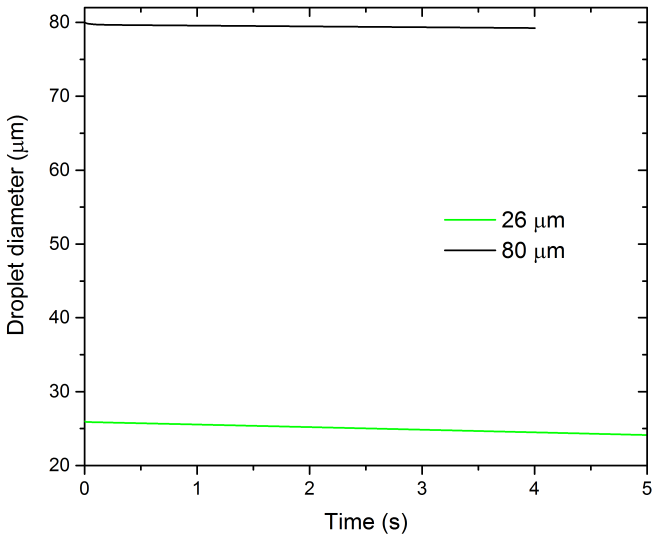

Figure 2.6: *Evolution of droplet size inside CLINCH at 245 K and 75 % RH_w. The green line shows the droplet size used by Ladino et al. (2011b) while the black line represents the droplet size used in this work. The black line stops at 4 s because this is the maximum residence time of the 80 μm droplet in the chamber.*

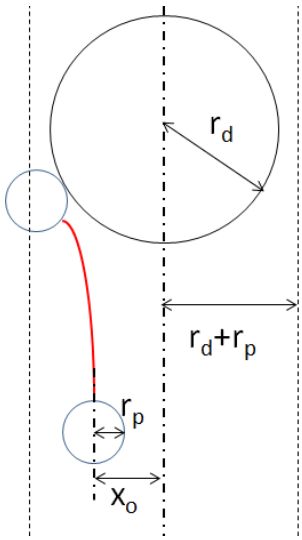

Figure 2.7: *Schematic representation of the collision process between a droplet of radius r_d and an aerosol particle of radius r_p, x_o stands for the impact parameter i.e. the maximum distance from the center of the droplet within which collision is certain. The red line shows the trajectory of the particle.*

- *Inertial impaction*: Particles with finite mass moving with the air flow may not follow the streamlines due to their inertia i.e. the trajectory of the particle deviates from the streamlines and continues to move towards the droplet leading to a collision. Inertial impaction is prominent for larger particles with a diameter $d_p > 1$ μm.

- *Interception*: Even if the trajectory of a particle does not deviate from the streamline, a particle will be collected by the droplet if the streamline brings it within a distance to the droplet of one particle radius. The particles with a finite size can be collected in the absence of Brownian motion and inertial impaction, establishing the importance of the contribution of interception to the collision efficiency (Kulkarni et al., 2011).

Fig. 2.8 panel (a) shows on the left side shows impaction and on the right side interception of particle by a droplet. Panel (b) shows collection of the particle due to Brownian motion.

The particle size dependent collision mechanisms are effective for particle diameters $d_p < 0.2\ \mu$m and $d_p > 1\ \mu$m. The range of diameters between $0.2\ \mu\text{m} < d_p < 1\ \mu$m is called the Greenfield gap (Greenfield, 1957). This gap can be filled partially by the collision efficiency mechanisms which are dependent on environmental conditions of the droplets and particles and their charge (Ladino, 2011; Tinsley et al., 2006a). These mechanisms are as follows:

- *Thermophoresis*: The temperature difference between the two sides of the particle pushes it towards colder temperatures. This happens because the momentum of the air molecules at the warmer side of the particle is larger than at the colder side and it pushes the particle towards colder temperatures by the Brownian motion of the air molecules. In case of evaporating droplets, the droplet surface is colder than the environment and the particles get pushed towards the droplet.
- *Diffusiophoresis*: The vapor gradient between the two sides of the particle exerts a force on the particle due to the diffusion of vapor from a high saturation region to a low saturation region. Diffusiophorsis acts opposite to thermophoresis for evaporating droplets as well as for droplets growing by condensation.
- *Electrophoresis*: This process takes place in the case of charged particles. If the particle and the droplet are oppositely charged, they are attracted towards each other resulting in a collision. Electrophoresis can also take place between droplets and particles carrying the same charge by means of image charge formation (Tinsley and Leddon, 2013).

In Fig. 2.8, panel (c) shows the thermophoretic and diffusiophoretic process. As shown in the figure, these two processes act opposite to each other.

Usually, collision efficiencies of each of these processes are formulated separately and added together to yield the total collision efficiency E_{Tot} as follows,

$$E_{Tot} = E_{Br} + E_{imp} + E_{int} + E_{Th} + E_{Df} + E_{El} \tag{2.6}$$

where E_{Br}, E_{imp}, E_{int}, E_{Th}, E_{Df}, and E_{El} are collision efficiencies due to Brownian diffusion, inertial impaction, interception, thermophoresis, diffusiophoresis and electrophoresis, respectively. Analytical expressions for all six collision efficiencies are discussed in chapter three.

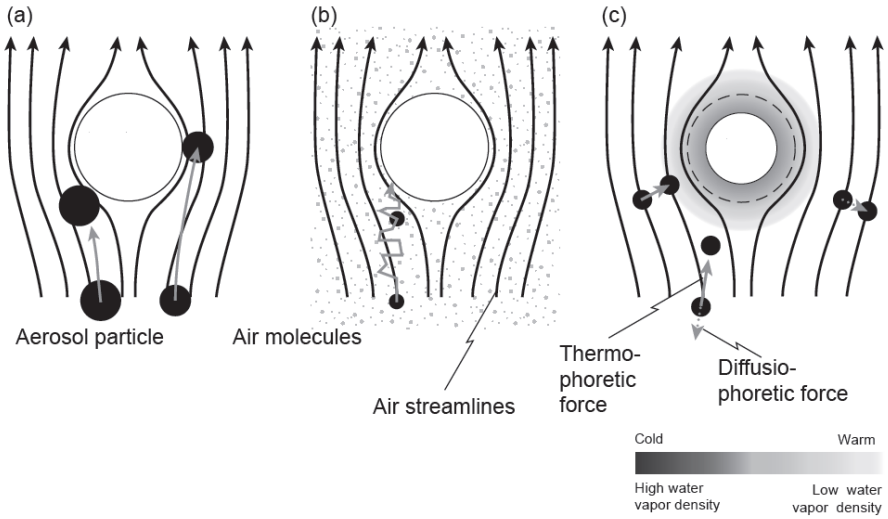

Figure 2.8: *Schematic of the different forces/ processes that can contribute to a collision of an aerosol particle with droplet: (a) inertial impaction (left) and interception (right), (b) Brownian motion and (c) thermophoresis (left), diffusiophoresis (right) and combined phoretic forces (below). Gray arrows show the direction of the processes. As the different processes are important for aerosol particles of different sizes, they are shown in different sizes. Adapted from Lohmann et al. (2016).*

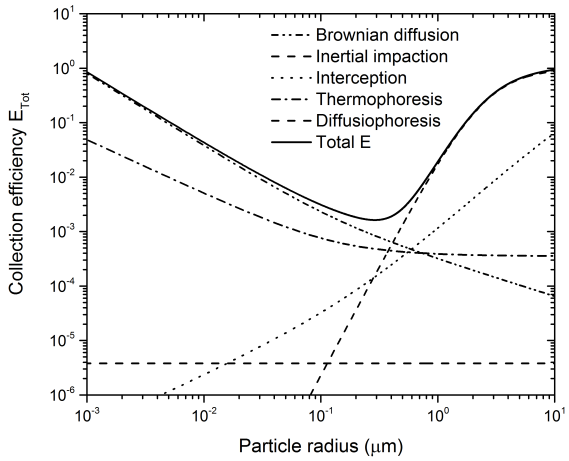

Figure 2.9: *Total collision efficiency and contribution of each collision mechanism for 80 μm droplets at 245 K and 75 % RH_w without considering the charge on the droplet or particles calculated with the theoretical formulations used by Park et al. (2005) and Andronache et al. (2006).*

With E_{Tot} known, the number of collisions between droplets and particles (N) can be calculated as follows:

$$N = K \times C \times t \tag{2.7}$$

where C is the concentration of the particles and K is the collision kernel ($m^3\ s^{-1}$) which can be physically interpreted as the volume swept by droplets per unit time and is given as (Lohmann et al., 2016)

$$K = \pi \times E_{Tot} \times (r_d + r_p)^2 \times |U - u| \tag{2.8}$$

where U and u are the fall velocities of the droplet and aerosol particle, respectively.

2.5 Droplet size sensitivity of E and N

Fig. 2.10 shows the collision efficiency and number of collisions for aerosols of varying diameters for droplet diameters of 80 μm and 26 μm. In order to investigate the effect of the droplet size and swept out volume by droplets as presented in Ladino et al. (2011b), the charges on the droplets and on the particles are ignored. Collision efficiency is calculated for time steps of 0.01 s along the droplet path in CLINCH and averaged over time. The averaging time is 2 s for 80 μm droplets and 5 s for 26 μm droplets. i.e. the time taken by droplets traced through the 40 cm length of CLINCH. The number of collisions is integrated over the total time. It is seen that the collision efficiency is higher for the smaller droplet size but the number of collisions is higher for the larger droplets, because the volume swept out by the larger droplets is larger.

2.6 Other instruments

Contact freezing was probably first mentioned in 1950 by Rau (1950) who termed it the 'Trockenkern-Effect' (dry particle effect) (Pitter and Pruppacher, 1973). Various groups have since then studied contact freezing experimentally and a review of experimental studies is presented in Ladino Moreno et al. (2013). Broadly, there are four types of instruments including CLINCH to study contact freezing. Here is a brief survey of the instruments and major observations noted using them.

- *Cold plate* : The cold plate instrument is perhaps the oldest instrument to study contact freezing. In simple terms, a droplet is placed on a solid plate coated with a hydrophobic material. The plate can be cooled to the desired temperature for contact freezing. The particles can then be sprinkled on the droplet (e.g., Gokhale and Goold, 1968; Niehaus et al., 2014). The other way to perform cold plate type contact freezing is to place the particle on the surface of the droplet (e.g., Shaw et al., 2005). Experiments were conducted by Durant and Shaw (2005); Fornea et al. (2009) where the INP was made to contact the surface of the droplet. They termed this mechanism contact freezing inside-out.
- *Wind tunnel* : In wind tunnel experiments, the droplets are suspended in an air stream (e.g., Gokhale and Spengler, 1972; Pitter and Pruppacher, 1973; Diehl and Mitra, 1998). The air stream is laden with particles whose temperature and relative humidity can be controlled. Using

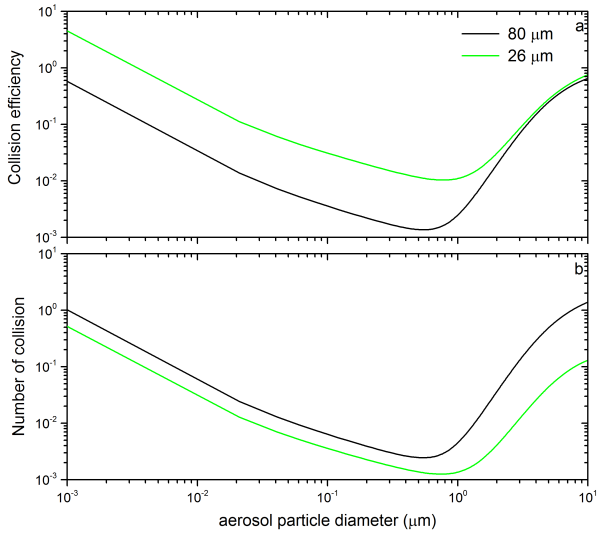

Figure 2.10: *Collision efficiency (panel a) and number of collisions (panel b) for 80 μm and 26 μm diameter droplets at 245 K and 75 % RH_w without considering the charge on the droplet or particles calculated with the theoretical formulations from Park et al. (2005) and Wang et al. (1978).*

a wind tunnel, Pitter and Pruppacher (1973) found a significantly higher efficiency for kaolinite and montmollonite when they were in contact with the surface than when they were inside the drop. Other experiments conducted by Levin and Yankofsky (1983) found 2°C higher freezing temperatures for bacteria in contact compared with immersion mode. Diehl et al. (2002) used different types of pollen in contact and immersion mode and found that median freezing temperature in contact mode were higher than in immersion mode.

- *Electrodynamic balance (EDB)*: The EDB is an instrument where a charged droplet can be suspended in an electric field. The suspended droplet then is subjected to aerosols at different temperatures. Using EDB Hoffmann et al. (2013b) found that contact freezing dominates over immersion freezing on the timescale of their experiment. Svensson et al. (2009) investigated the influence of relative humidity on contact freezing. They observed higher onset temperatures for the humidified air relative to dry air.
- *Continuous flow chamber*: The continuous flow chambers like CLINCH, droplets and particles are inserted into the chamber and interact with each other while passing through the chamber. Using CLINCH Ladino et al. (2011b) concluded that there are some hints that contact freezing is more efficient than immersion freezing.

Each of the above mentioned techniques has advantages and disadvantages. In the cold plate technique, the droplet is resting on the plate. This situation does not simulate the droplet in the atmosphere, where it is suspended in air. The number of collected INPs can be estimated by evaporating the droplet and the freezing efficiency can be estimated. A direct comparison with immersion freezing is difficult because the number of collisions is usually not known or badly constrained. The wind tunnel requires relatively larger droplets which can be suspended and observed. In the EDB, the droplet

needs to be highly charged in order to be suspended which does not represent typical atmospheric conditions and might influence the freezing efficiency. In the continuous flow chamber, it is difficult to estimate the collision rate between droplets and particles because analytical formulations for collision efficiency between the droplets and particles yield unrealistically high freezing efficiency (Ladino Moreno et al., 2013).

Chapter 3

Comparison of measured and calculated collision efficiencies at low temperatures

This chapter is published in Atmospheric Chemistry and Physics. Citation: Nagare, B., Marcolli, C., Stetzer, O., and Lohmann, U.: Comparison of measured and calculated collision efficiencies at low temperatures, Atmos. Chem. Phys., 15, 13759-13776, doi:10.5194/acp-15-13759-2015, 2015.

3.1 Introduction

Interactions of atmospheric aerosols with clouds influence the cloud properties and modify the aerosol life cycle. Depending on particle size, morphology and chemical composition, aerosol particles act as cloud condensation nuclei (CCN) and ice nucleating particles (INP) or become incorporated into cloud droplets by scavenging. Scavenging of particles in the air is one of the major processes by which the atmosphere is cleansed (Radke et al., 1980). Particles may be scavenged in-cloud and below-cloud due to collision with droplets (impaction scavenging) or by nucleation scavenging when they serve as CCN or INP (Leong et al., 1982). Below 273 K solid aerosol particles that activate to cloud droplets may induce droplet freezing in immersion mode when the temperature is further decreased. This freezing process is usually discriminated from condensation freezing, where CCN activation is immediately followed by ice formation. When interstitial aerosol particles collide with supercooled cloud droplets they may induce freezing in contact mode. This nucleation process deserves special attention, since it is reported to induce ice nucleation at higher temperature than when the same particle acts as INP in immersion or condensation mode (Durant and Shaw, 2005; Fornea et al., 2009; Ladino Moreno et al., 2013). In addition, the importance of contact nucleation for cloud glaciation also depends on the collision efficiency between aerosol and cloud droplets.

Collisions between particles and droplets can result from motion induced by turbulence and Brownian diffusion or as a result of external forces induced by gravity, electric charges, temperature or vapor gradients (Leong et al., 1982). There exist different formulations that describe collision efficiencies theoretically and give mathematical expressions for them (Slinn, 1983; Park et al., 2005; Andronache et al., 2006; Wang and Pruppacher, 1977). To validate theoretical calculations, laboratory studies have been carried out in which aerosols have been exposed to falling droplets (see Wang et al., 1978

and Ladino et al. 2011a and 2013 for references). Most of these studies have been performed at or close to room temperature with droplets of sizes that are typical for drizzle and rain drops rather than for cloud droplets. Measurements of pre- and post-rain aerosol concentrations have been used to quantify aerosol scavenging by precipitation (Davenport and Peters, 1978; Laakso et al., 2003; Chate and Pranesha, 2004; Maria and Russell, 2005). These studies often show too large washout compared with theoretical estimates based on formulations of collision efficiencies (Andronache et al., 2006). One reason for this might be an inaccurate representation of the collision processes. Accurate estimates of collision efficiencies are also needed to describe cloud glaciation. Up to date, there is lack of atmospheric INP that might explain ice nucleation at temperatures higher than -15 °C. While biological particles are discussed as candidates to close this gap (DeMott et al., 2010), an alternative explanation would be ice nucleation in contact mode. Several field studies have observed that ice crystals preferentially formed in regions of downdrafts and at cloud edges where dry air is entrained (Young, 1974). Particles contained in these air masses could initiate droplet freezing when they collide with them. To judge the importance of this process nucleation and collision efficiencies have to be quantified. The representation of heterogeneous ice nucleation in most global models still lacks a detailed description of the freezing processes depending on aerosol properties and nucleation mode (Yun and Penner, 2012; Lohmann and Hoose, 2009).

Depending on particle size and the forces acting on the particles, different collision processes have to be taken into account. In models, collision efficiencies are usually calculated as the sum of the different collision processes (Andronache et al., 2006; Bae et al., 2009; Croft et al., 2010) neglecting that the forces act together to determine the aerosol path either into or around the droplet. Trajectory calculations can be used to simulate the particle pathway, however, they need to be validated with reliable laboratory measurements (Tinsley and Leddon, 2013). Calculated collision efficiencies are quite accurate for Aitken and coarse mode particles, for which either Brownian diffusion or impaction dominates. Accumulation mode particles fall into the particle size range of the Greenfield gap (Greenfield, 1957; Seinfeld and Pandis, 2006; Ladino et al., 2011a), where Brownian diffusion and impaction are inefficient collision mechanisms. However, the collision efficiency minimum of the Greenfield gap is reduced in the presence of electric or phoretic forces and theoretical descriptions have to include the corresponding contributions to the collision efficiencies to give accurate values. Only few experimental studies have explored this part of the parameter space (Ladino et al., 2011a; Ladino, 2011) and none of them at mixed-phase cloud temperatures.

The present study investigates collision efficiencies of 200 nm and 400 nm diameter silver iodide (AgI) particles with 80 μm diameter droplets at low temperatures. A temperature range where all contacts lead to freezing is a prerequisite for the applied evaluation. This condition is fulfilled for AgI particles of 200 and 400 nm diameter for $T < 247$ K. If AgI particles were not active in contact mode, they nevertheless should lead to nucleation in immersion mode after colliding with the droplet. In addition, we provide a lower and upper limit of collision efficiency for 800 nm kaolinite particles. In our experiment droplets and particles bear charges of opposite sign giving rise to electric forces. Morever, droplets are slowly evaporating inducing thermophoretic and diffusiophoretic forces. This

study therefore provides experimental data to validate theoretical formulations exactly in this least explored parameter space range. The paper is structured as follows: Sect. 2 presents theoretical formulations of collision efficiencies from the literature, Sects. 3 and 4 describe the experimental procedure and the results. In Sect. 5, the theoretical formulations are compared with experimental results and are critically discussed. Comparison with other experimental work is presented in Sect. 6. Sect. 7 discusses improvements of theoretical formulations and atmospheric implications.

3.2 Theory

3.2.1 Collision efficiency

When a droplet falls through air, various processes can lead to the collision of aerosol particles with droplets. Theoretical formulations of these processes generally assume a flow around a spherical droplet capturing spherical particles. The collision efficiency (E) is defined as the fraction of particles in the cylindrical volume swept out by a falling droplet that collide with the droplet. A collision efficiency of unity is realized when all the particles residing in the swept out volume of a droplet collide with the droplet. When the particles follow the air stream around the droplet, E is smaller than one. E can exceed unity when particles get scavenged by wake capture. The coalescence efficiency is defined as the fraction of particles that are retained by the droplet when they collide with them. The product of E and coalescence is called the collection efficiency. Normally, it is assumed that a collision leads to the scavenging of the particle by the droplet so that the collision efficiency and collection efficiency are the same. Different processes have to be considered that cause deviations of the particle's movement from the air stream path and lead to the collision of aerosols with droplets (Ladino et al., 2011a). For the smallest particles, Brownian diffusion is the most important collision process. Brownian diffusion describes the random motion of aerosol particles resulting from collisions with carrier gas molecules. It is a strong function of particle size being most important for small aerosol particles. Large particles are most efficiently scavenged by inertial interception and impaction. Inertial impaction occurs when a particle is unable to follow the streamlines around a falling droplet and, because of its inertia, continues to move toward the drop and is eventually captured by it (Seinfeld and Pandis, 2006). Interception takes place when a particle follows the streamlines around a falling droplet sufficiently close to collide with it. The region of low collision efficiency between the small and large aerosol particles is known as the Greenfield gap. This gap may at least be partly closed when electric and phoretic effects contribute to particle collisions. Thermophoresis describes a net transport of particles in the presence of a temperature gradient in the air. Air molecules at higher temperature have a higher mean velocity and therefore impart more momentum on a particle than colder ones. The momentum on the warmer side of the particle is therefore larger and moves particles from higher to lower temperatures. Since evaporation cools the droplets and induces a temperature gradient in the surrounding air, particles are attracted by droplets for RH $<$ 100 % because of thermophoresis. Diffusiophoresis arises in the presence of a vapor concentration gradient. In the case of an evaporating droplet, there is a flux of water molecules away from the droplet, compensated by a flux of carrier

gas molecules (mainly N_2, O_2) in the opposite direction (Stephan flow) to keep the total pressure constant. Thus thermophoresis and diffusiphoresis act opposite to each other. Under typical atmospheric conditions thermophoresis dominates diffusiophoresis for aerosol particles $< 1\ \mu$m (Slinn and Hales, 1971). Finally, in case of charged particles and droplets, electroscavenging has to be considered as an additional collision process. Usually, collision efficiencies of each of these processes are formulated separately and added together to yield the total collision efficiency E_{tot}. Park et al. (2005) and Slinn (1983) proposed formulations for the collision efficiencies by Brownian diffusion (E_{Br}), interception (E_{int}), and impaction (E_{imp}). Andronache et al. (2006) gives formulations for thermophoresis (E_{Th}), diffusiophoresis (E_{Df}), and electrophoresis (E_{El}). Wang et al. (1978) use a flux model to calculate collision rate coefficients for electric and phoretic scavenging. In the following, we will outline the formulations proposed for the different collision processes.

3.2.2 Brownian diffusion, interception and impaction

In the approaches by Park et al. (2005), hereafter referred to as P05, and Slinn (1983), hereafter referred to as S83, collision efficiencies of Brownian diffusion, interception and impaction ($E_{Br,I}$) are provided. They are calculated separately and added together.

$$E_{Br,I} = E_{Br} + E_{int} + E_{imp} \tag{3.1}$$

Formulation by Park (P05)

For collision efficiencies due to Brownian diffusion and interception Park et al. (2005) follow Jung and Lee (1998) who used a resolved flow field around a system consisting of multiple spheres to obtain an analytical solution including the effects of induced internal circulation inside a liquid droplet. Due to the influence of the internal flow, the outer flow velocity around the fluid spheres becomes larger than that around solid spheres. For this reason, the streamlines pass around a fluid sphere more closely than around a solid sphere. The collision efficiency due to Brownian diffusion is taken from Park et al. (2005):

$$E_{Br}(d_p, D_d) = 2\left(\frac{\sqrt{3}\pi}{4P_e}\right)^{\frac{2}{3}}\left(\frac{(1-\alpha)(3\sigma+4)}{(J+\sigma K)}\right)^{\frac{1}{3}} \tag{3.2}$$

where α is the packing density i.e. the water volume present in a unit volume of air and σ the viscosity ratio of water to air. The hydrodynamic factors J and K are given as

$$J = 1 - \frac{6}{5}\alpha^{\frac{1}{3}} + \frac{1}{5}\alpha^2$$

$$K = 1 - \frac{9}{5}\alpha^{\frac{1}{3}} + \alpha + \frac{1}{5}\alpha^2$$

and P_e is the Peclet number defined as the ratio between the advective and diffusive transport rate and is given as

$$P_e = \frac{D_d U(D_d)}{D_{diff}}$$

where D_d is the droplet diameter, $U(D_d)$ is the terminal velocity of the drop and D_{diff} the diffusion coefficient of aerosol particles given by

$$D_{diff} = \frac{k_B T_a C_c(d_p)}{3\pi\mu_a d_p}$$

where k_B is the Boltzmann constant, T_a is the air temperature in K, μ_a is the dynamic viscosity of air and $C_c(d_p)$ is the Cunningham slip correction factor to account for non-continuum effects associated with small particles. It is given as (Ladino et al., 2011a)

$$C_c(d_p) = 1 + \frac{2\lambda_a}{d_p}\left[1.257 + 0.4\exp\frac{-1.1 d_p}{2\lambda_a}\right]$$

where λ_a is the mean free path of air molecules. The temperature dependent viscosity of air μ_a is taken from the parametrization in Pruppacher and Klett (1997). In poise units it is given as

$$\mu_a = \frac{1.718 + 0.0049 T_c - 0.000012 T_c^2}{10^{-4}}$$

where T_c is the temperature in °C. For the viscosity of water the lowest measured value at 273 K is used (1.787×10^{-3}kg m^{-1} s^{-1}).

According to Jung and Lee (1998) the collision efficiency due to interception E_{int} is given as

$$E_{int}(d_p, D_d) = \frac{1-\alpha}{J + \sigma K}\left[\frac{R}{1+R} + \frac{1}{2}\left(\frac{R}{1+R}\right)^2 (3\sigma + 4)\right] \tag{3.3}$$

where R is the diameter ratio between particle and droplet $\frac{d_p}{D_d}$.

The collision efficiency due to impaction E_{imp} is given as

$$E_{imp}(d_p, D_d) = \left(\frac{Stk}{Stk + 0.35}\right)^2 \tag{3.4}$$

where Stk is the Stokes number

$$Stk = \frac{\rho_p d_p^2 U(D_d)}{18\mu_a D_d}$$

and ρ_p is the density of the particles.

Formulation by Slinn (S83)

Slinn (1983) proposed formulations for E_{Br}, E_{int} and E_{imp} using dimensional analysis coupled with experimental data which are summarized in Seinfeld and Pandis (2006). Based on Slinn (1983), the following formulations are given in Seinfeld and Pandis (2006) and Wang et al. (2010)

$$E_{Br}(d_p, D_d) = \frac{4}{ReSc}(1 + 0.4Re^{\frac{1}{2}}Sc^{\frac{1}{3}} + 0.16Re^{\frac{1}{2}}Sc^{\frac{1}{2}}) \tag{3.5}$$

$$E_{int}(d_p, D_d) = 4\frac{d_p}{D_d}\left[\frac{\mu_a}{\mu_w} + (1 + 2Re^{\frac{1}{2}})\frac{d_p}{D_d}\right] \tag{3.6}$$

$$E_{imp}(d_p, D_d) = \left(\frac{\rho_w}{\rho_p}\right)^{\frac{1}{2}}\left(\frac{St - St^*}{St - St^* + \frac{2}{3}}\right)^{\frac{3}{2}} \tag{3.7}$$

where ρ_w and ρ_p are densities of liquid water and particles respectively. The normalizing factor $\frac{\rho_w}{\rho_p}$ is necessary to account for aerosol particles with density >1000 kg m^{-3}. *Re* is the Reynolds number representing the ratio of inertial to viscous forces in the flow and given by Pruppacher and Klett (1997).

$$Re = \exp(Y)$$

where Y is

$$\begin{aligned} Y = &-3.18657 + 0.992696X - 0.00153193X^2 - 0.000987059X^3 \\ &-0.000578878X^4 + 0.000085517X^5 - 0.00000327815X^6 \end{aligned}$$

where $X = \ln(CdRe^2)$ and $CdRe^2$ is given as

$$CdRe^2 = \frac{4D_d^3(\rho_w - \rho_a)g}{3\mu_a^2}$$

where ρ_a is the density of air, g is the acceleration due to gravity. *Sc* is the Schmidt number of aerosol particles, *St* is the particle Stokes number given as

$$St = \frac{2\tau(U(D_d) - u(d_p))}{D_d}$$

$U(D_d)$ and $u(d_p)$ are the terminal velocities of the droplets and aerosol particles, respectively. The relaxation time τ is given as (Wang et al., 2010),

$$\tau = \frac{(\rho_p - \rho_a)d_p^2 C_c}{18\mu_a}$$

St^* is the critical Stokes number above which particles may be deposited on the droplet. Note that S83 uses a slightly different formula for the Stokes number (*St*) than P05 (*Stk*). In the formulation for

E_{imp} given in Eq. (3.7) collision can happen only when $St > St^*$. The critical Stokes number is given as

$$St^* = \frac{1.2 + \frac{1}{12}\ln(1+Re)}{1+\ln(1+Re)}$$

3.2.3 Phoretic forces

Since inside the collision chamber, the droplets are evaporating, thermo- and diffusiophoretic forces also contribute to the collision efficiency. Electroscavenging has to be taken into account because particles and droplets are charged. We consider the formulations of Andronache (2004) and Andronache et al. (2006), hereafter referred to as A06, where collision efficiencies are calculated separately and added together to obtain the total collision efficiency due to phoretic forces E_{ph}

$$E_{ph} = E_{Th} + E_{Df} + E_{El} \tag{3.8}$$

where E_{Th}, E_{Df} and E_{El} are the collision efficiencies due to thermophoresis, diffusiophoresis and electrophoresis, respectively.

Formulation by Andronache (A06)

The contribution of thermophoresis to the collision efficiency is given as (Andronache et al., 2006)

$$E_{Th}(d_p, D_d) = \frac{4\gamma(2 + 0.6Re^{\frac{1}{2}}P_r^{\frac{1}{3}})(T_a - T_s)}{U(D_d)D_d} \tag{3.9}$$

where T_a is the absolute temperature of air, T_s is the absolute temperature at the droplet surface and P_r the Prandtl number for air given as

$$P_r = \frac{C_p \mu_a}{k_a}.$$

γ is given as

$$\gamma = \frac{2C_c\left(k_a + 5\frac{\lambda_a}{D_p}k_p\right)k_a}{5p\left(1+6\frac{\lambda_a}{D_d}\right)\left(2k_a + k_p + 10\frac{\lambda_a}{D_d}k_p\right)}$$

where k_a and k_p are the thermal conductivities of the air and the aerosol particles, p is the atmospheric pressure and C_p is the specific heat of air at constant pressure. The diffusiophoretic contribution to collision efficiency is given as

$$E_{Df}(d_p, D_d) = \frac{4\beta(2 + 0.6Re^{\frac{1}{2}}Sc_w^{\frac{1}{3}})(\frac{p_s^0}{Ts} - \frac{p_a^0 RH}{T_a})}{U(D_d)D_d} \tag{3.10}$$

where

$$\beta = \frac{T_a D_w}{p} \cdot \left(\frac{M_w}{M_a}\right)^{\frac{1}{2}}$$

The Schmidt number for water vapor in air is given as

$$Sc_w = \frac{\mu_a}{\rho_a D_w}$$

where D_w is the diffusivity of water vapor in air. For evaporating droplets, the diffusiophoretic contribution to E is negative. In the formulation by Andronache et al. (2006), the contribution of electric charge to the scavenging efficiency is based on Coulomb interactions between aerosol particles and droplets carrying point charges of opposite sign, leading to the capture of particles present on the streamline close to the droplet surface. The expression for this electrostatic collision efficiency is given as (Andronache, 2004; Davenport and Peters, 1978)

$$E_{El}(d_p, D_d) = \frac{16KC_cQq}{3\pi\mu_a D_d^2 d_p U(D_d)} \tag{3.11}$$

where $K = 9 \times 10^9$N m^2 C^{-2}, Q and q are the mean charges on the droplet and the aerosol particle in Coulomb units.

The flux model (W78)

An alternative formulation for phoretic and electrostatic forces is given by the flux model (Wang et al., 1978), hereafter referred to as W78. It expresses the thermophoretic force F_{Th} as (Tinsley et al., 2006b)

$$F_{Th} = -\frac{6\pi\mu_a d_p(k_a + 2.5k_pKn)k_a}{5(1+3Kn)(k_p + 2k_a + 5k_pKn)p}\frac{2(T_a - T_s)}{D_d r^2} \tag{3.12}$$

where r is the distance between the center of the droplet and the particle and Kn the Knudsen number. The term $\frac{2(T_a - T_s)}{D_d r^2}$ is the temperature gradient between the absolute temperature of the surrounding (T_a) and at the droplet surface (T_s), assuming spherical symmetry. The diffusiophoretic force can be expressed as (Tinsley et al., 2006b)

$$F_{Df} = -\frac{3\pi\mu_a d_p(0.74)D_w M_a}{(1+\alpha Kn)M_w\rho_a}\frac{2(\rho_{v,a} - \rho_{v,s})}{D_d r^2} \tag{3.13}$$

The last term in this expression $\frac{2(\rho_{v,a} - \rho_{v,s})}{D_d r^2}$ is the gradient in water vapor density. M_a and M_w are the molecular weights of air and water, $\rho_{v,a}$ and $\rho_{v,s}$ are the water vapor densities in the air far from the droplet and at the droplet surface, respectively. The parameter α is given as (Wang et al., 1978)

$$\alpha = 1.26 + 0.40\exp(-1.10Kn^{-1})$$

The formulation of the forces is strictly valid only for spherically symmetric inverse square fields. This is the case for stationary droplets. If the droplet moves, the temperature and vapor fields are not spherically symmetric. As a first order correction, mean heat and vapor ventilation coefficients f_h and f_v, respectively, can be introduced to account for the effect of air motion on the flux of heat and water

vapor (Tinsley, 2010). With this correction, the forces may be expressed as $F_{Th} = \frac{C_{Th}}{r^2 f_h}$ and $F_{Df} = \frac{C_{Df}}{r^2 f_v}$ where C_{Th} and C_{Df} are inverse square force constants for thermophoresis and diffusiophoresis, $C_{Th} = f_h F_{Th} r^2$ and $C_{Df} = f_v F_{Df} r^2$. The inverse square force constants C for the thermophoretic force and the diffusiophoretic force can be formulated as (Wang et al., 1978)

$$C_{Th} = -\frac{3\pi\mu_a d_p (k_a + 2.5 k_p K_n) k_a D_d (T_a - T_s) f_h}{5(1+3Kn)(k_p + 2k_a + 5k_p Kn)p} \tag{3.14}$$

$$C_{Df} = -\frac{3}{2}\frac{\pi\mu_a D_d (0.74) D_w M_a d_p (\rho_{v,a} - \rho_{v,s}) f_v}{(1+\alpha Kn) M_w \rho_a} \tag{3.15}$$

If electric forces are approximated by inverse square forces (repulsive for like charges, attractive for unlike charges and neglecting image charges), the inverse square force constant for electrical forces is (Tinsley, 2010)

$$C_{El} = \frac{Qq}{4\pi\varepsilon_0} \tag{3.16}$$

Using the relationship between collision efficiency and collision kernel, an effective collision efficiency can be derived from the forces. The collsion kernel K for each force constant C can be calculated as (Ladino et al., 2011a)

$$K = \frac{4\pi B_p C}{\exp(\frac{2B_p C}{D_{diff} f_p d_p}) - 1} \tag{3.17}$$

where B_p is the mobility of particles. From the collision kernel, the different collision efficiencies for each mechanism can be calculated using the relationship

$$E = \frac{4K}{\pi(D_d + d_p)^2 (U(D_d) - u(d_p))}. \tag{3.18}$$

3.3 Experimental setup

3.3.1 Instrumentation

Our collision nucleation chamber (CLINCH) is similar to the one used by Ladino et al. (2011a,b) for contact freezing studies with some modifications to observe the frozen fraction of droplets at different times. It is a continuous flow chamber which consists of two parallel plates separated by 1 cm width with side windows for the detector. Both chamber walls are held at the same temperature and are covered with ice, leading to an environment that is saturated with respect to ice and subsaturated with respect to water. Relative humidity in the chamber depends on the chamber temperature. The droplet generator from Bremen University is placed at the center top of the chamber. The droplet generator contains a piezo element which can produce 80 ± 3 μm diameter droplets with a frequency of 100 droplets per second (Ulmke et al., 2001). With this setting the distance between two successive droplets is about 2 mm when the droplet acquires its terminal velocity of 0.186 m s^{-1}. The droplets

are generated with pure water (Milli-Q, 18.2 MΩ) at a temperature of 281 K. The relaxation time for a droplet to reach its terminal velocity is 0.2 s and the temperature relaxation time is about 0.6 s when the chamber is kept at 235 K.

Figure 3.1 shows the droplet surface temperature (panel a), the difference between droplet surface and chamber temperature (panel b) and evolution of droplet diameter (panel c) at 255, 245 and 235 K. Aerosol particles enter the chamber at the top in an air flow from both sides and can interact with the liquid droplets while passing through the chamber. The flow through the chamber is laminar and should not show any turbulence. The terminal velocity of the AgI aerosol is too low to contribute to the flow velocity. The fall velocity of the aerosol particles is therefore taken as the flow velocity averaged over the whole cross section of the chamber, which equals 0.017 m s^{-1} for an air flow of 1 liter per minute through the chamber. In CLINCH, aerosol particles and cloud droplets can collide leading to freezing of the cloud droplets via contact freezing. With the modified setup, it is possible to observe the frozen fraction of droplets at lengths of 40 cm and 80 cm. The residence time of droplets at these two lengths are 2 s and 4 s, respectively. Since the droplets have to cool down to the chamber temperature after injection, the residence time at the desired temperature is shorter (see Fig. 3.1). In the case of the lowest investigated temperature of 235 K it is reduced to 1.4 s and 3.4 s for chamber lengths of 40 cm and 80 cm. At the end of the chamber, a Condensation Particle Counter (CPC, TSI 3772) is connected to measure the concentration of the aerosol particles. In order to discriminate between water droplets and ice crystals, an in-house developed Ice Optical Detector (IODE) (Nicolet et al., 2010) was used. In order to avoid the presence of two droplets simultaneously in the laser beam, a new laser was installed (402 nm, Schaefter + Kirchhoff laser Makroliniengenerator13LTM) providing a rectangular instead of a circular laser beam. The fall velocity of the droplets is 0.210 m s^{-1} calculated as the sum of the terminal velocity of the droplets (0.186 ms^{-1}) and the flow velocity at the center of the chamber (0.024 ms^{-1}) using the formula by Rogers (1988) neglecting the temperature gradient term. The Reynolds number of the air flow is calculated to be 12 and the droplets Reynolds numbers are about 0.65 which ensures that the chamber flow is not turbulent. With such conditions inside the chamber, the relative humidity around the column of droplets will increase only slightly due to evaporation of droplets. Our calculations show that this increase is $<$ 1% and too small to trigger deposition nucleation on the aerosol particles. Stetzer et al. (2008) showed that deposition nucleation on silver iodide particles can take place only when the relative humidity with respect to ice is larger than 105 %.

3.3.2 Aerosol preparation

Silver iodide particles were produced by mixing of 0.1 M potassium iodide and 0.1 M silver nitrate solutions. 10 ml of the potassium iodide solution was diluted with 80 ml distilled water and 10 ml of the silver nitrate solution were added. The AgI precipitate was then decanted to 40 ml and 60 ml distilled water was added to the solution. From this solution aerosol particles were produced by atomizing. The particles were then dried to RH $<$ 10 % at room temperature. These dried particles passed through a mixing volume to obtain a relatively constant concentration of particles. At the exit

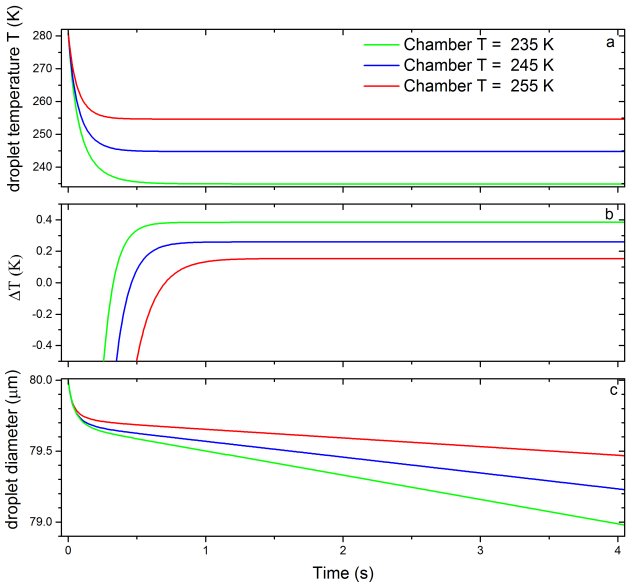

Figure 3.1: *Droplet characteristics at experimental conditions calculated along the pathway through the chamber with timesteps of 0.01 s. Panel (a) shows the surface temperature of the droplet, panel (b) shows the difference between the surface temperature of the droplet and the chamber temperature and panel (c) shows the droplet diameter at chamber temperatures of 235, 245 and 255 K. These parameters are calculated using equation 13-15b of Pruppacher and Klett (1997).*

of the mixing volume, a cyclone with 1 μm cutoff size was used and the particles were then passed to the Differential Mobility Analyzer (DMA). The DMA column voltage was set to negative so that only negatively charged particles got into the air stream. The size distribution of AgI particles is lognormal with a mode diameter of 80 nm. Size selected 200 and 400 nm silver iodide particles are in the downslope of the size distribution of particles which were produced. So the contribution of double or triple charged particles in the outflow of the DMA was < 10 %. These size selected particles were passed to the chamber via a concentration control system in order to select a particular concentration of particles. The aerosol concentration was measured at the end of the chamber with a CPC.

3.3.3 Charge measurement

The droplets obtain a variable number of charges when the stream of droplets is injected from the droplet generator and the charge can be measured with various methods. We determined the charge off-line of the experiment by passing the droplet stream through a capacitor consisting of two parallel plates which were connected to a DC voltage supply. The droplet generator was placed exactly at the top edge of the plates. These two plates were kept at 6 mm distance from each other and a DC voltage was applied. Due to the presence of the charge on the droplets, the droplets can be either deflected toward the positively or negatively charged plate. Multiple measurements were performed at different times in order to obtain the average charge on the particles. Fig. 3.2 shows the individual measurements of the charge on the droplets. The charge on the droplets varied from 0.16 fC (1000 e)

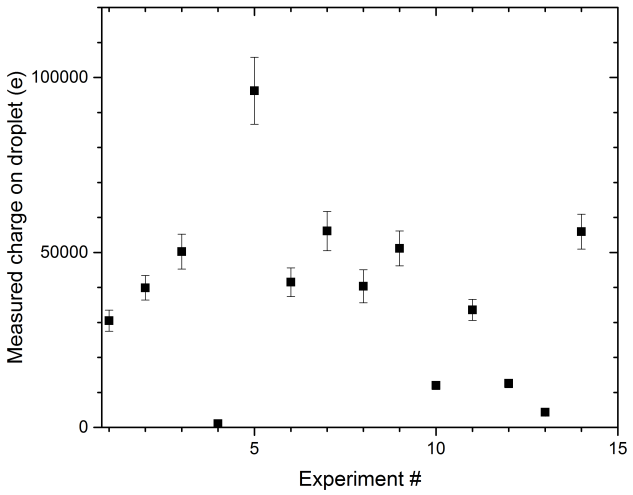

Figure 3.2: *Measured charge on droplets at different times. Error bars represent uncertainties in charge measurement due to the uncertainty in the measurement of the vertical distance traveled by the droplet. The mean charge averaged over all the experiments is 39000 e with a standard deviation of 20000 e.*

to 80 fC (50000 e). It remained the same once the droplet generator was turned on but could switch to a different value when the droplet stream was turned off and turned on again. The mean charge on the droplets was about 65 fC (39000 e $\pm$ 20000 e).

3.3.4 Experimental procedure

The collision ice nucleation experiments were conducted at temperatures between 261 K and 236 K. Initially the chamber was evacuated for 5 min and then cooled to 258 K. To cover the walls with a thin layer of ice the chamber was filled with distilled water for 10 s and then flushed out. The chamber was again evacuated for 3 min and the detector was mounted. When the desired temperature of the chamber was reached, the droplet generator was turned on and droplets were observed in the detector. This blank experiment without aerosol particles was performed at each temperature in order to ensure that there is no droplet freezing without particles. After the blank experiments, the aerosol flow was turned on and the actual experiment was performed. After completing the experiment for one temperature, the temperature of the chamber was lowered in steps of 2 to 3 K until the homogeneous freezing temperature was reached.

3.4 Experimental results

Figure 3.3 shows the frozen fraction of droplets as a function of temperature for the investigated concentrations of the 200 nm and 400 nm silver iodide particles and residence times of 2 s (panel a, panel c) and 4 s (panel b, panel d). Error bars shown represent an uncertainty in the frozen fraction due

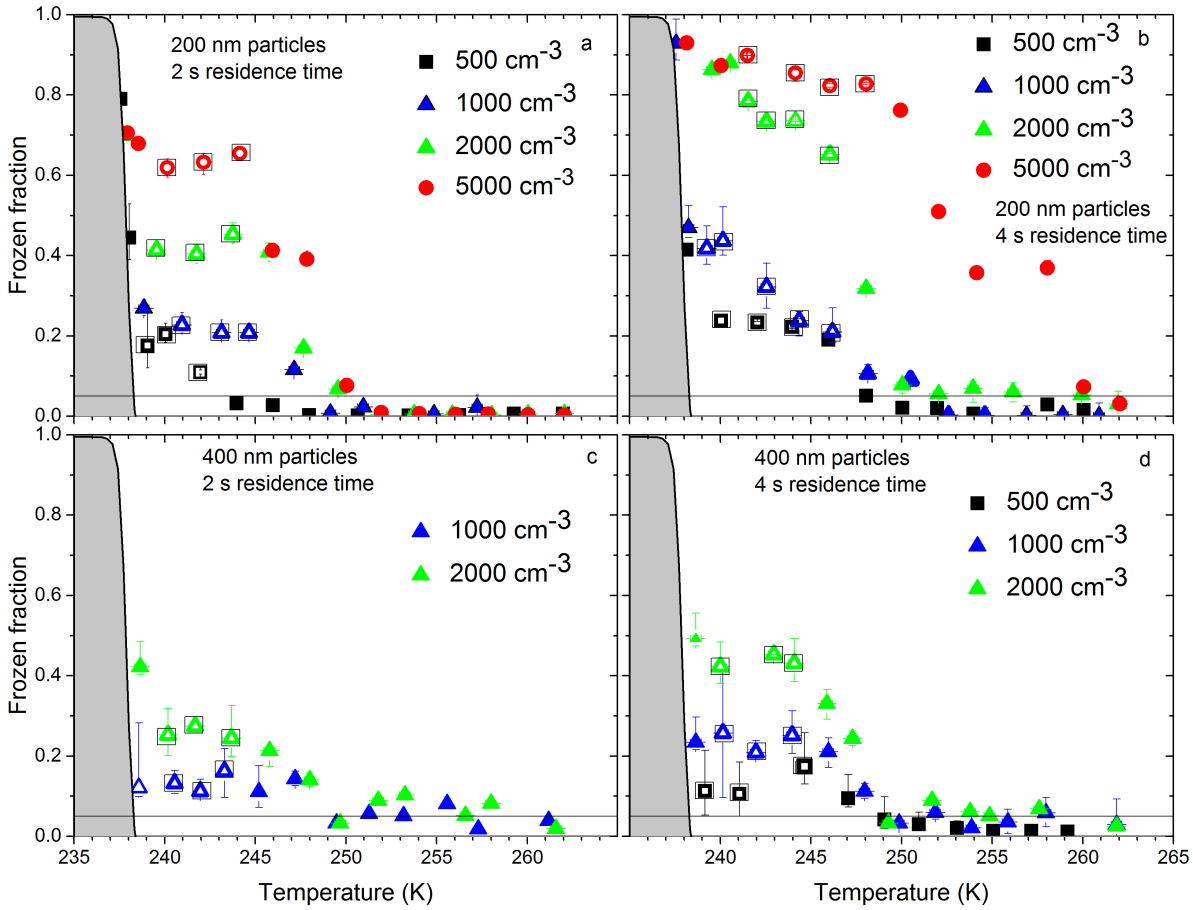

Figure 3.3: *Frozen fraction against chamber temperature for droplet residence times of 2 s (panel a, panel c) and 4 s (panel b, panel d) for different concentrations of silver iodide and 2 different sizes 200 nm (panel a, panel b) and 400 nm (panel c, panel d). The gray shaded area indicates homogeneous freezing from blank experiments. The horizontal black line indicates the detection limit of the detector determined from the blank experiments. Open symbols indicate the experiments used for the calculation of collision efficiencies.*

to the classification (liquid or ice) uncertainty originating from the measurement errors of the IODE detector (Lüönd et al., 2010). As the chamber temperature was decreased the frozen fraction started to rise and after reaching a certain value it remained constant. The frozen fraction plateau is reached at about 245 K. A frozen fraction of 1 is not reached even for the lowest investigated temperature of 238 K. According to classical nucleation theory, homogeneous nucleation becomes effective only for $T < 238$ K (e.g Ickes et al. (2015)). We assume that for $T < 245$ K heterogeneous freezing on AgI particles is so efficient that each collision of a particle with a droplet leads to the immediate freezing of the droplet (freezing efficiency of 1) and the frozen fraction plateau is reached. For $T > 245$ K, the probability of droplet freezing is < 1, and the collision of a particle with a droplet does not necessarily induce freezing. For $T < 245$ K, frozen fractions increase with increasing particle concentration from 500 cm^{-3} to 5000 cm^{-3} without reaching a value of 1 and they are higher for 4 s residence time than for 2 s residence time. This is in accordance with immediate contact freezing once the droplet has

collected a particle. This limits the contact freezing by the probability that a droplet actually captures a particle while it is falling through the chamber. If the freezing probability for T $<$ 245 K is assumed to be 1, this temperature range can be used to deduce collision efficiencies from our experimental data. We therefore define data points that correspond to unity freezing probability and use them to derive experimental collision efficiencies. These points are indicated by open symbols in black rectangles in Fig. 3.3. With our preparation method for AgI, the concentration of 800 nm diameter particles was too low to keep a constant concentration during the time needed for an experiment. To derive collision efficiency for 800 nm particles, we therefore used kaolinite particles. The experimental setup for these measurements was the same as for AgI except for the particle generation method, which is described in Nagare et al. (2015b).

Figure 3.4, shows the evolution of the frozen fraction as a function of the residence time in the chamber calculated as

$$FF = 1 - e^{-E_{exp} K_{geo} C_{par} t} \tag{3.19}$$

where K_{geo} is the geometrical area swept out by the droplet per unit time t. C_{par} is the particle concentration and E_{exp} is the collision efficiency that fits to the experimental results best. K_{geo} was simulated for each 0.01 s time step to take the size change of the droplet and change in terminal velocity into account. Since the collision efficiency should be the same for all concentrations and not depend on residence time, E_{exp} was determined by simultaneously minimizing the difference between the mean values of frozen fraction indicated by the symbols in Fig. 3.4 and the frozen fraction calculated with Eq. (3.19). In our experiment the droplets are evaporating slowly which decreases the K_{geo} over time. We take the average of collision efficiency over the residence time in the chamber, thus small changes in K_{geo} also get accounted. K_{geo} decreases almost linearly with highest values at the first time step ($\approx 1.06 \times 10^{-3}$ cm^{3}s^{-1}) and the lowest one in the last ($\approx 1.042 \times 10^{-3}$ cm^{3}s^{-1}). This yielded value of $E_{exp} = 0.13$ for 200 nm particles in reasonable agreement with all data points taking experimental uncertainties into account. To show the sensitivity of the frozen fraction to the assumed collision efficiency, curves for $E = 0.02$ (according to the theoretical formulation of P05 and W78 are also given in Fig. 3.4 as dashed lines.

3.5 Comparison of the different formulations of collision efficiency

Figure 3.5 shows the different contributions to the total collision efficiency of a 80 μm droplet as a function of AgI particle diameter calculated with the theoretical expressions of Sect. 2 for the experimental conditions of the CLINCH chamber, which is kept at ice saturation for $T = 245$ K. Temperature and vapor pressure gradients between the droplet surface and the surrounding are calculated as well as the slow evaporation of the droplet along its path through the chamber in time increments of 0.01 s. Mean collision efficiencies for the whole chamber length are obtained by averaging over the individual 0.01 s increments. In this simulation, the droplet has a diameter of 80 μm when it enters the chamber and shrinks to 79 μm at the end of the chamber. This slow evaporation induces a temperature gradient between the surrounding and the droplet ($T_a - T_s = 0.3$ K) leading to thermophoresis.

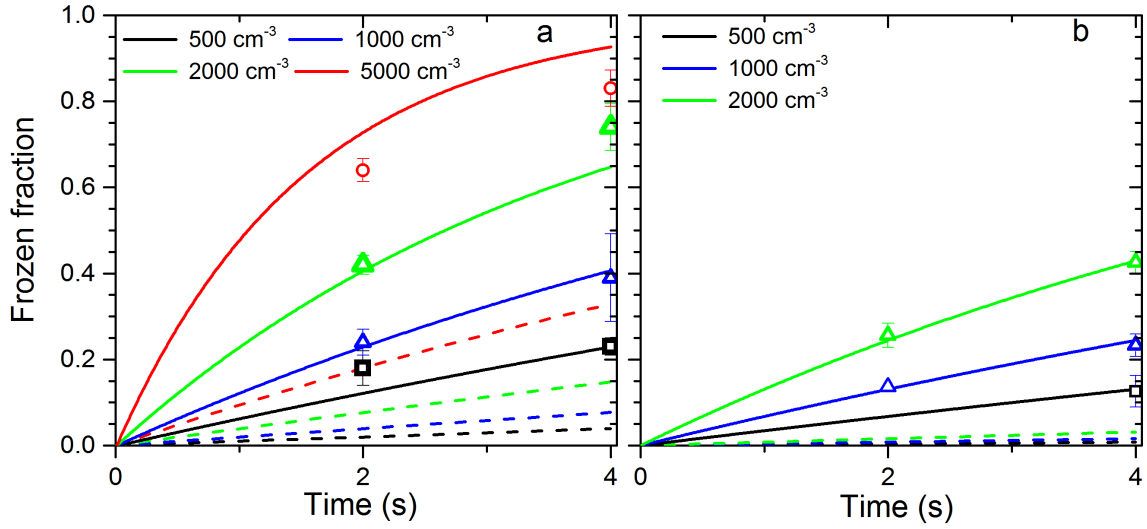

Figure 3.4: *Evolution of the frozen fraction as a function of the residence time in the chamber calculated with Eq.3.19 for the different particle concentrations from 500* cm^{-3} *to 5000* cm^{-3}*. Solid lines are calculated assuming a collision efficiency* $E_{exp} = 0.13$ *and dashed lines for* $E = 0.02$ *for 200 nm particle in panel (a) while in panel (b)* $E_{exp} = 0.07$ *and* $E = 0.004$ *for 400 nm particles. Symbols and uncertainty bars give the average and standard deviation of the frozen fraction plateau values indicated by open symbols in Fig. 3.3.*

AgI particles have a density of 5600 kg m^{-3} and one elemental charge since they passed through a DMA for size selection. Major uncertainties are associated with the charge of the droplets. For the calculations shown in Fig. 3.5, a charge of 50000 e of opposite sign to that of the particles was assumed. Panel (a) of Fig. 3.5 shows the collision efficiencies of Brownian diffusion, interception and impaction for the formulations P05 described in section 3.2.2 and S83 described in section 3.2.2. The formulations for Brownian diffusion and interception by P05 and S83 show a very similar particle size dependence, but the values using S83 are by about a factor of three higher for E_{Br} and even an order of magnitude higher for E_{int}. While the formulations of P05 are derived theoretically from a resolved flow field, S83 used dimensional analysis coupled with experimental results. Although the formulation of P05 takes the increased collision efficiency for a flow around a liquid droplet compared with a flow around a solid sphere explicitly into account, it yields lower collision efficiencies than the one by S83. The formulation of S83 crucially depends on the accuracy of the experiments forming the basis for the dimensional analysis. E_{imp} using S83 drops off to zero for a particle diameter $d_p < 2$ μm because of the critical Stokes number in the formulation of impaction below which the impaction of particles on droplets is zero. For particles smaller than 0.1 μm, Brownian diffusion is the most dominant mechanism and for particles above 1 μm diameter, impaction dominates for the formulation of P05. For the 200 nm particles used in our experiments the collision efficiency by Brownian diffusion is by more than an order of magnitude more efficient than interception and impaction.
Panel (b) of Fig. 3.5 shows the collision efficiencies due to individual contributions for thermophoresis and electrophoresis. Diffusiophoresis results in a repulsive force rendering the collision efficiency

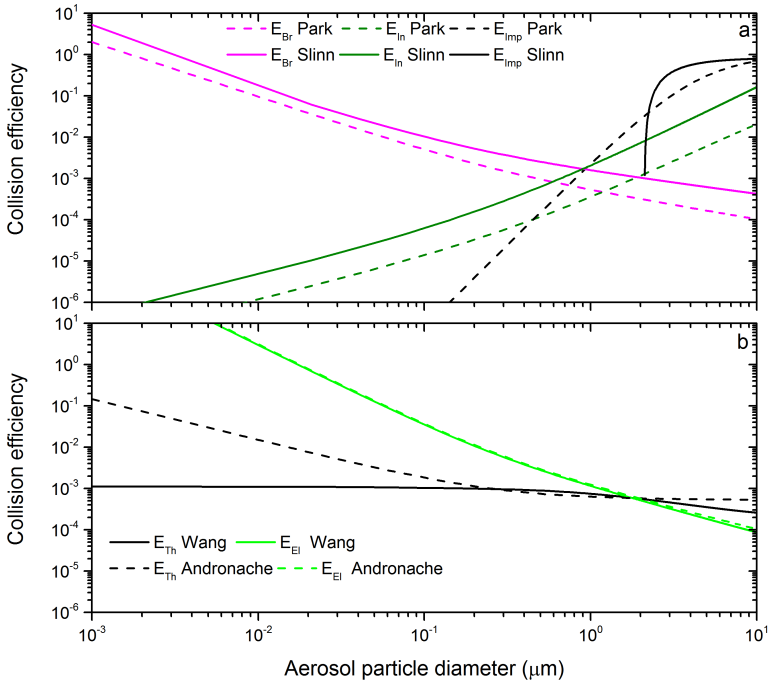

Figure 3.5: *Calculated collision efficiency for a droplet of 80 μm diameter as a function of aerosol particle diameter at a temperature of 245 K and ice saturation. The contributions of Brownian motion, interception and impaction are shown in panel (a) for the formulations by Park et al. (2005) (P05) and Slinn (1983) (S83). The contributions for thermophoresis, and electrophoresis are shown in panel (b) for the formulations by Andronache et al. (2006) (A06) and Wang et al. (1978) (W78).*

negative for the formulation of A06 ($\approx -10^{-4}$) and too small to be represented in Fig. 3.5 using W78 ($\approx 10^{-28}$). While collision efficiencies by electrophoresis are almost identical, considerable differences for thermophoresis in particle size dependence can be found comparing the formulations A06 and W78. A06 predicts a decrease of collision efficiency for increasing particle size whereas W78 shows hardly any dependence on aerosol particle diameter. The expression by W78 is formulated for the slip regime (Kn $<$ 0.1) and applies to larger particles (Leong et al., 1982). The expression of A06 applies to the free molecular regime (Kn $>$ 10) and small particles (Slinn and Hales, 1971). Electrophoresis contributes the most for the smallest of the aerosol particles i.e. between the range of 1 nm to 0.1 μm diameter.

3.5.1 Temperature dependence of thermophoretic collision efficiency

Panel (a) of Fig. 3.6 shows the dependence of the collision efficiency due to thermophoresis for T = 263 K, 248 K and 233 K, keeping the other parameters the same as used for Fig. 3.5. As the temperature decreases the effect of thermophoresis also decreases because the evaporation rate of the droplet decreases and therefore also the temperature gradient decreases. On the other hand, the collision efficiency by thermophoresis is also influenced by the decreasing relative humidity with decreasing temperature from 90.6 % at 263 K to 78.2 % at 248 K and finally to 67.8 % at 233 K

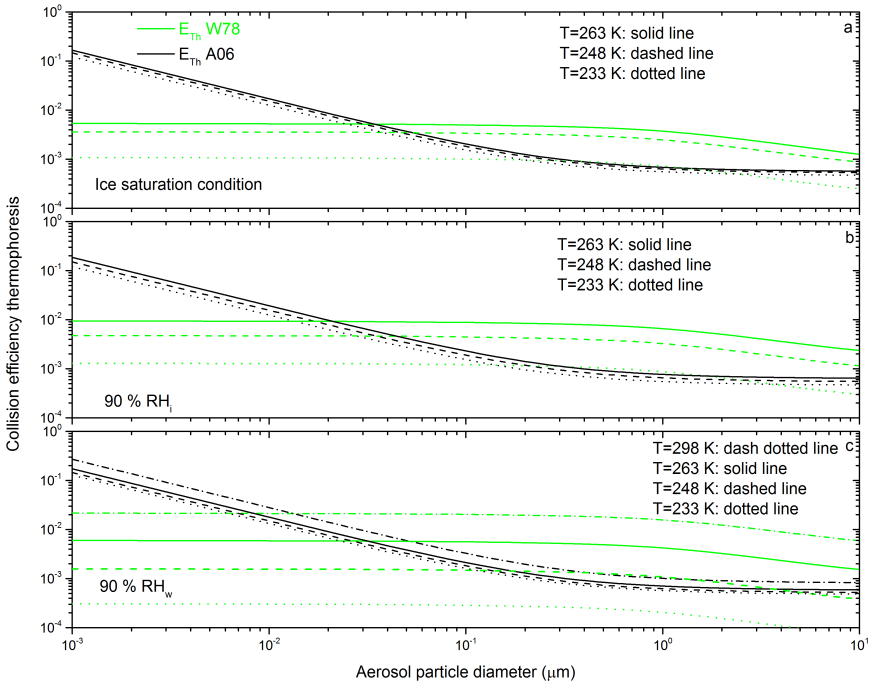

Figure 3.6: *Dependence of thermophoresis on aerosol particle diameter following Andronache et al. (2006) (A06) and Wang et al. (1978) (W78) for a droplet of 80* μm *diameter. Panel (a) at ice saturation for temperatures of 263 K, 248 K and 233 K. Panel (b): at 90 % relative humidity with respect to ice. Panel (c): at 90 % relative humidity with respect to water.*

because the chamber is kept at ice saturation conditions. To take apart the influence of temperature and relative humidity, panel (b) of Fig. 3.6 shows the dependence of thermophoresis on temperature keeping the environmental relative humidity with respect to ice at 90 % and panel (c) by keeping the environmental relative humidity with respect to water at 90 %. In addition to that, curves at $T = 298$ K are also shown as dash dotted lines in panel (c) for a better comparison with other studies. The temperature dependence of W78 is much stronger than the one of A06. Since for our experimental settings, diffusiophoresis results in a repulsive force rendering the collision efficiency negative or zero, we do not show here the temperature dependence of diffusiophoresis. The combined description of thermophoretic and diffusiophoretic forces indicate that for our experimental conditions of evaporating droplets in the presence of rather small aerosol particles, thermophoresis should exceed diffusiophoresis (Slinn and Hales, 1971). However, disagreement still exists between experiments and model predictions concerning the prevalent forces as a function of particle radius (Santachiara et al., 2012; Prodi et al., 2014).

3.5.2 Charge dependence of electrophoresis

Figure 3.7 shows the droplet charge dependence of electroscavenging for the formulations of A06 and W78. Calculations are shown for droplet charges of 5000 e, 10000 e, and 50000 e and a particle charge of 1 e. All other parameters are the same as for Fig. 3.5. Charges on droplets and particles are

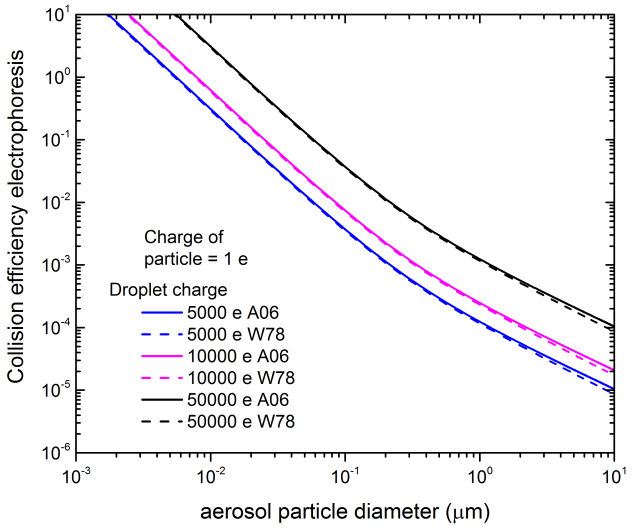

Figure 3.7: *Dependence of electrophoresis on droplet charges for the formulations of Andronache et al. (2006) (A06) and Wang et al. (1978) (W78). The legend indicates the elementary charge on the droplets. The aerosol particles carry one elementary charge.*

of opposite sign. Both formulations show the same charge and particle size dependence with a strong increase of collision efficiencies with increasing droplet charge and decreasing particle size. If the charges of droplets and particles were of the same sign, particles would be repulsed from the droplets and the collision efficiency would be effectively zero, since the formulations of A06 and W78 both assume point charges located in the middle of the particles and droplets and do not take into account image charge effects. When aerosol particles come close enough to water droplets, image charges on the conducting droplets can lead to attraction even if the charges on the particle and on the droplet are of the same sign (Tinsley et al., 2000). When the radial component of the flow carries the particle towards the droplet as fast as the particle is repulsed, then the particle will pass through the distance of maximum repulsion and in most cases collide with the droplet, as the image forces increase very rapidly at close distance. Tinsley et al. (2000) show in their Fig. 5, panels (c) and (d), that for particles with diameters $>$ 500 nm and charges of 5 - 500 e electroscavenging by droplets with 84 μm diameter and a charge of 500 e does not depend on whether the charges of droplets and particles are of the same or opposite sign. Particles with diameters $<$ 200 nm are strongly repulsed from the droplets when their charge is of the same sign as the droplet charge and strongly attracted when the charges are of opposite sign. For particles with diameters of 200 nm, collision efficiencies are by a factor of 2 larger in case of opposite sign than in case of same sign. Also for our experimental situation image charges will diminish the difference between electroscavenging between particles and droplets with like and opposite charges. However, the effect might be smaller because the AgI particles carry only one elementary charge resulting in a smaller image force compared to the situation shown in Tinsley et al. (2000), and the droplets are highly charged, increasing the radius of repulsion that has to be overcome until attractive image forces set in.

3.5.3 The total collision efficiency E_{Tot}

Figure 3.8 shows the total collision efficiency for different combinations of the theoretical formulations for the same experimental conditions as in Fig. 3.5. All combinations of collision efficiencies are dominated by electrophoresis for particle diameters $<$ 100 nm and by impaction for diameters $>$2 μm. In this range Brownian diffusion, electrophoresis and thermophoresis contribute significantly to the total collision efficiency. For 200 nm particles, the total collision efficiency is lowest (0.01) for the combination P05 and A06 and highest (0.02) for the combination S83 and W78. In our approach total collision efficiencies are obtained by adding up collision efficiencies of the different processes with values ≥ 0. Negative collision efficiencies were not considered since they lack physical meaning. In trajectory calculations (Tinsley, 2010; Tinsley and Leddon, 2013) the simultaneous action of the different forces on the particle can be investigated. These calculations show that e.g. for small particles, the total collision efficiency can be lower than the one by Brownian diffusion alone when Brownian diffusion is diverted by repulsion of particles carrying charges of the same sign as the droplet (Tinsley et al., 2006b). Table 3.1 shows the dependence of the total collision efficiency on droplet and particle sizes used in the experiments for P05 and W78 (red line in Fig. 3.8). Other formulations show similar variations in total collision efficiency. In addition, it lists the sensitivity of the total collision efficiency to the density of the particle and variation in atmospheric pressure. For both these parameters, the calculated collision efficieny sensitivity is found to be negligible. It should be noted that impaction collision efficiency in S83 is normalized by the density of the particle but this effect can only be seen for particles larger than 2 μm. The listed particle densities are the ones of silver iodide (5600 kgm^{-3}) and potassium nitrate (2100 kgm^{-3}).

3.6 Comparison with previous experimental work

A direct comparison of our experimental results with other measurements of collision efficiencies is not possible because collision efficiency is sensitive to many parameters, which are only partly the same in different experiments. Important parameters that determine the collision efficiency are droplet and particle sizes, charges on droplets and particles, relative humidity and temperature. Laboratory studies summarized by Wang and Pruppacher (1977) and Ladino et al. (2011b) have all been performed at or close to room temperature. In a critical review, Wang and Pruppacher (1977) criticize most older studies for insufficient control of relative humidity, insufficient control or knowledge of charges on droplets and particles, and the use of large droplets so that the terminal velocity is not reached during the experiment. In the following, the relevant studies to compare with our data are summarized. Lai et al. (1978) investigated collection efficiency of AgCl aerosol particles by freely falling water droplets in nitrogen. For 300 nm, 500 nm, and 900 nm diameter particles scavenged by 1.24 mm diameter droplets, they measured collection efficiencies of 0.107, 0.016 and 0.045, respectively. These results are in agreement with ours considering the larger particle and droplet sizes employed by Lai et al. (1978). When 1.24 mm diameter droplets were charged with surface charge densities of -0.7×10^{10} to -3.0×10^{10} C cm^{-2} and $+0.8 \times 10^{10}$ to $+3.1 \times 10^{10}$ C cm^{-2}, the collec-

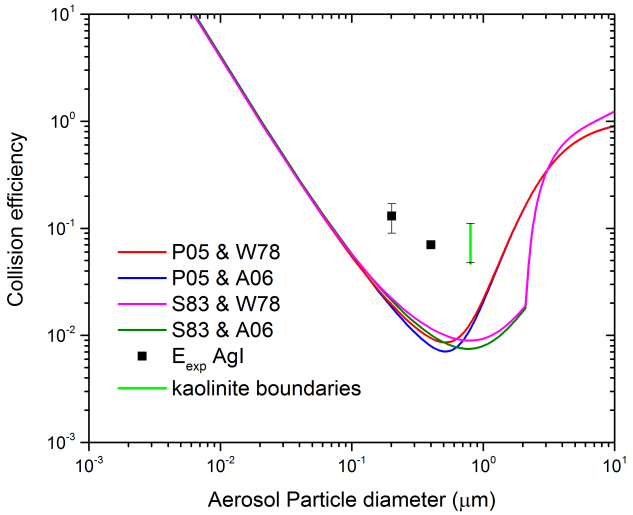

Figure 3.8: *Total collision efficiency for a droplet of 80 μm diameter as a function of aerosol particle diameter at 245 K and ice saturation. The total collision efficiency is the sum of all individual contribution. The experimentally determined collision efficiency for 200 nm and 400 nm silver iodide particles colliding with 80 μm water droplets is shown by squares. The error bars represent the uncertainty level derived by optimizing the collision efficiency to the upper and lower limits of experimentally determined frozen fractions shown by the symbols in Fig. 3.4 The green line shows the upper and lower bound for 800 nm kaolinite particles. Since the assumption of freezing efficiency of 1 is not valid at any temperature for kaolinite, no plateau region is available for evaluation. We can therefore only give upper and lower boundaries of collision efficiency for these particles.*

tion efficiency for 480 nm diameter particles increased from 0.017 to 0.023 - 0.067 irrespective of the sign of the charge. This increase illustrates the effect of image charge that is also expected to influence our collision efficiencies. Byrne and Jennings (1993) and Barlow and Latham (1983) obtained collision efficiencies in reasonable agreement with Lai et al. (1978) for similar experimental conditions. Radke et al. (1980) performed airborne measurements of aerosol size distributions before and after rain or snow showers in aged air masses and found good agreement with theoretical calculations for particles ≥ 1 μm in diameter, where inertial impaction dominates scavenging. For the submicron aerosol particles the Greenfield gap was narrower than predicted by theory. Measured scavenging collection efficiencies ranged typically from 0.1 - 0.7 for 200 nm diameter particles which is in general agreement with our results, and dropped to $<$0.05 in the size range 400 - 1000 nm. Beard (1974) determined collection efficiencies of uncharged 700 - 900 nm diameter particles with 0.40-0.85 mm diameter droplets with charges of 10^{-5}, 10^{-4}, and 10^{-3} esu (1-100 fC) at 99 % RH and a temperature of 24°C. They found increasing collection efficiencies with increasing droplet charge of 0.5×10^{-4} - 3.7×10^{-4} for 10^{-5} esu, 2.3×10^{-4} - 11.6×10^{-4} for 10^{-4} esu, and 12.2×10^{-4} - 16.1×10^{-4} for 10^{-3} esu, illustrating again the influence of image charge. Their considerably lower values compared with ours can be partly ascribed to the larger particle and droplet sizes and partly to the absence of phoretic forces. The increase of collection efficiency due to phoretic forces can be seen comparing with the results from Lai et al. (1978) performed at low RH, which are two orders of magnitude larger

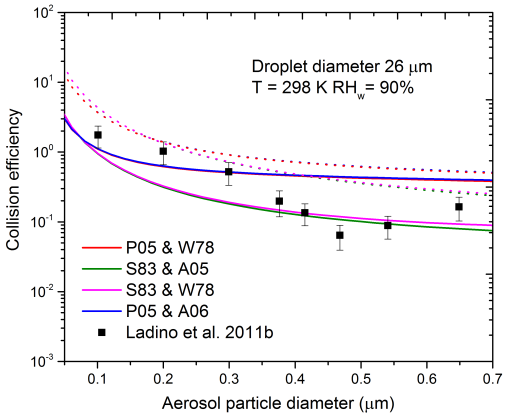

Figure 3.9: *Total collision efficiency for a droplet of 26 μm diameter as a function of aerosol particle diameters at a temperature of* 298 K *and 90 % relative humidity with respect to water. The black squares indicate the measured collision efficiency by Ladino et al. (2011a). We have assumed charges of 10000 e (solid lines) and 50000 e (dotted lines).*

for similar particle and droplet sizes. Wang and Pruppacher (1977) determined collection efficiencies for 500 nm diameter indium acetylacetonate particles collected by water droplets at 23 % RH and 22°C. They observed for 340 μm diameter droplets with charges of 1.2×10^{-3} esu (15 e) a collection efficiency of 1.8×10^{-2}. The lower value compared with ours can be explained by the larger particle and droplet size and the lower charge in the experiment of Wang and Pruppacher (1977). Ladino et al. (2011a) determined collision efficiencies for aerosol particles scavenged by cloud droplets in CLINCH using 26 μm diameter droplets. They exposed freely falling water droplets at 298 K and 90 % RH to an aerosol consisting of lithium metaborate particles with diameters between 0.1 and 0.66 μm and observed collision efficiencies between $E = 0.08 - 1.75$. $E_{tot} > 1$ are obtained because of the high efficiency of Brownian diffusion for small particles. Fig. 3.9 shows that their experimental results are in agreement with the theoretical predictions. Ardon-Dryer et al. (2015) determined collision efficiencies between Polystyrene Latex Spheres (PSL) with radii from 0.125 - 0.475 nm and 43 μm diameter droplets charged with 400 ± 40 e. Collision efficiencies ranged from 5.7×10^{-3} to 8.6×10^{-3} for $RH = 15$ % and from 6.4×10^{-3} to 2.2×10^{-2} at 88 % RH. These values are lower than the ones reached in this study which may be explained by the lower charge on the PSL spheres.

3.7 Discussion

3.7.1 Discrepancies between theoretical and experimentally derived collision efficiencies

The experimentally derived collision efficiencies are almost one order of magnitude higher than the theoretical ones. It is unlikely that the experimentally derived ones are by this amount too high.

The assumption that every collision leads to droplet freezing can only result in too high collision efficiencies. A conceivable process that would result in an overestimation of the collision efficiency could be that droplet freezing would influence the velocity of the droplets in such a way that frozen droplets collide with liquid ones. However, considering the sequence of frozen and liquid droplets, such a bias does not seem to exists. Brownian diffusion is the main collision mechanism for small particles in the absence of charges and one of the dominating contributions to the total collision efficiencies for the 200 nm diameter particles investigated in this study. The formulation of S83 predicts higher collision efficiencies than the one of P05 for Brownian diffusion and combinations with S83 for total collision efficiencies yield higher values. However, it is unlikely that uncertainties in the theoretical formulations of this process can account for the total discrepancy between experimentally derived and calculated collision efficiencies. Contributions of impaction and interception to total collision efficiencies are more than one order of magnitude lower than the one of Brownian diffusion and therefore uncertainties in these formulations are not likely to fill the gap between experimentally derived and calculated collision efficiencies. The assumption that the charge on the droplet is 50000 e and of opposite sign to the one on the particles results in the highest expected value for collision efficiencies due to electric forces. Accounting for image forces would only increase collision efficiencies in the case of same charges on particles and droplets. The processes with the highest uncertainties are the ones arising from thermophoretic and diffusiophoretic forces. While diffusiophoresis leads to a repulsive force and does not contribute to the total collision efficiencies under our experimental conditions of evaporating droplets, thermophoresis is attractive and a dominating contribution. In the combined treatment of electrical, thermophoretic and diffusiophoretic forces, collection efficiencies can be lower than when efficiencies are treated separately and added up. In trajectory calculations (Zhou et al., 2009) Brownian motion, electrical and phoretic processes are treated together. Since the diffusiophoretic force of an evaporating droplet is repulsive it can counteract attraction by thermophoresis and Brownian motion. A study on the simultaneous effect of phoretic processes performed by Slinn and Hales (1971) showed that thermophoresis dominates diffusiophoresis for evaporating droplets in quasi-steady state conditions for vapor diffusion and heat conduction. Similarly, the same charges on particles and droplets will divert particles away from the droplets at distances where mirror charges are too weak to lead to attraction and decrease the collision efficiency (Tinsley et al., 2000). For the calculation of collision efficiencies spherical particle shapes have been assumed. This assumption is valid for liquid or glassy particles but not for solid ones, which have complex morphology with significant deviations from sphericity. The drag on a nonspherical particle depends on its orientation, which in turn is affected by shear in the flow field. Leong et al. (1985) estimated in a theoretical study the effects of oblate and prolate particle rotation in shear flow and shape dependency of the thermophoretic force of evaporating 30 μm radius droplets. The results indicate that the orientation effects of the shear flow will tend to decrease the thermophoretic force on the particle toward the drop surface in the size regime where phoresis dominates beacuse the non spherical particle aligns along the streamlines and the velocity component of the phorestic force is minimized. Foss et al. (1989) investigated the collection of uncharged prolate spheroidal aerosol particles by 30 μm radius collector droplets. They found that such particles can be captured on the downstream side of the collector in

the absence of attractive forces in contrast to the case of spherical particles. In the case of prolate spheroidal aerosol particles collected by charged 30 μm radius droplets, the collision efficiencies for particles having large aspect ratios are significantly lower than those for spherical particles when the Coulomb force is dominant. These studies indicate that deviations from particle sphericity rather decrease collision efficiencies for the experimental conditions of our study and cannot account for the discrepancy between measured and calculated collision efficiencies. The largest uncertainties are associated with the theoretical description of phoretic processes at low temperatures. It might be necessary to re-assess these to obtain expressions that are in better agreement with experiments.

3.7.2 Implications for contact freezing

The efficiency of contact freezing depends on the efficiency of the collision process and the ability of the particle to act as INP. The most important heterogeneous ice nuclei identified in the atmosphere so far are mineral dusts. Size distributions of mineral dusts depend on the age of the air mass because larger particles are removed by gravitational settling. Mineral dust particles cover a large size range from 0.1 to 100 μm (Tegen and Schepanski, 2009; Maring et al., 2003). In the coupled aerosol-climate model ECHAM5-HAM, which was used to investigate heterogeneous contact and immersion freezing, the mineral dust aerosol is represented by two lognormal modes with mass-median radii of 0.37 and 1.75 μm (Lohmann and Diehl, 2006; Hoose et al., 2008). Small particles collide with droplets mainly due to Brownian diffusion, large ones due to impaction. The predicted number of collisions varies by up to a factor of three for Brownian diffusion and impaction depending on the mathematical formulation that one chooses. Most importantly, in the highly relevant size range for ice nucleation on mineral dusts from 0.5 - 2 μm, calculated collision efficiencies are strongly reduced when a critical Stokes number is included in the formulation for impaction. In updrafts within clouds a slight supersaturation typically persists, directing particles away from droplets due to thermophoresis which is only partly compensated by attraction due to diffusiophoresis. In downdrafts or when dry air is entrained in clouds, droplet evaporation mostly occurs at cloud top and close to the edges of cumuli, which is the region where first ice in clouds is indeed observed (Young, 1974). Under such conditions, thermophoresis leads to attraction and may contribute significantly to the collision efficiency in the size range 0.1 - 2 μm. The two formulations for thermophoresis are very different in terms of particle size and temperature dependence. This term has to be re-assessed to improve estimates of contact nucleation in models. In addition electric forces act on the particles which may significantly contribute to the overall collision efficiency. Evaporating cloud droplets and aerosol particles released from evaporated droplets from the same region of the cloud are supposed to have like charges (Tinsley and Leddon, 2013). For particles of sizes that act as INP such as mineral dusts, the predominant effect of their charge, irrespective of sign, is an increase in the collision rate due to the short-range electrical image-charge attraction (Tinsley and Leddon, 2013). Layer clouds such as stratocumulus and altostratus are weakly electrified producing droplet charges in the consequent gradients of electric field of the order of 100 e on 20 μm diameter cloud droplets (Zhou et al., 2009). Thunderstorm clouds are strongly electrified (Tinsley and Leddon, 2013) with cloud droplets bearing elementary charges in

the range of 10000 - 100000 e. Taking the effect of image charges into account will therefore increase the collision rate of particles with droplets even more. In summary, the collision efficiency of mineral dust particles with cloud droplets is most probably underpredicted in state of the art aerosol-climate models leading to an underestimation of the relevance of contact nucleation especially in evaporating clouds.

3.7.3 Implications for atmospheric aerosol scavenging

Impaction scavenging of aerosol particles can occur in cloud and below cloud. Below-cloud scavenging leads to the removal of aerosol particles from the atmosphere between cloud base and ground due to precipitation. In addition to impaction scavenging, in-cloud scavenging includes also contributions from nucleation scavenging (Seinfeld and Pandis, 2006). Aerosol scavenging is usually described by the scavenging coefficient (s^{-1}) defined as the rate of aerosol removal (Chate et al., 2011). In field measurements, the scavenging coefficient is usually calculated from measurements of the change in aerosol size distribution with rainfall (Santachiara et al., 2012). For very small and very large particles, there is mainly an agreement with theoretical studies. However, theoretical parameterizations often underestimate observed scavenging coefficients by one to two orders of magnitude for particles in the 0.2 μm - 2 μm diameter range, where collection efficiencies are lowest. Theoretical models predict Brownian diffusion as the dominating scavenging process of particles with diameters $<$ 0.2 μm, and inertial impaction as the main scavenging process for diameters $>$ 2 μm. For aerosol scavenging in the particle diameter range of 0.2 μm - 2 μm, contributions from electric and phoretic forces are thought to be important. In the case of thermal equilibrium between the drop and the environment and water vapor evaporation or condensation is the only factor determining the temperature gradient, thermophoresis and diffusiophoresis are supposed to act in opposite directions. However, in rain events, falling raindrops can have a different temperature from that of the ambient air and diffusiophoretic and thermophoretic forces will reinforce each other (Santachiara et al., 2012). Many theoretical studies on scavenging do not take phoretic forces into account, but even those which do are not able to explain the discrepancies between field and observed scavenging coefficients in the Greenfield gap (Santachiara et al., 2012). Most model parameterizations treat the collision processes separately and either assume that they act in series (Davenport and Peters, 1978) or calculate the total collision efficiency as the sum of individual collision efficiencies (Bae et al., 2009; Andronache et al., 2006). With this approach, the net effect of repulsive and attractive contributions of forces acting on particles cannot be taken into account correctly. Figures 3.5 and 3.6 show that the collision efficiency formulations of thermophoresis of W78 and A06 are vastly different. They are derived for large and small particles, respectively, but in most studies applied to the whole simulated particle size range. Moreover, the temperature dependency of the formulations by A06 and W78 are very different indicating also here large uncertainties. From this, it can be concluded that phoretic forces give important contributions to scavenging of aerosol particles in the accumulation mode, and are most probably also a main source of uncertainties in aerosol scavenging predictions.

3.8 Summary and conclusions

This study uses contact freezing experiments of freely falling 80 μm diameter droplets exposed to an aerosol consisting of silver iodide particles. The chamber is kept at ice saturation in the temperature range from 236 - 261 K leading to slow evaporation of water droplets giving rise to thermophoresis and diffusiophoresis. Droplets and particles bear charges inducing electrophoresis. From the experimental results, collision efficiencies of 0.13 and 0.07 were derived for 200 nm and 400 nm diameter particles, respectively. In addition, an upper and lower bound for 800 nm kaolinite particles of 0.047 - 0.11 was derived. These values are compared with theoretical formulations which yield values from 0.01 - 0.02. Brownian diffusion, electrophoresis and thermophoresis contribute the most to these values. Most experimental parameters are well constrained or show little sensitivity with respect to the resulting collision efficencies and can therefore not account for the observed discrepancies. Comparisons of different theoretical formulations show differences within one order of magnitude in the accumulation mode. There are large differences between the formulations for thermophoresis from A06 and W78 regarding size and temperature dependence. For our experimental conditions, diffusiophoresis results in a repulsive force and does not contribute to the total collision efficiency. It can be expected that in a combined treatment of the forces acting on particles, the calculated total collision efficiency would even be lower. Collision efficiencies are important parameters needed to correctly represent contact freezing and aerosol scavenging in models. Thermophoresis and diffusiophoresis are supposed to give important contributions to scavenging of aerosol particles in the accumulation mode, but are most probably also main sources of uncertainties in aerosol scavenging predictions. For ice nucleation in contact mode an accurate description of collision efficiencies below 273 K are needed. Ice nucleating particles are most probably in the accumulation mode size range. For this size range collection efficiencies are lowest and associated with the largest uncertainties. More experimental data of collision efficiencies especially at low temperatures are needed to validate theoretical formulations. This is to the authors knowledge the first dataset of collision efficiencies acquired below 273 K. More such experiments with different particle diameters are needed to improve the understanding of collision efficiencies.

Table 3.1: *Dependency of collision efficiency on droplet diameter, particle density and atmopheric pressure*

Parameter	Particle diameter (nm)		
	200	400	800
Droplet diameter (μm)			
77	0.0158	0.0082	0.008
80	0.0134	0.007	0.0074
83	0.0115	0.0061	0.0069
Density of particle (kgm^{-3})			
2100	0.0134	0.007	0.0074
5600	0.0134	0.007	0.0074
Atmopheric pressure (hPa)			
960	0.0134	0.007	0.0074
1000	0.0135	0.007	0.0074

Chapter 4

Comparing contact and immersion freezing from continuous flow diffusion chambers

This chapter is accepted for publication in Atmopheric Chemistry and Physics. Citation: Nagare, B., Marcolli, C., Welti, A., Stetzer, O., and Lohmann, U.: Comparing contact and immersion freezing from continuous flow diffusion chambers, Atmos. Chem. Phys. 2016

4.1 Introduction

Aerosol particles influence the climate system in different ways. They scatter or absorb the incoming solar radiation or can absorb thermal radiation. Aerosol particles also play a role in cloud formation by acting as cloud condensation nuclei (CCN) and as ice nucleating particles (INPs). INPs help in ice nucleation depending on their physical and chemical properties, temperature of the environment and presence of supercooled droplets. Heterogeneous ice formation may take place with the help of INPs between 237 K and 273 K in the mixed-phase clouds regime. In this regime, three pathways of ice nucleation are differentiated, namely, immersion freezing, condensation freezing and contact freezing. In condensation freezing, water vapor condenses on the INP at temperatures $<$ 273 K to form a liquid droplet which freezes instantaneously. Immersion freezing (IF) takes place when an INP acts as CCN and the formed droplet freezes when the temperature is lowered. In contact freezing the INP collides with the droplet followed by freezing. Contact freezing (CF) in the original sense is defined as the process in which freezing of a supercooled droplet results from the collision with an aerosol particle (Ladino Moreno et al., 2013; Vali, 1985). This view of collisional contact freezing has been complemented by Durant and Shaw (2005) who found higher ice nucleation temperature compared with the immersion mode, when an INP was in contact with the water-air interface of a droplet, from either the inside or the outside (Durant and Shaw, 2005; Gurganus et al., 2014; Fornea et al., 2009; Murray et al., 2012; Shaw et al., 2005). In the following, we refer to a contact nucleation process as adhesion freezing when the position of the INP on the water surface enhances the ice nucleation efficiency compared with immersion freezing and discriminate it from collisional contact freezing, which assumes an enhancement due to the collision of the particle with the droplet.

Various theoretical mechanisms underlying contact freezing have been proposed as explanations for the higher freezing efficiency in contact compared with immersion mode. They have been reviewed by Ladino Moreno et al. (2013). Here we discuss them in brief. Cooper (1974) proposed that ice embryos formed on INPs in vapor are able to nucleate supercooled water upon collision with a droplet. His explanation relies on the classical nucleation theory and is based on the prediction that the critical radius of an ice embryo for deposition nucleation is about 4-5 times larger than that for immersion freezing. Therefore a particle inactive as a deposition nucleus in the vapor, may nevertheless possess ice embryos larger than the critical size for an embryo immersed in water on itâs surface. Such an embryo may induce freezing when immersed in water. This mechanism was rejected by Fukuta (1975b). Fukuta (1975a) proposed a similar mechanism but with subtle differences. Similar to Cooper (1974), Fukuta (1975a) assumed that subcritical ice clusters form on the particles by vapor deposition. However, he rejected that these clusters remain active, once they are immersed in the droplet as proposed by Cooper (1974). Instead, he assumed that freezing occurs during the wetting process when the water front moves over the particle, because this process gives rise to a transient high free energy zone which facilitates nucleation. This process should be only valid for hydrophobic nuclei. While the older theories focus on a collisional contact freezing mechanism, the more recent ones concentrate on adhesion freezing. Indeed, experimental studies by Shaw et al. (2005) and Fornea et al. (2009) have shown that an INP that is not completely immersed in the droplet can trigger ice nucleation at higher temperatures. From simulations, Sear (2007) found that the nucleation rate is 4 orders of magnitude higher along the contact line where the water surface meets the surface of the particle. Based on classical nucleation theory, he considered this result as generic. Suzuki et al. (2007) found from their experiments with water droplets on silicon surfaces coated with various silanes that the temperature at which nucleation occurs at a contact line depends on the contact angle between water and the substrate. On the other hand, Gurganus et al. (2011, 2013) investigated the freezing of droplets deposited on clean and coated silicon wafers and did not observe any preference of nucleation at the contact line. The same group also studied this phenomenon on catalyst substrates with imposed surface structures and found that the preferred nucleation site was the contact line in the case of nanoscale texture but not for microscale texture (Gurganus et al., 2014). Djikaev and Ruckenstein (2008) proposed that the line tension associated with the three phase contact line may indeed play an important role. On the other hand, Niehaus and Cantrell (2015) investigated soluble INPs for contact freezing. They showed that ionic salts can trigger freezing of moderately supercooled water. They concluded that this freezing effect must depend on collision between water droplet and INP since the particles they have used dissolve when they become immersed in water.

Ladino Moreno et al. (2013) reviewed experimental studies on contact freezing and also pointed out large discrepancies in the available experimental data. Quantification of the number of INPs required for contact freezing, time dependence of contact freezing, dependence on particle type and size were listed amongst the most uncertain parameters. Hoffmann et al. (2013a,b), and Niehaus et al. (2014) attempted to quantify the number of INPs required to freeze a droplet by contact freezing for their respective experiments. In Hoffmann et al. (2013a,b), an highly electrified droplet is suspended in an electrodynamic balance. The freezing probability of a droplet on a single collision was shown to

be a steep function of temperature. Nine collisions were necessary to freeze the droplet at 244 K while a single collision was sufficient to freeze the droplet at 239 K for illite particles with a mobility diameter of 750 nm. They conclude that contact freezing is the dominant mechanism over immersion freezing (Hoffmann et al., 2013a). Niehaus et al. (2014) found that for mineral dust from different origins 10^3 to 10^5 particles had to collide with a droplet deposited on the glass slide in the temperature range of 253 K to 258 K. Moreover, they ran experiments in which they melted a droplet after having observed a freezing event. When they cooled it back to the original temperature, no freezing event occurred. From this, they concluded that contact freezing was more probable than immersion freezing and that the particle-droplet collision was responsible for freezing. Contact freezing and immersion freezing have been previously compared by Levin and Yankofsky (1983) for bacterial cells where onset temperatures for contact freezing were shown to be 2 K higher. However, they did not state how many particles were needed to collide with the droplets to initiate freezing. Also Ladino et al. (2011b) concluded that there are some hints that contact freezing is more efficient than immersion freezing for kaolinite particles. They attempted to derive the freezing efficiency per single particle using theoretical formulations of collision efficiencies to calculate the number of collisions between droplets and particles and obtained unrealistic freezing efficiencies on the order of 10 to 100 for 26 μm diameter droplets and 400 nm kaolinite particles. The too large values of the freezing efficiency were attributed to the overestimation of droplet size in calculating CE. They also were mistaking liquid droplets as frozen droplets because multiple droplets were simultaneously present in the laser beam of the detector (Ladino Moreno et al., 2013).

The relevance of contact freezing for the atmosphere depends on the collision rate and the freezing efficiency. The collision rate between particles and droplets is a function of the collision efficiency which is not well determined in the accumulation mode size range as pointed out by Nagare et al. (2015). Collision efficiency (CE) is defined as the fraction of particles in the cylindrical volume swept out by a falling droplet that collide with it. CE depends mainly on particle size and droplet size. Other factors which influence CE are relative humidity of the environment and charges on droplets and particles. For Aitken mode particles, Brownian motion of the particles is usually the dominant collision process and CE can exceed 1 because of the high mobility of the particles in this size range. For coarse mode particles, impaction and interception of particles are the dominant contributors to CE. The minimum of CE (Greenfield gap) is in the accumulation mode where thermophoresis and diffusiophoresis may also contribute to CE (Nagare et al., 2015).

In order to compare the efficiency of immersion freezing and contact freezing, we performed a series of experiments with silver iodide, kaolinite and Arizona Test Dust (ATD) in immersion and contact freezing mode. Silver iodide is known to be a very good ice nucleus (Vonnegut, 1949) inducing ice nucleation up to 269 K, while ATD and kaolinite become efficient ice nuclei only at lower temperatures. Silver iodide has been reported to be more efficient as INP in contact than in immersion mode (DeMott, 1995). Kaolinite and ATD have been widely tested in laboratory studies as immersion freezing nuclei. Kaolinite is a clay mineral and accounts for 13 % of dust mass in the atmosphere (Atkinson et al., 2013). It has been studied previously in immersion freezing (e.g., Welti et al., 2012)

and contact freezing studies (e.g., Ladino et al., 2011b; Svensson et al., 2009). ATD has been previously studied for immersion freezing by Marcolli et al. (2007) and Niedermeier et al. (2010) and for contact freezing by Niehaus et al. (2014). ATD is composed of quartz, feldspar, carbonate, illite, kaolinite and other clays (Broadley et al., 2012).

4.2 Experimental setups and procedures

4.2.1 Instrument description

CLINCH setup

Contact freezing data was obtained with the ETH CoLlision Ice Nucleation CHamber (CLINCH). This instrument has been used previously by Ladino et al. (2011b) for a contact freezing study with kaolinite as INPs. In CLINCH, aerosol and water droplets collide and may freeze by contact. The extension of the chamber length from 40 cm used by Ladino et al. (2011b) to 80 cm for the current study makes it possible to observe the frozen fraction of droplets (FF) i.e. the ratio of number of frozen droplets to total number of droplets, at residence times of 2 s and 4 s with 80 μm diameter droplets compared to 26 μm droplets used by Ladino et al. (2011b). The droplet diameter is changed from 26 to 80 μm in order to increase the geometrically swept out volume by the droplet and to avoid significant change in the droplet size due to evaporation in the chamber. 80 ± 3 μm diameter droplets are generated with a droplet generator (Ulmke et al., 2001) at the top center of the chamber with a frequency of 100 Hz. The droplets are generated with pure water (Milli-Q, 18.2 MΩ) at a temperature of 281 K. The relaxation time for a droplet to reach its terminal velocity (0.186 ms^{-1}) is 0.2 s and the time needed to reach the target temperature is about 0.1 and 0.6 s when the chamber is kept at 261 and 235 K, respectively (Nagare et al., 2015a). While performing the experiment, the walls of the chamber are coated with a thin layer of ice creating an ice saturated environment inside the chamber.

Aerosol particles enter the chamber at the top in air streams from both sides with a flow velocity of 1 LPM and can interact with the droplets inside the chamber. FF can be determined with the in-house developed Ice Optical DEtector (IODE) (Nicolet et al., 2010; Lüönd et al., 2010) which discriminates water droplets from ice crystals by measuring the depolarization of the backscattered light of a laser beam. In order to avoid the presence of several droplets simultaneously in the laser beam, a new laser was installed (402 nm, Schaefter + Kirchhoff laser Makroliniengenerator13LTM) providing a rectangular instead of a circular laser beam. At each temperature, a blank experiment without aerosol particles was performed before the aerosol stream was turned on. A more detailed description of the instrument and experiment is given in Nagare et al. (2015a).

IMCA/ZINC setup

Immersion freezing experiments were performed using the IMCA/ZINC setup (Welti et al., 2012). This setup combines the Zurich Ice Nucleation Chamber (ZINC) (Stetzer et al., 2008) with the vertical extension Immersion Mode Cooling chAmber (IMCA) (Lüönd et al., 2010). In brief, the aerosol particles are activated as CCN in the IMCA part at a relative humidity with respect to water $>$ 120 % and temperature $>$ 300 K. These activated droplets are then cooled down in the IMCA part and reach the target temperature for freezing when they enter the ZINC chamber. The droplets are 18 $-$ 20 μm in diameter when they leave the IMCA part and enter the water saturated environment in ZINC which is created by ice coatings on the parallel walls, which are kept at different temperatures. FF can be determined using the depolarization detector IODE at different residence times from 1 s to 21 s. A more detailed description of the instrument and experiment is given in Welti et al. (2012). Characteristics of the IMCA/ZINC and the CLINCH experiments are compared in Table 4.1.

4.2.2 Aerosol generation and sampling

Silver iodide was precipitated by mixing 0.1 M solutions of potassium iodide and silver nitrate. The aerosol particles were generated by atomizing this suspension and dried (for details refer to Nagare et al. (2015a)). The suspension was usually prepared the day before a measurement series was started and used for a measurement series performed during typically 2 days. Between measurements the suspension was kept in the dark. Kaolinite (Fluka, Sigma Aldrich GmbH) and ATD (Powder Technology Inc.) particles were aerosolised in a fluidized bed aerosol generator (TSI Model 43400A). The aerosol stream was passed through a cyclone to remove large particles. Aerosol particles were selected based on their electrical mobility with a Differential Mobility Analyzer (DMA TSI 3081) with an upstream impactor. These size selected particles were used for either contact or immersion freezing experiments in the respective experimental setups. The concentration of particles in CLINCH was measured at the end of the chamber using a condensation particle counter (CPC, TSI 3772).

4.2.3 Particle sprinkling experiment

We sprinkled polydispersed particles of AgI, ATD, and kaolinite gently on a water surface to observe optically whether they adhere to the surface or sink to the bottom. The particles were sprinkled on Milli-Q water at room temperature by gently shaking a spatula loaded with a small portion of the powders.

4.3 Experimental results

Figure 4.3 shows the FF observed for silver iodide as INP in CLINCH (triangles) as a function of chamber temperatures for droplet residence times of 2 s in panel (a) and 4 s in panel (b) for different

Table 4.1: *Instrument characteristics*

Instrument	Droplet diameter (μm)	Residence time of droplet (s)	Aerosol concentration cm^{-3}
IMCA/ZINC	18 - 20	3 (variable)	1 particle per droplet
CLINCH	80 ± 3	2 and 4	variable

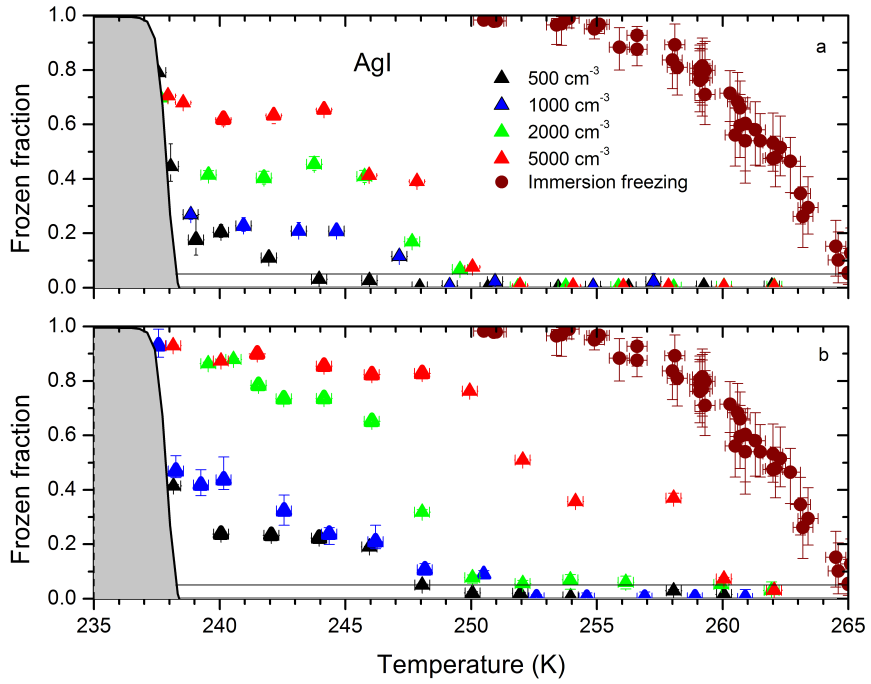

Figure 4.1: *Frozen fraction against chamber temperature for silver iodide particles of 200 nm diameter. Contact freezing for aerosol concentrations from 500* cm^{-3} *to 5000* cm^{-3} *are given by triangles for a droplet residence time of 2 s in panel (a) and 4 s in panel (b). Immersion freezing for 3 s residence time of droplets in the ZINC chamber is shown by circles. The gray shaded area shows the homogeneous freezing of droplets determined from blank experiments (without aerosol) and the black horizontal line indicates the reliability of measurement determined from the blank signal level observed in experiments without aerosol. Error bars shown represent the uncertainty in the frozen fraction due to the classification (liquid or ice) uncertainty of the IODE detector (Lüönd et al., 2010).*

concentrations of silver iodide. The gray shaded area is the experimentally determined homogeneous freezing regime of droplets in CLINCH from blank experiments. The black horizontal line marks the lower reliability limit of differentiation between ice and water determined from blank experiments. As the temperature of the chamber decreases to $<$ 250 K, the FF starts to rise and then remains constant. The frozen fraction due to immersion freezing from IMCA/ZINC experiments with 3 s residence time in the ZINC chamber is shown as circles for comparison with contact freezing. Silver iodide particles produced by our method are found to be much more efficient INP in terms of onset temperature in immersion than in contact freezing mode. The onset temperature for silver iodide particles as INP is 265 K while for contact freezing significant frozen fractions were observed only below 250 K except for the highest concentration and 4 s residence time. For the highest concentration used in our experiment, the onset temperature for contact freezing is 258 K.

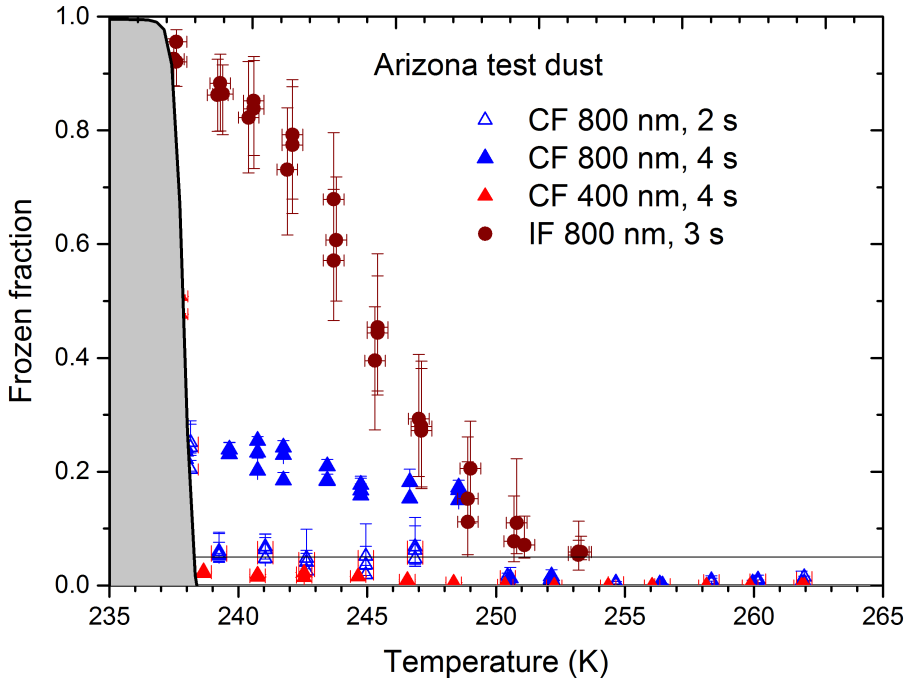

Figure 4.2: *Frozen fraction against chamber temperature for ATD particles of 400 nm and 800 nm diameter. Contact freezing (CF) for aerosol concentrations of 1000* cm^{-3} *are given by triangles for droplet residence times of 2 s and 4 s. Immersion freezing (IF from IMCA/ZINC) for 800 nm ATD particles and 3 s residence time in ZINC are shown by circles. The gray shaded area shows the homogeneous freezing of droplets determined from blank experiments (without aerosol) and the black horizontal line indicates the reliability of the measurement determined from the blank signal level observed in experiments without aerosol. Error bars represent the uncertainty in the frozen fraction due to the classification (liquid or ice) uncertainty of the IODE detector (Lüönd et al., 2010).*

Figure 4.3 shows the frozen fraction of droplets when ATD was used as INP in contact and immersion freezing mode. The frozen fraction due to immersion freezing shown are for 800 nm particles and 3 s residence time in the ZINC chamber. There is no significant difference in onset temperature for immersion and contact freezing for ATD. Figure 4.3 shows the frozen fraction for experiments performed with kaolinite. For this INP, the onset temperature of contact freezing is 3 K higher than for immersion freezing. Possible reasons for this will be discussed in Sects. 5.5 and 5.6.

4.4 Freezing efficiencies

4.4.1 Calculation of freezing efficiency from frozen fraction

The frozen fraction measured by CLINCH depends on the collision efficiency and the freezing efficiency. For a further evaluation and comparison of contact freezing and immersion freezing FF has to be converted to FE. If a droplet freezes after more than one particle have hit it, it is not clear which

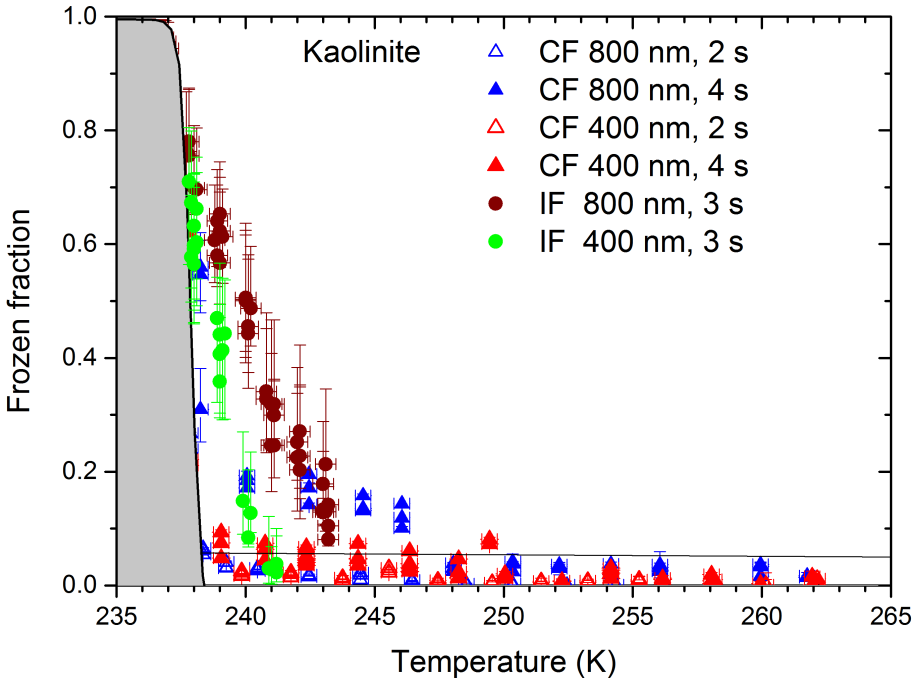

Figure 4.3: *Frozen fraction against chamber temperature for kaolinite particles of 400 nm and 800 nm diameter. Contact freezing (CF) for aerosol concentrations of 1000* cm^{-3} *are given by triangles for droplet residence times of 2 s and 4 s. Immersion freezing (IF from IMCA/ZINC) for 400 nm and 800 nm kaolinite particles and 3 s residence time in ZINC are shown by green and brown circles, respectively. The gray shaded area shows the homogeneous freezing of droplets determined from blank experiments (without aerosol) and the black horizontal line indicates the reliability of the measurement determined from the blank signal level observed in experiments without aerosol. Error bars represent the uncertainty in the frozen fraction due to the classification (liquid or ice) uncertainty of the IODE detector (Lüönd et al., 2010).*

particle induced freezing. Assuming that all collisions were needed for freezing leads to the following equation:

$$FE = \frac{FF}{N} \tag{4.1}$$

where N is the number of collisions for a droplet with the aerosol particles and can be calculated as (Ladino et al., 2011b)

$$N = CE \times C \times L \times \pi \times (R+r)^2 \tag{4.2}$$

where C is the concentration of the particles, R and r are the radii of droplets and particles, respectively, and L is the effective length experienced by the droplet given as

$$L = \frac{U(R)l}{U(R)+V_{flow}} \tag{4.3}$$

where l is the geometrical length traced by the droplet, $U(R)$ is the terminal velocity of the droplet and V_{flow} is the flow velocity of the carrier gas in CLINCH.

Eq. (4.1) assumes that the droplet has collected N particles and freezes due to the last particle that it has collected. However, the droplet can freeze on collision with the first particle and then collect other particles. Assuming that one collision is enough for ice nucleation, leads to the following expression for FE:

$$FE = \frac{FF}{1 - e^{-N}}. \tag{4.4}$$

Here the denominator indicates the fraction of unfrozen droplets after N collisions with the particles. We use this formula in the case of AgI, because we expect for this ice nucleus FE = 1 at T $<$ 245 K (Nagare et al. 2015). While Eq. (1) gives a lower limit of FE, Eq. (4) gives the upper limit.

Since FE is derived by normalizing FF with respect to N, FE should be independent of the residence time when the number of collisions is < 1. If freezing efficiencies of 2 s $(FE(2s))$ and 4 s residence times $(FE(4s))$ are the same within the experimental uncertainty, this can be considered as an indication of immediate freezing when the first particle collides with a droplet. Conversely, $FE(4s) > FE(2s)$ suggests that freezing is not immediate when a particle hits a droplet but that more time is needed on average. Such a time dependent freezing process would be in accordance with an immersion freezing mechanism assuming that the droplet only freezes when the particle becomes immersed. A time dependence is also expected for adhesion freezing when the particle adheres to the surface of the droplet. If $N < 1$, it is unlikely that FE is influenced by the number of collisions and we will interpret $FE(2s) = FE(4s)$ as a criterion for collisional contact freezing and $FE(4\text{s}) > FE(2\text{s})$ as a criterion for freezing in immersion mode or adhesion freezing.

4.4.2 Freezing efficiency of silver iodide particles

We derived a collision efficiency $CE = 0.13$ for 200 nm diameter AgI particles with 80 μm droplets in our previous study (Nagare et al., 2015a). This number is an order of magnitude higher than the values calculated with commonly used theoretical formulations of collision efficiencies. Figure 4.4 shows FE of 200 nm diameter silver iodide particles for droplet residence times of 2 s (open symbols) and 4 s (filled symbols) calculated using Eqs. (4.1) (panel a) and (4.4) (panel b). The number of collisions for the different particle concentrations range between 0.1 and 2.35 as listed in Table 4.4.2. Panel (a) of Fig. 4.4 shows that FE does not exceed 0.5 for $C = 5000$ cm^{-3} for 4 s residence time. For this concentration and residence time 2.35 collisions occurred in the chamber and freezing might have been induced by any of these collisions. Eq. (1) assumes that indeed all collisions are necessary to freeze a droplet and gives a lower limit of freezing efficiency. An upper limit is obtained using Eq. (4), which assumes that the first collision induces freezing. Panel (b) of Fig. 4.4 shows that this assumption leads to a grouping of FE data around 1 for T $<$ 245 K for all particle concentrations and residence times of 2 s and 4 s. This reinforces the assumption that the first contact leads to droplet freezing in this temperature range and confirms the plateau condition used in Nagare et al. (2015a) to derive CE. We ascribe data points with FE ¿ 1 to homogeneous

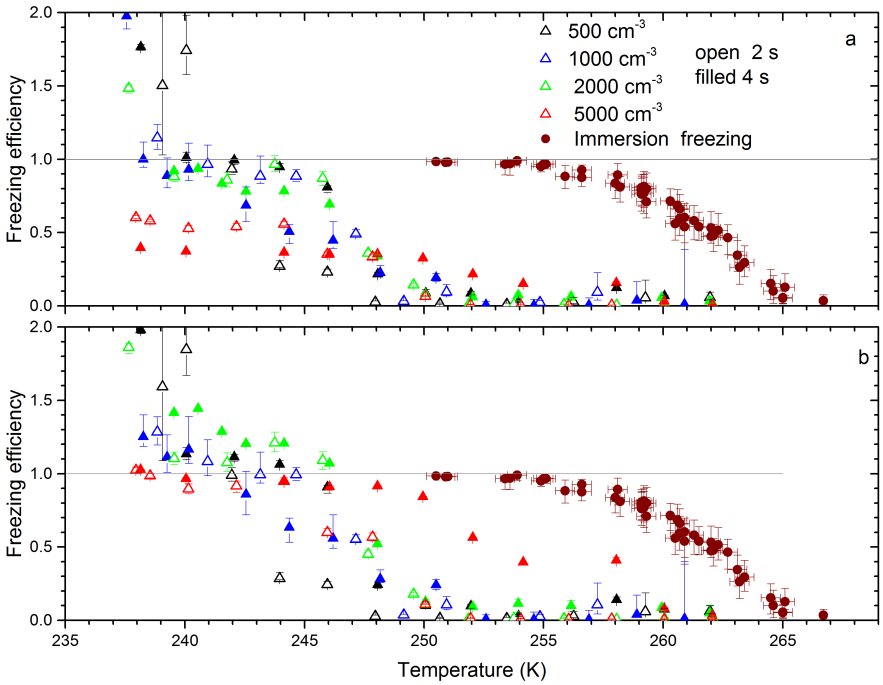

Figure 4.4: *Freezing efficiency FE against chamber temperature for contact freezing experiments (triangles) with 200 nm diameter AgI particles with droplet residence times of 2 s (open symbols) and 4 s (filled symbols). The concentration of silver iodide partiles varies from 500* cm^{-3} *to 5000* cm^{-3}*. A collision efficiency $CE = 0.13$ is used to calculate N. FE is calculated using Eq.* (4.1) *in panel (a) and Eq.* (4.4) *in panel (b). Immersion freezing of droplets in the ZINC chamber for 3 s residence time is shown as circles. The gray horizontal line indicates the maximum freezing efficiency realized when the first collision initiates freezing.*

Table 4.2: *Average number of collisions N for 200 nm silver iodide particles with a 80* μm *diameter droplet in concentrations from 500 to 5000* cm^{-3} *and residence times of 2 s and 4 s.*

Concentration cm^{-3}	2 s	4 s
500	0.11	0.23
1000	0.23	0.47
2000	0.47	0.94
5000	1.17	2.35

freezing and measurement uncertainties. For T ¿ 252 K, FE values significantly different from zero are only reached for concentrations of 5000 cm^{-3}. This would imply that above this temperature more than one collision is necessary for droplet freezing in CLINCH. For T $<$ 245 K, FEs for 2 s and 4 s residence times are the same within measurement uncertainties suggesting that ice nucleation occurs immediately when the particle hits the droplet. At higher temperatures the data points are quite scattered impeding a clear conclusion. Also shown are immersion freezing measurements with IMCA/ZINC with AgI particles that were prepared the same way as the ones for the contact freezing experiments. Residence time in the ZINC chamber was 3 s. Surprisingly, the onset temperature

and the efficiency for immersion freezing are significantly higher than for contact freezing. This observation is further discussed in Sect. 4.5.2.

4.4.3 Freezing efficiency of ATD particles

Figure 4.4.3 shows FE in contact freezing mode for 800 nm ATD particles calculated using Eq. (4.1). N is calculated based on 4 different assumptions for CE. For panel (a), $CE = 0.0033$ from the theoretical formulation by Park et al. (2005) and Wang et al. (1978) was used. Details of the calculations are given in Nagare et al. (2015a), where discrepancies between theoretical calculations and experimental observations have been addressed. For 200 nm silver iodide particles, the experimentally determined CE is 14 times higher than the calculated one. In order to adjust FE better to the theoretical upper limit of $FE = 1$ and due to lack of other available experimental values, the calculated collision efficiency was multiplied with the factor of 14 to calculate N for panel (b). For a lower limit the experimentally derived CE for 200 nm AgI particles $(CE = 0.13)$ was used to calculate N in panel (c). In panel (d), $CE = 0.061$ was used which shifts FE of 800 nm ATD particles close to 1, which is in accordance with the assumption that each collision leads to droplet freezing. The calculated CE shown in panel (a) leads to unrealistically high FE. This was also observed by Ladino et al. (2011b). Using a correction factor of 14 for CE, still yields FE values > 1. Panels (c) and (d) give best estimates of lower and upper limits of freezing efficiency. The difference in FE between panels (c) and (d) must be considered as an uncertainty due to the lack of reliable theoretical values of CE in the investigated temperature and particle size range. The number of collisions for the different assumptions of CE is listed in Table 4.3. For the lower limit case with $CE = 0.13$, FE reaches values up to 0.5 for data points that can be unambiguously assigned to heterogeneous freezing. Contact freezing experiments do not show significantly different onset temperatures compared with immersion freezing experiments carried out with the IMCA/ZINC setup, where every droplet contains one particle. The active site parameterization developed by Marcolli et al. (2007) based on DSC experiments is shown as brown line in Fig. 4.4.3. It agrees well with the immersion freezing experiments carried out with 800 nm particles in the IMCA/ZINC chamber. Taking $CE = 0.061$ (panel d), contact freezing might be slightly more efficient than immersion freezing. Taking $CE = 0.13$ (panel c), contact freezing and immersion freezing seem to be similarly efficient. We did not convert the frozen fraction of 400 nm ATD particles to freezing efficiency because FF is close to the detection limit. For all assumed values of collision efficiencies, the freezing efficiency at 4 s residence time is almost twice the value at 2 s residence time. As listed in Table 4.3 the number of collisions is < 1 for both residence times. While the uncertainty associated with the measurements at 2 s is quite large, this data still seems significantly lower than the 4 s residence time freezing efficiencies. An increasing freezing efficiency with increasing residence time is expected for immersion freezing (Hoffmann et al., 2013b; Welti et al., 2012) and adhesion freezing. Therefore, it is likely that freezing occurs due to one of these mechanisms rather than collisional contact freezing.

Table 4.3: *Number of collisions for 800 nm particles with a 80 μm diameter droplet*

Collision efficiency *CE*	Number of collisions N	
	2 s	4 s
0.003	0.0057	0.0122
0.46	0.079	0.168
0.13	0.24	0.48

4.4.4 Freezing efficiency of kaolinite particles

Figure 4.4.4 shows freezing efficiency for 800 nm diameter kaolinte particles for 2 s (open triangles) and 4 s (filled triangles) residence times. The frozen fraction measured for 400 nm particles was not significant, therefore, we do not convert this data to freezing efficiency. Panels (a), (b) and (c) use three different assumptions to calculate N as explained in the previous section for ATD. For panel (a) the theoretical formulations were used, while panels (b) and (c) give the upper and lower limit of FE, respectively. Shown as brown circles in Fig. 4.4.4 are the immersion freezing results of 800 nm Fluka kaolinite particles for 3 s residence time in the ZINC chamber. Freezing efficiencies are in good agreement with the previously published α-pdf parameterization by Welti et al. (2012) derived from immersion freezing experiments performed with the same setup (brown line). In Wex et al. (2014) immersion freezing experiments with 700 nm kaolinite (Fluka) particles were performed with LACIS (shown as blue diamonds) and with a CFDC (shown as green diamonds). In the LACIS instrument, INPs are activated to droplets at $T = 257 - 260$ K while cooling to the targeted temperature. They are at the experimental temperature during 1.6 s while they evaporate. This lower residence time may explain the lower freezing efficiency observed in LACIS compared with IMCA/ZINC. Slightly higher freezing efficiencies than in LACIS but still lower than in IMCA/ZINC were observed for 700 nm Fluka kaolinite particles in the CFDC (orange stars: Tobo et al. (2012); green diamonds: (Wex et al., 2014)). The contact freezing efficiencies from CLINCH are clearly higher for the lower limit of $CE = 0.046$ and slightly higher for the upper limit of $CE = 0.13$.

4.5 Discussion

4.5.1 Collision efficiency

Collision efficiency is a crucial parameter for an accurate comparison of contact and immersion freezing. Figures 4.4.3 and 4.4.4 show that freezing efficiencies of ATD and kaolinite particles calculated with theoretical formulations of CE are at least by one order of magnitude too high. This corroborates the finding by Nagare et al. (2015a), that CE formulations need to be reassessed for temperature below 273 K. More such studies for different particle and droplet sizes are needed to improve the data base for validation of calculated collision efficiencies at subzero temperatures, subsaturation with respect to water and droplets and particles with known charges. For measurements with the AgI aerosol, $FE = 1$ could be assumed for data points at T $<$ 245 K, because they showed constant frozen frac-

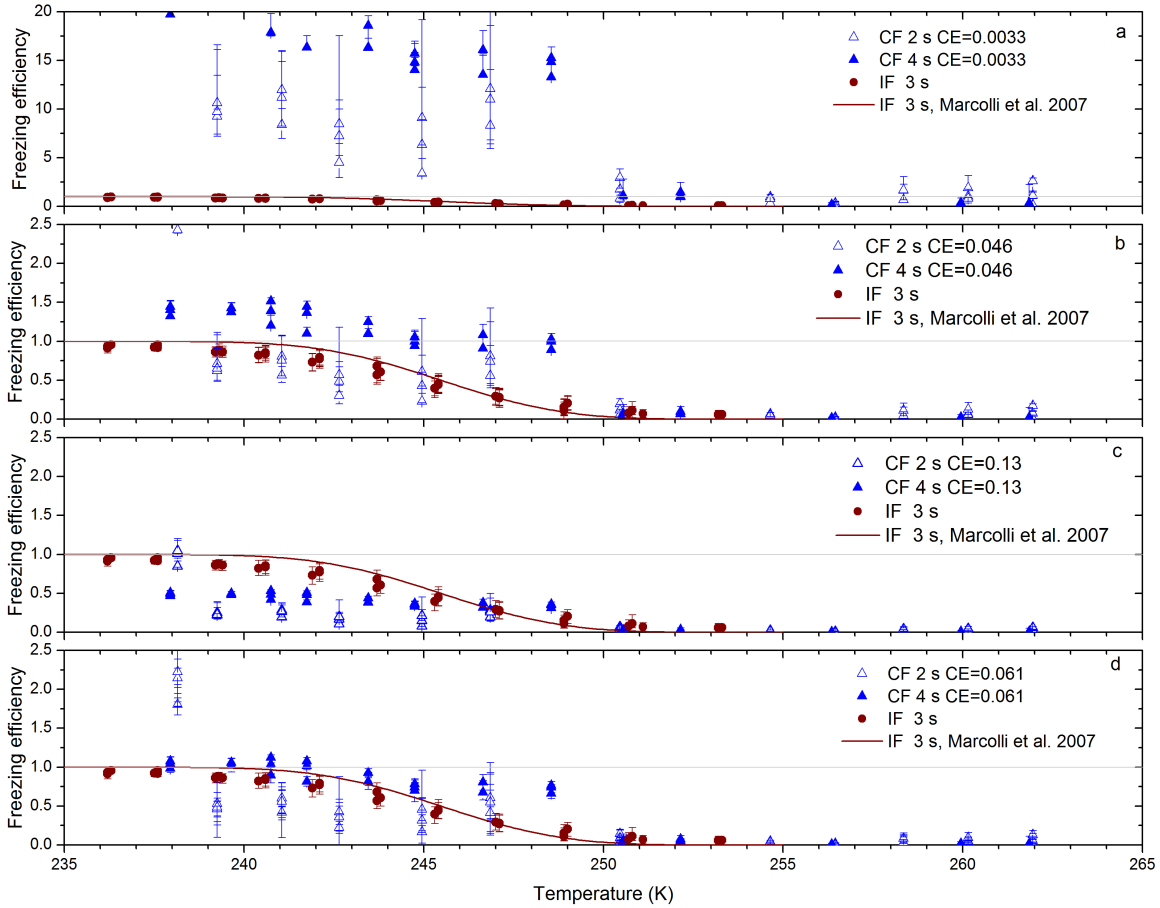

Figure 4.5: *Freezing efficiency for 800 nm ATD particles with a concentration of 1000* cm^{-3} *calculated with 4 different assumptions for CE: panel (a) with theoretical CE from Wang et al. (1978) and Park et al. (2005); panel (b) with* $14 \times CE$ *from panel (a) (see text for details); panel (c) with* $CE = 0.13$ *(applying the value for 200 nm AgI particles) for all particle sizes; panel (d) with* $CE = 0.061$*, shifting collision efficiencies close to 1. Filled triangles show contact freezing for 4 s residence time in the CLINCH chamber, the open triangles for 2 s residence time. Each triangle represents an independent measurement. Error bars represent the precision of the IODE detector. Brown circles show the freezing efficiency for immersion freezing of droplets in the IMCA/ZINC chamber for 3 s residence time. The brown lines show the* FF *calculated with the active site immersion freezing parameterization from Marcolli et al. (2007) evaluated for 800 nm particles and 3 s residence time. The gray horizontal line indicates* $FE = 1$*. Note that the y-scale in panel (a) is different from the ones in panels (b), (c) and (d).*

tions and IMCA/ZINC experiments determined $FE = 1$ at T $<$ 245 K. For ATD and kaolinite, there was no temperature range where freezing occurred with an efficiency of one. Therefore, only upper and lower limits of collision efficiency can be estimated. This limits the comparison of contact with immersion freezing. Collision efficiency is also a crucial factor to quantify the lifetime of the accumulation mode aerosol in the atmosphere because their lifetime strongly depends on the scavenging rate of particles by the droplets (Seinfeld and Pandis, 2006).

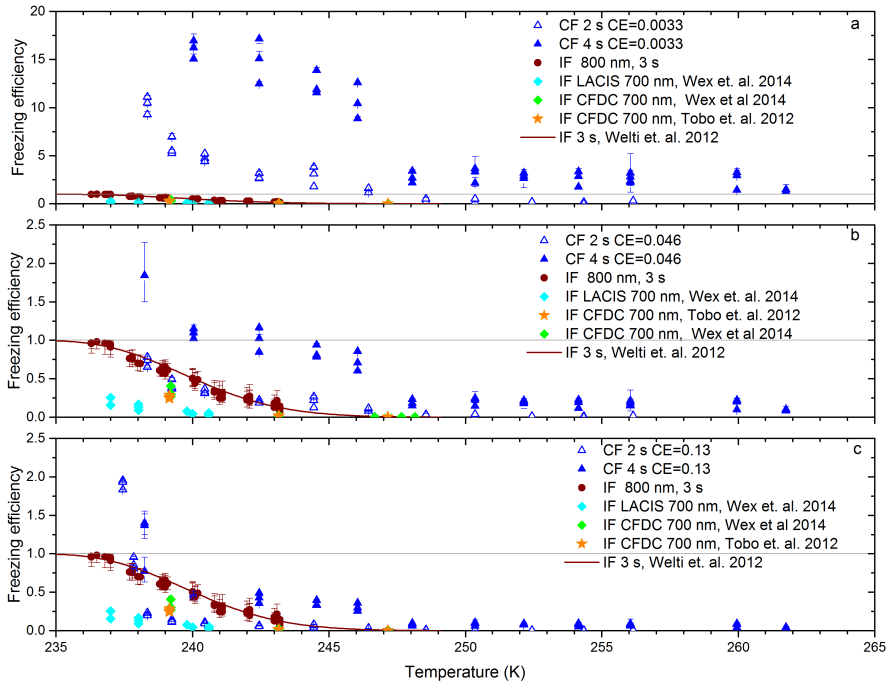

Figure 4.6: *Freezing efficiency for 800 nm kaolinite particles with a concentration of 1000* cm^{-3} *calculated with 3 different assumptions for CE: panel (a) with the theoretical CE from Park et al. (2005) and Wang et al. (1978); panel (b):* $14 \times CE$ *from panel (a); panel (c) with* $CE = 0.13$ *(applying value of 200 nm AgI particles) for lower bound of freezing efficiency. Each triangle represents an independent measurement. Error bars represent the precision of the IODE detector. Brown circles show the freezing efficiency of droplets in ZINC for a residence time of 3 s for 800 nm kaolinite particles. Orange stars show immersion freezing of droplets activated by 700 nm Fluka kaolinite particles (from Fig. 2a of Tobo et al. 2012). Light blue diamonds show immersion freezing of droplets activated by a 700 nm Fluka kaolinite particle (LACIS data with 1.6 s residence time (from Fig. 2 (right panel) of Wex et al., 2014). Green diamond shows immersion freezing of droplets activated by 700 nm kaolinite particle (CFDC data with 5 s residence time (from Fig. 2 (right panel) of Wex et al., 2014). The brown line represents the* α*-pdf parameterization from Welti et al. (2012). The gray horizontal line indicates the maximum freezing efficiency. Note that the y-scale for panel (a) is different from the ones shown in panels (b) and (c).*

4.5.2 Contact freezing process

The higher FEs for 4 s than for 2 s residence time of the CLINCH experiments with ATD and kaolinite are in agreement with adhesion freezing or immersion freezing. This indicates that collision itself does not increase FE but there seems to be an effect whether the INP adheres to the water surface or is immersed in the droplet. The situation is less clear for AgI. For contact freezing experiments FE at 2 s is the same as for 4 s residence time within error when on average one AgI particle or less collides with the droplet in the chamber. This result is in agreement with a collisional contact freezing mechanism, but may also result from a very high nucleation rate of immersion freezing and/or adhesion freezing at the investigated temperature.

When a particle adheres to the surface it might induce ice nucleation in contact mode by the part exposed to air and immersion freezing by the part immersed in water. When an insoluble or slightly soluble particle acts as cloud condensation nucleus (CCN), it is usually assumed that it becomes totally immersed into the droplet. However, whether the particle adheres to the droplet surface or becomes totally immersed depends on the wetting behavior of the particle (see Appendix A). The consequences for ice nucleation is discussed below for the investigated INPs.

Silver iodide

For AgI particles, freezing efficiencies for 2 s and 4 s residence times are the same within experimental uncertainties, which is in accordance with immediate freezing after collision. However, adhesion freezing and immersion freezing cannot be excluded, if these processes occur at a high rate. Whether AgI adheres to the surface after collision or becomes totally immersed depends on the contact angle between water and the AgI surface. Billett et al. (1976) observed a dependence of the contact angle on the silver concentration in the solution. For silver iodide prepared in stoichiometric ratio, they determined $\alpha = 45^{\circ} - 50^{\circ}$ for the intermediate advancing angle. We observed that most of the AgI particles adhered to the surface when we sprinkled them gently on water. This is in accordance with observations by Gokhale and Goold (1968) and Gokhale and Lewinter (1971). We therefore assume that silver iodide particles remain on the droplet surface after collision in the CLINCH chamber. It is also likely that the AgI particles adhere to the droplet surface in the ZINC chamber after activation in the IMCA chamber. Therefore, in CLINCH and IMCA/ZINC experiments, the efficiency of adhesion freezing is probed and it could be expected that freezing efficiencies in both experiments are the same. However, the IMCA/ZINC freezing experiments performed with the same AgI aerosol and similar residence times shows a much higher freezing efficiency than the CLINCH experiments. This is in contrast to DeMott (1995), who reported higher freezing efficiencies in contact than in immersion mode for AgI-AgCl aerosols. However, AgI is a complex ice nucleus that appears in different polymorphic forms. Moreover, it partly dissolves in water. Depending on the production procedure, AgI is agglomerated with soluble salts. Moreover the freezing ability depends on the surface charge on AgI particles. A closer investigation of factors influencing the efficiency of AgI as an ice nucleus and reasons for the lower freezing efficiency in CLINCH compared with IMCA/ZINC are discussed in the companion paper by Marcolli et al. (2016).

Arizona test dust

The ice nucleation ability of ATD has been investigated by several groups using different setups. Niehaus et al. (2014) investigated contact freezing of deposited droplets on a glass slide, which were exposed to a flow of a polydisperse ATD aerosol (0.3 - 10 μm diameter particles). They determined that one in 1000 particles induced freezing at 253 K, and one in 100 000 at 258 K. These numbers are not directly comparable with this study, because the detection limit for frozen fractions of the IODE detector is ca. 0.05. In CLINCH we observed the onset of freezing at 247 K for 800 nm ATD par-

ticles. For 800 nm ATD particles, the freezing efficiencies in contact mode are within experimental uncertainties the same as freezing efficiencies in immersion mode measured with IMCA/ZINC at 3 s residence time. When the ATD parameterization for immersion freezing proposed by Marcolli et al. (2007) is applied to 800 nm particles with a nucleation time of 3 s, it is agreeing well with the experimental data from IMCA/ZINC. Niedermeier et al. (2010) investigated immersion freezing of ATD particles with LACIS. Experiments with ATD aerosols with diameters $<$ 560 nm yielded frozen fractions of 0.04 at 239 K and 0.1 at 236 K. The low residence time and the cutoff of particles $>$ 560 nm might be reasons for this lower freezing efficiency compared with IMCA/ZINC. When the active site parameterization by Marcolli et al. (2007) is applied to 400 nm particles, it gives too high active fractions compared to experiments. The heterogeneous mineralogical composition of ATD may be one of the reasons that smaller particles do not act as effective INPs and may even be inactive. Atkinson et al. (2013) have shown that ATD is composed of 20.3% K-feldspar, 12.4 % (Na, Ca)-feldspar, 17.1 % quartz, 7.5 % illite/muscovite, and 10 % illite/smectite. Clay mineral particles of illite/muscovite tend to be small and presumably dominate the particle fraction with diameters $<$ 500 nm, while quartz and K-feldspar may be overrepresented in the fraction with diameters $>$ 500 nm. Moreover, larger particles are often conglomerates of different minerals (Reid et al., 2003; Kandler et al., 2011) and might contain contributions of some K-feldspar while small particles are often primary particles of one mineral, which might not be very active as INP. Comparison of all measurements shows that immersion and contact freezing are similarly efficient modes of ice nucleation with ATD. Contact freezing experiments performed at 2 s residence time yielded higher freezing efficiencies than at 4 s, which is compatible with adhesion freezing or immersion freezing, but not with a collisional freezing mechanism. If particles became immediately immersed after contacting the droplet, freezing would occur in immersion mode also when a contact freezing experiment is performed. Indeed, the surfaces of many mineral dusts like quartz and feldspars are covered with hydroxyl groups, which render surfaces hydrophilic (Koretsky et al., 1997). Shang et al. (2010) measured contact angles of water droplets on clay films and found for illites a dependence of contact angles on relative humidity and on the exchangeable cations: the contact angle of Ca-illite sank from 28.3° to 21.6° when RH was raised from 19 % to 100 %. At 33 % RH contact angles ranged between $23.3° - 34.2°$ for illites saturated with different cations (Na, K, Mg, or Ca). Contact angles of $31° - 35°$ were measured for quartz (Szyszka, 2012). When we sprinkled ATD on a water surface, most particles immediately immersed and sank to the bottom. This suggests that when ATD particles collide with water droplets, the particles become immediately immersed such that in immersion freezing and contact freezing experiments the immersion mode is probed.

Kaolinite

X-ray powder diffraction showed that Fluka kaolinite (K-SA) which is used in this study, contains only 82.7 % kaolinite, but 5.4 % illite/muscovite, 5.9 % quartz, and 4.5 % K-feldspar (Atkinson et al., 2013). The clay minerals illite/muscovite and kaolinite tend to form small crystals and are presumably enriched in the particle fraction with diameters $<$ 500 nm, while quartz and K-feldspars might

be overrepresented in the fraction with diameters > 500 nm. K-feldspars and illite are known to be efficient ice nuclei (Atkinson et al., 2013; Hiranuma et al., 2015) and may dominate freezing when many particles are present in a sample (Pinti et al., 2012). When only one particle is present, this is likely to be a kaolinite particle. Kaolinite is a clay mineral with the formula $Al_2Si_2O_5(OH)_4$. It has a layered structure with octahedral aluminum and tetrahedral silicon layers. It forms plate-like crystals with sizes of several hundred nanometers to micrometers and typical thicknesses of 30 - 50 nm (Hu and Michaelides, 2007, 2008). These plates have a hydrophilic octahedral Al-OH surface and a rather hydrophobic tetrahedral siloxane (Si-O) surface. The edges of the plates are terminated by oxygen atoms or hydroxyl groups and are hydrophilic. Šolc et al. (2011) computed a contact angle of 105° for nanodroplets on the tetrahedral siloxane surface by force-field molecular dynamics. Nanodroplets spread on the octahedral surface indicating a contact angle of 0°. Shang et al. (2010) measured a contact angle of about 18° for water droplets on kaolinite films. This experimental value represents an averaged value over all kaolinite surfaces. The energetically most favorable configuration is therefore when the kaolinite particle adheres to the water surface with the siloxane surface exposed to air. Whether a kaolinite particle realizes this configuration may depend on the orientation of the particle when it contacts the water droplet. When we sprinkled kaolinite powder on water, we observed that some particles floated on the surface for hours while others became totally immersed and sank to the bottom within seconds. The lower freezing efficiency observed for 2 s residence time in the CLINCH chamber compared with 4 s is incompatible with a collisional freezing process but in accordance with adhesion freezing or immersion freezing. A particle on the surface can induce ice nucleation in the immersion mode with the part immersed in water or in contact mode with the part exposed to air. While it is likely that a kaolinite particle that hits a water droplet adheres to the surface and exposes the hydrophobic siloxane surface to air, it is less clear whether particles that underwent droplet activation stick to the surface or whether they totally immerse into the growing droplet. Which is the case may also depend on the conditions during activation like supersaturation or growth rate of the droplet. The immersion and contact freezing studies compiled in Fig. 4.4.4 suggest that contact freezing is more efficient than immersion freezing with an onset temperature that is about 3 K higher. Ladino et al. (2011b) who compared their contact freezing data with immersion freezing measurements from Lüönd et al. (2010) using IMCA/ZINC concluded that there are some hints for contact freezing to be more efficient than immersion freezing. Pitter and Pruppacher (1973) compared contact and immersion mode freezing temperatures in wind tunnel experiments by exposing water droplets to kaolinite particles that were injected into the air stream. They estimated that a droplet captured several thousands of particles, which explains the much higher median freezing temperature of 261 K compared with this study. In accordance with our experiments, they found a clear shift to lower freezing temperatures when changing from contact to immersion mode experiments. Hoffmann et al. (2013b) found that contact freezing dominates over immersion freezing for droplets levitated in an electrodynamic balance that were exposed to a flow of a kaolinite KGa-1b particles. Svensson et al. (2009) investigated contact freezing using an eletrodynamic balance to levitate droplets exposed to a flow of Fluka kaolinite particles. They observed contact freezing below 249 K for dry conditions and

a freezing threshold of 267 K when the air was humidified. This value is higher than the one reported for freezing of bulk suspensions of Fluka kaolinite (K-SA) by Pinti et al. (2012).

It is not clear which surface of kaolinite is responsible for ice nucleation. Using grand canonical Monte Carlo simulations, Croteau et al. (2008, 2010) showed that the Si-O surface remained dry up to water vapor saturation, while the edges and the Al-OH surface are much more hydrophilic and absorb up to a monolayer water at water saturation. Adsorbed water on the octahedral Al-OH surface exhibits hexagonal patterns but no close lattice match with ice (Croteau et al., 2008, 2010). Simulations by Zielke et al. (0) showed that for the Al-surface, reorientation of the surface hydroxyl groups is essential for ice nucleation. On the siloxane surface, ice nucleates via an ordered arrangement of hexagonal and cubic ice layers, joined at their basal planes where the interfacial energy cost is low. Experimentally, much higher absorption was determined showing that most absorption probably occurs on surface irregularities such as adsorbed ions or surface defects like trenches, pits, and steps (Schuttlefield et al., 2007; Tabrizy et al., 2011). Croteau et al. (2010) have shown that absorption is much higher on trenches than on the defect-free surface. Ice nucleation may therefore occur on liquid patches on an otherwise dry surface (Conrad et al., 2005). The wetting state of a nucleus may therefore be a crucial parameter for ice nucleation by kaolinite. This would be in accordance with the higher nucleation temperatures observed by Svensson et al. (2009) at humid conditions and point to a adhesion freezing mechanism.

4.6 Summary and conclusions

This study confirms the findings of Nagare et al. (2015a) that theoretical formulations give too low collision efficiencies at subzero temperature for particles in the accumulation mode. In CLINCH, droplets are evaporating giving rise to diffusiophoresis and thermophoresis. Moreover, droplets and particles are charged. Freezing efficiencies calculated from theoretical formulations of collision efficiencies are more than one order of magnitude higher than the highest possible value of $FE = 1$. An assessment of the relevance of contact compared to immersion freezing is therefore limited by knowledge of collision efficiencies. To improve calculated collision efficiencies, formulations of thermophoresis and diffusiophoresis should be re-assessed.

Comparing contact freezing efficiencies acquired at 2 s ($FE(2s)$) and 4 s ($FE(4s)$) residence times enables conclusions regarding the freezing mechanism. For contact freezing experiments with AgI, freezing efficiencies at 2 s and 4 s residence times were the same within error when the droplets collected on average only one particle during their time in the chamber. This is in accordance with a collisional contact freezing mechanism. However, adhesion freezing and immersion freezing cannot be excluded if these processes occur at a high rate. For experiments with ATD and kaolinite $FE(2s)$ was smaller than $FE(4s)$ which is incompatible with immediate freezing after contact. Therefore, immersion freezing or adhesion freezing must be at work for these INPs. The comparison of contact and immersion freezing experiments did not confirm a general enhancement of freezing efficiency in contact mode relative to immersion mode. One reason for this may be that in CLINCH and

IMCA/ZINC experiments the particles are free to realize the energetically most favorable position in or on the droplet. For AgI particles the freezing efficiency in CLINCH experiments was less than in IMCA/ZINC and the onset temperature was shifted to lower values. This is further investigated in Marcolli et al. (2016). For ATD, freezing efficiencies in contact and immersion mode were similar. For kaolinite particles, contact freezing became detectable at higher temperature than immersion freezing. A specific dependence on the INP for the enhancement of contact freezing relative to immersion freezing is in accordance with Gurganus et al. (2014) who observed an increased efficiency for nucleation at the three-phase contact line in case of nanoscale but not for microscale textures. In most experiments of contact freezing inside-out, the position of the particle with respect to the droplet is fixed by the design of the experiment (Shaw et al., 2005; Fornea et al., 2009; Gurganus et al., 2014). Whether a particle adheres to the surface or becomes totally immersed in a droplet depends on the wetting of the particle with water. A contact angle of zero corresponds with complete wetting, for higher values, the wetting is only partial. Our observations of particles that were gently sprinkled on water confirmed the predictions based on contact angles. Our experiments and calculation suggest that AgI particles partition to the droplet surface for contact and immersion freezing experiments. ATD particles seem to have highly hydrophilic surfaces that lead to fast immersion of the particles so that there is no time for adhesion freezing and immersion freezing prevails. Kaolinite forms plate-like crystals with a hydrophobic siloxane surface, all other surfaces are hydrophilic. It is therefore energetically most favorable when the hydrophobic surface of kaolinite particles is exposed to air. For this configuration, adhesion freezing and immersion freezing can compete.

4.7 Wetting of particles

The wetting behavior of particles can be quantified by the contact angle α, which is related to the surface tensions of water with air σ_{LA} and solid with air σ_{SA} and the interfacial tension between solid and water σ_{SL} through the Young equation (Holownia et al., 2008) as follows:

$$\cos\alpha = \frac{\sigma_{SA} - \sigma_{SL}}{\sigma_{LA}}, \tag{4.5}$$

The change in surface tension when the particle that adheres to a surface of the droplet becomes totally immersed in the droplet is given as (Holownia et al., 2008)

$$\Delta\sigma = \sigma_{SL} - \sigma_{SA} + \sigma_{LA} \tag{4.6}$$

Using Young's equation the change of surface tension is

$$\Delta\sigma = \sigma_{LA}(1 - \cos\alpha). \tag{4.7}$$

The change in the interfacial energy is given by

$$\Delta G = \Delta\sigma A \tag{4.8}$$

where A is the surface area of the particle exposed to air when the particle adheres to the surface of the droplet. Considering a cubic particle and neglecting the curvature of the droplet, the area to be immersed in the droplet would be the area of one face of the cube. The particle will immerse in the droplet for negative ΔG and will remain on the surface for positive ΔG. As can be seen from Eq. 4.8, ΔG is always positive and becomes zero for $\alpha = 0^\circ$. This means that in the absence of other forces, complete wetting of the particle surface by water is needed for total immersion of the particle into the droplet.

Chapter 5

Conclusions and Discussion

This thesis was dedicated to the investigation of contact freezing. After many years of research, clear experimental evidence is still missing whether contact freezing is indeed more efficient than immersion freezing (Ladino Moreno et al., 2013). One reason for this is the large uncertainty connected with the collision efficiency between cloud droplets and aerosol particles in the size range of the Greenfield gap. The first part of this laboratory study was focused on the quantification of the collision efficiency between cloud droplets and aerosols at mixed-phase cloud temperatures. We used the frozen fraction of droplets observed in contact freezing experiments with 200 and 400 nm particles as INPs for different concentrations of particles and different residence times of the droplets in the nucleation chamber to derive the collision efficiency based on the assumption that each collision of a particle with the droplet would cause freezing of the droplet. We also determined an upper and lower limit of the collision efficiency for 800 nm kaolinite particles. It is found that the collision efficiency at mixed phase cloud temperatures should be higher for accumulation mode particles than the analytical expressions used in various scavenging studies. It was noticed that the analytical expression of Wang et al. (1978) and Andronache et al. (2006) describing collision efficiency of thermophoresis and diffusiophoresis differ vastly. The temperature dependence of thermophoresis is discussed in detail in chapter 3. The importance of electrical charge on droplet and particles and the formation of image charges is also discussed. We conclude that the largest discrepancy is associated with the theoretical description of the phoretic processes at mixed phase cloud temperatures and we suggest that these expressions need a re-evaluation. This study was carried out with 80 μm diameter droplets and it is necessary to investigate other droplet sizes in order to generalize the findings of this study. The previously neglected important factor of electric charge (Ladino et al., 2011a) of droplets and particles was shown to be critical in order to estimate collision efficiency. More experiments with precise control of charge on droplets and particles would give new insights into collision efficiency.

The second part of this thesis was dedicated to investigate the relative importance of immersion freezing and contact freezing for silver iodide, kaolinite and Arizona test dust. We used frozen fractions in the immersion mode measured in the IMCA/ZINC chamber and compared them with frozen fractions from CLINCH. In order to convert frozen fraction of CLINCH to freezing efficiency per single particle, collision efficiencies determined in the first study were used for AgI aerosols. For kaolinite and ATD aerosols different assumptions were tested, leading to upper and lower limits of

freezing efficiencies. Major findings of this have been discussed in chapter 4. We measured the frozen fraction of droplets for two different residence times of droplets in CLINCH. We can observe that frozen fractions scale with the residence time for the same concentration of AgI particles and increase with the concentration of particles. Freezing efficiencies by contact and immersion freezing were compared for the continuous flow chambers CLINCH and IMCA/ZINC. In our study we found that our silver iodide particles are much less efficient in terms of onset temperature for contact freezing than for immersion freezing. 800 nm ATD particles in our experiment showed similar onset temperature for contact freezing as for immersion freezing although 800 nm kaolinite particles showed onset temperatures higher by 3 K for contact freezing. Observing the frozen fractions at different residence times of droplet in the chamber shows that for the kaolinite and ATD, freezing efficiency for 4 s residence time is higher than the 2 s. This is contrary to collisional contact freezing where freezing efficiency for different residence times is expected to be the same and hence for kaolinite and ATD immersion freezing and contact freezing inside-out must be at work. In case of silver iodide freezing efficiencies of the two residence times are the same within experimental error however we can not rule out contact freezing inside-out and immersion freezing.

5.1 Outlook and Comments

In the atmosphere, cloud droplets are activated from CCN. The droplets generated in this study were of Milli-Q water. To simulate cloud droplets impurities like ammonium sulphate and sodium chloride can be added to Milli-Q water.

The equilibrium thermodynamics calculation in chapter 4 suggests that the equilibrium position of the particle is at the surface of the droplet. In the case of the immersed particle, how this can affect the position of the particles inside the droplet needs to be investigated to understand the freezing mechanisms.

It is noticed that very little literature on charges on cloud droplets is available. More observations on charges of cloud droplets can help in constraining the collision efficiency due to electrophoresis. Various studies have proposed that image charge can play an important role for droplet-particle collisions. The requirement for image charge is the polarizability of the droplet and the particle. The current knowledge about polarizibilty is rather poor.

Appendix A

Charge measurement

As discussed in chapter 3, electrophoresis has a major role in the collision efficiency between droplets and particles if either of them are electrically charged. In our droplet generator, droplets get charged while they separate from the tip of the droplet generator. To measure the charge on the droplets, we passed a droplet stream through a capacitor consisting of two parallel plates which were connected to a DC voltage supply. A schematic of the charge measurement setup is shown in Fig. A.1. Positively charged droplets are attracted towards the negative plate while negatively charged droplets are attracted to the positive plate and uncharged droplets fall straight through the plates. The charge on the droplet is determined as follows. The force acting on the droplets can be written as

$$F = q \times E = q \times \frac{V}{d} = m \times a, \tag{A.1}$$

where F is the force on the droplets with charge q, V is the applied voltage, E is the electric field, d is the distance between the plates, m is the mass of the droplet and a is the acceleration of the droplet. From laws of kinetics,

$$x = U_x t + \frac{1}{2} a_x t^2 \tag{A.2}$$

where x is the distance traveled by the droplet in horizontal direction, U_x is the initial velocity of the droplet in x direction, t is the time before the droplets reach one of the plates and a_x is the acceleration of the droplets in horizontal direction.

At $t = 0$, $U_x = 0$ and $d = a_x t^2$, where d is the distance between the plates. Hence

$$t = \left(\frac{d}{a_x} \right)^{\frac{1}{2}} \tag{A.3}$$

Hence the vertical distance traveled by the droplet between the plates L is given as.

$$L = U_t \times t = U_t \left(\frac{d}{a_x} \right)^{\frac{1}{2}} \tag{A.4}$$

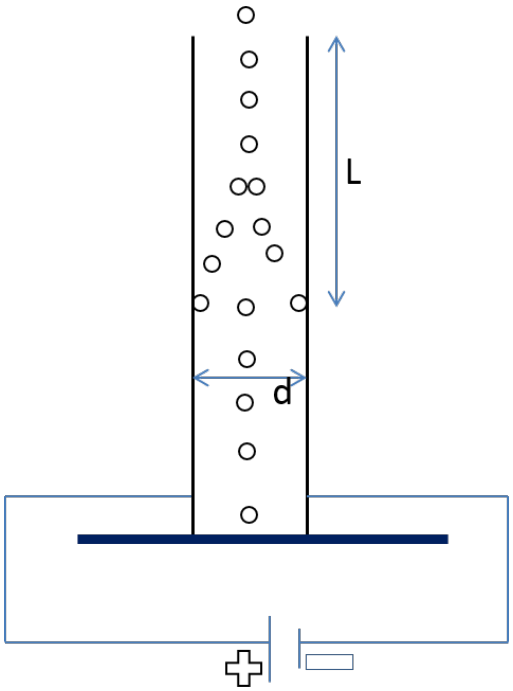

Figure A.1: *Schematic of measurement of charge on droplet.*

where U_t is the terminal velocity of the droplet. By substitution for a_x from Eq. (A.1),

$$L = U_t d \left(\frac{m}{qV} \right)^{\frac{1}{2}} \tag{A.5}$$

$$q = U_t^2 d^2 \frac{m}{VL^2}. \tag{A.6}$$

Eq. (A.6) gives the charge of the droplet.

Appendix B

Elemental composition of a silver iodide particle

Silver iodide was prepared by mixing of 0.1 M potassium iodide and 0.1 M silver nitrate solutions. The particles were produced by atomizing the solution. Details of aerosol preparation are discussed in chapter 3. To investigate the elemental composition of the produced aerosols, energy dispersive X ray spectroscopy (EDX) analysis on particles was performed. Figure B.1 shows the TEM-EDX image of AgI particle. The particle composition shows that it contains silver and iodine in the bright area. The second area shows that the particle also contains some potassium.

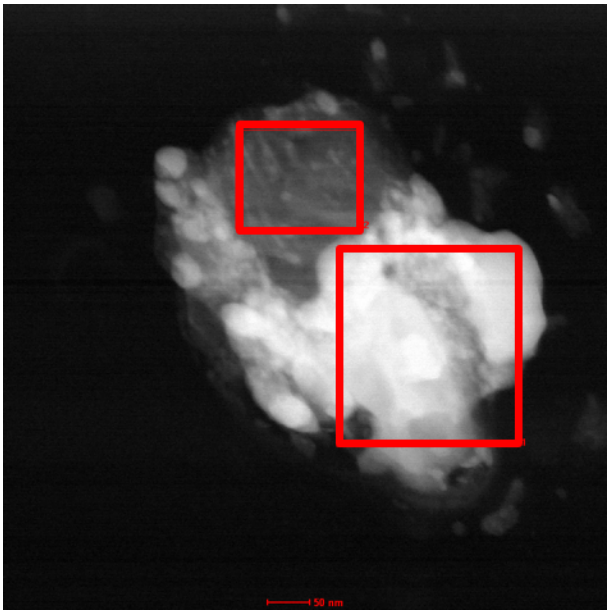

Figure B.1: *EDX image of the produced particle.*

List of symbols

Table B.1: *List of symbols*

A	surface area of the particle (m^2)
B_p	Mobility of particles (s kg^{-1})
C	Concentration of particle ([m^{-3})
C_c	Cunningham slip correction
C_{Df}	Force constant for ventilated diffusiophoresis (kg m^3 s^{-2})
C_{El}	Force constant for electrophoresis (kg m^3 s^{-2})
C_{Th}	Force constant for ventilated thermophoresis (kg m^3 s^{-2})
C_p	Specific heat capacity of air (1005 kJ kg^{-1} K)
D_{diff}	Diffusion coefficient of aerosol particles (m^2 s^{-1})
D_d	Diameter of the droplet (m)
D_v^*	modified diffusivity of water vapor
D_w	Diffusivity of water vapor (m^2 s^{-1})
d_p	Diameter of the particle (m)
E	Collision efficiency
E_{Tot}	Sum of all contributing mechanisms of collision efficiency
E_{Br}	Collision efficiency due to Brownian diffusion
E_{int}	Collision efficiency due to interception
E_{imp}	Collision efficiency due to impaction
E_{Th}	Collision efficiency due to thermophoresis
E_{Df}	Collision efficiency due to diffusiophoresis
E_{El}	Collision efficiency due to electrophoresis
ΔF	activation energy of molecule (Pa)
e_i	saturation vapor pressure over ice (Pa)
e_w	saturation vapor pressure over water (Pa)
FE	Freezing efficiency
FF	Frozen fraction of droplets
f_h	mean ventilation coefficient for heat transfer
f_p	mean ventilation coefficient for aerosol particle flux
f_v	mean ventilation coefficient for mass
ΔG	Gibbs free energy for phase change (J)
h	Planck constant (Js)
$I_\perp$ and $I_\parallel$	signal intensities in the perpendicular and parallel channel of IODE (pW)
L	effective length experienced by the droplet (m)
l	length of chamber (m)

k_a	Thermal conductivity of air (J $m^{-1}s^{-1}$ K^{-1})
k_B	Boltzmann constant (JK^{-1})
k_p	Thermal conductivity of particles (0.419 $Jm^{-1}s^{-1}K^{-1}$)
k_B	Boltzmann constant (kg m^2 s^2 K^{-1})
J_{hom}	homogeneous nucleation rate (m^3s^{-1})
J_{het}	heterogeneous nucleation rate (m^2s^{-1})
N_{ice}	number of ice crystals
N_{water}	number of water droplets
n_e	number of water molecules in an ice embryo
P_e	Peclet number
P_r	Prandtl number for air
p_s^0	Saturation vapor pressure at droplet surface (Pa)
p_a^0	Saturation vapor pressure of environment (Pa)
R	Diameter ratio between particle and droplet
R_e	Reynolds number
R_v	gas constant for water vapor $JK^{-1}mol^{-1}$
r	radius of an ice embryo (m)
r_c	critical rdaius of an ice embryo (m)
r_d	radius of water droplet (m)
Sc	Schmidt number of aerosol particles
Sc_w	Schmidt number for water vapor air
St	Stokes number (S83)
Stk	Stokes number (P05)
St^*	Critical stokes number
T	absolute temperature (K)
T_a	Air temperature (K)
T_c	Air temperature in Celsius
T_s	Temperature of droplet surface (K)
t	time (s)
U	Terminal velocity of droplets (m s^{-1})
u	Terminal velocity of particles (m s^{-1})
α	Packing density i.e. water volume present in unit volume of air
σ	Viscosity ratio of water to air
σ_{iw}	interfacial energy between ice and water (Jm^{-2})
σ_{LA}	surface tesnsion between air and liquid (Jm^{-2})
σ_{SL}	interfacial tension between particle and water (Jm^{-2})
δ	depolarization ratio
θ	contact angle (rad)
μ_a	Dynamic viscocity of air (kg m^{-1} s^{-1})
μ_a	Viscocity of water at 273 K (1.787×10^{-3} kg m^{-1} s^{-1})
μ_i	chemical potential of molecule in ice phase (J)
μ_w	chemical potential of molecule in liquid water (J)
ϕ	diffusive flux of molecules ($m^{-2}s^{-1}$)
ν_i	volume of water molecule in ice (m^3)
ρ_a	Density of air (1.293 kg m^{-3})
ρ_w	Density of water (1000 kg m^{-3})
ρ_p	Density of aerosol particles (kg m^{-3})
τ	Relaxation time (s)
λ_a	Mean free path of air molecules (m)

List of Figures

1.1 Radiative forcing and effective radiative forcing 3
1.2 Aerosol indirect effect 4
1.3 Change in gibbs free energy 6
1.4 Schematic representation of the different nucleation modes 8
1.5 Nucleation energy barrier for different contact angles 9
1.6 Collisional and inside-out contact freezing 11

2.1 Schematic of CLINCH 17
2.2 80 μm droplet as observed by the camera. 18
2.3 Size measurement of typical droplet images captured by the camera. 18
2.4 Homogeneous freezing of droplets in CLINCH 19
2.5 RH_w variation at 100 % RH_i 19
2.6 Size eveolution of droplets in CLINCH 21
2.7 Schematic of collision efficiency 21
2.8 Schematic of collision mechanisms 23
2.9 Total collision efficiency 23
2.10 Collision efficiency number of collisions for 26 and 80 μm diameter droplets 25

3.1 Droplet characteristics in CLINCH 37
3.2 Measured charge on droplets 38
3.3 Frozen fraction using 200 and 400 nm silver iodide particles 39
3.4 Evolution frozen fraction with time 41
3.5 Calculed collision efficieny for different mechanisms 42
3.6 Temperature and RH_w dependence of thermophoresis 43
3.7 Charge dependence of electrophoresis 44
3.8 Calculated total collision efficiency and experimental collision efficiency 46
3.9 Collision efficiency for Ladino et al. (2011a) 47

4.1 Frozen fraction using 200 nm silver iodide particles 58
4.2 Frozen fraction using ATD particles 59
4.3 Frozen fraction using Kaolinite particles 60
4.4 Freezing efficiency for 200 nm silver iodide participles 62
4.5 Freezing efficiency for ATD participles 65
4.6 Freezing efficiency for kaolinite particles 66

A.1 Schematic of measurement of charge on droplet. 76

B.1 EDX image of the produced particle. 78

List of Tables

2.1 Differences between Ladino et al. (2011b) and this work 17

3.1 Dependency of collision efficiency on droplet diameter, particle density and atmospheric pressure 52

4.1 Instrument characteristics 58
4.2 Number of collisions for 200 nm silver iodide particles 62
4.3 Number of collisions for 800 nm particles with a 80 μm diameter droplet 64

B.1 List of symbols 79

References

Andronache, C.: Diffusion and electric charge contributions to below-cloud wet removal of atmospheric ultra-fine aerosol particles, J. Aero. Sci., 35, 1467 – 1482, doi:10.1016/j.jaerosci.2004.07.005, 2004.

Andronache, C., Grönholm, T., Laakso, L., Phillips, V., and Venäläinen, A.: Scavenging of ultrafine particles by rainfall at a boreal site: observations and model estimations, Atmos. Chem. Phys., 6, 4739–4754, doi:10.5194/acp-6-4739-2006, 2006.

Ansmann, A., Mattis, I., Mueller, D., Wandinger, U., Radlach, M., Althausen, D., and Damoah, R.: Ice formation in Saharan dust over central Europe observed with temperature/humidity/aerosol Raman lidar, J. Geophys. Res., 110, n/a–n/a, URL http://dx.doi.org/10.1029/2004JD005000, 2005.

Ansmann, A., Tesche, M., Seifert, P., Althausen, D., Engelmann, R., Fruntke, J., Wandinger, U., Mattis, I., and Müller, D.: Evolution of the ice phase in tropical altocumulus: SAMUM lidar observations over Cape Verde, J. Geophys. Res., 114, n/a–n/a, URL http://dx.doi.org/10.1029/2008JD011659, 2009.

Ardon-Dryer, K., Huang, Y.-W., and Cziczo, D. J.: Laboratory studies of collection efficiency of sub-micrometer aerosol particles by cloud droplets on a single droplet basis, Atmos. Chem. Phys. Discuss., 15, 6207–6236, doi:10.5194/acpd-15-6207-2015, 2015.

Atkinson, J. D., Murray, B. J., Woodhouse, M. T., Whale, T. F., Baustian, K. J., Carslaw, K. S., Dobbie, S., O/'Sullivan, D., and Malkin, T. L.: The importance of feldspar for ice nucleation by mineral dust in mixed-phase clouds, Nature, pp. –, URL http://dx.doi.org/10.1038/nature12278, 2013.

Bae, S. Y., Jung, C. H., and Kim, Y. P.: Relative contributions of individual phoretic effect in the below-cloud scavenging process, J.Aero. Sci., 40, 621 – 632, doi:10.1016/j.jaerosci.2009.03.003, 2009.

Barlow, A. K. and Latham, J.: A laboratory study of the scavenging of sub-micron aerosol by charged raindrops, QJRMS, 109, 763–770, doi:10.1002/qj.49710946205, 1983.

Beard, K. V.: Experimental and Numerical Collision Efficiencies for Submicron Particles Scavenged by Small Raindrops, J. Atmos. Sci., 31, 1595–1603, doi:10.1175/1520-0469(1974)031⟨1595:

EANCEF⟩2.0.CO;2, 1974.

Billett, D., Hough, D., and Ottewill, R.: Studies on the contact angle of the charged silver iodide-solution-vapour interface, J. Electro.Chem.and Inter.l Electro., 74, 107 – 120, doi:http://dx.doi.org/10.1016/S0022-0728(76)80217-3, URL http://www.sciencedirect.com/science/article/pii/S0022072876802173, 1976.

Boucher, O.: Atmospheric Aerosols, in: Atmospheric Aerosols, pp. 9–24, Springer Netherlands, doi:10.1007/978-94-017-9649-1_2, URL http://dx.doi.org/10.1007/978-94-017-9649-1_2, 2015.

Broadley, S. L., Murray, B. J., Herbert, R. J., Atkinson, J. D., Dobbie, S., Malkin, T. L., Condliffe, E., and Neve, L.: Immersion mode heterogeneous ice nucleation by an illite rich powder representative of atmospheric mineral dust, Atmos. Chem. Phys., 12, 287–307, doi:10.5194/acp-12-287-2012, URL http://www.atmos-chem-phys.net/12/287/2012/, 2012.

Byrne, M. and Jennings, S.: Scavenging of sub-micrometre aerosol particles by water drops, Atmos. Env. A. General Topics, 27, 2099 – 2105, doi:http://dx.doi.org/10.1016/0960-1686(93)90039-2, 1993.

Cantrell, W. and Heymsfield, A.: Production of Ice in Tropospheric Clouds: A Review, Bull. Amer. Meteor. Soc., 86, 795–807, doi:10.1175/BAMS-86-6-795, URL http://dx.doi.org/10.1175/BAMS-86-6-795, 2005.

Chate, D. and Pranesha, T.: Field studies of scavenging of aerosols by rain events, J. Aero. Sci., 35, 695 – 706, doi:10.1016/j.jaerosci.2003.09.007, 2004.

Chate, D., Murugavel, P., Ali, K., Tiwari, S., and Beig, G.: Below-cloud rain scavenging of atmospheric aerosols for aerosol deposition models, Atmos. Res., 99, 528 – 536, doi:10.1016/j.atmosres.2010.12.010, 2011.

Conrad, P., Ewing, G. E., Karlinsey, R. L., and Sadtchenko, V.: Ice nucleation on BaF2(111), J. Chem. Phys., 122, 064709, doi:http://dx.doi.org/10.1063/1.1844393, URL http://scitation.aip.org/content/aip/journal/jcp/122/6/10.1063/1.1844393, 2005.

Cooper, W. A.: A Possible Mechanism for Contact Nucleation, J. Atmos. Sci., 31, 1832–1837, doi:10.1175/1520-0469(1974)031⟨1832:APMFCN⟩2.0.CO;2, URL http://dx.doi.org/10.1175/1520-0469(1974)031<1832:APMFCN>2.0.CO;2, 1974.

Croft, B., Lohmann, U., Martin, R. V., Stier, P., Wurzler, S., Feichter, J., Hoose, C., Heikkilä, U., van Donkelaar, A., and Ferrachat, S.: Influences of in-cloud aerosol scavenging parameterizations on aerosol concentrations and wet deposition in ECHAM5-HAM, Atmos. Chem. Phys., 10, 1511–1543, doi:10.5194/acp-10-1511-2010, 2010.

Croteau, T., Bertram, A. K., and Patey, G. N.: Adsorption and Structure of Water on Kaolinite Surfaces: Possible Insight into lee Nucleation from Grand Canonical Monte Carlo Calculations, J. Phys., 112, 10 708–10 712, URL <GotoISI>://000260357600002, 2008.

Croteau, T., Bertram, A. K., and Patey, G. N.: Water Adsorption on Kaolinite Surfaces Containing Trenches, J. Phys. Chem. A, 114, 2171–2178, doi:10.1021/jp910045u, URL http://dx.doi.org/10.1021/jp910045u, pMID: 20085249, 2010.

Davenport, H. and Peters, L. K.: Field studies of atmospheric particulate concentration changes during precipitation, Atmos. Env., 12, 997–1008, doi:10.1016/0004-6981(78)90344-X, 1978.

DeMott, P.: Quantitative descriptions of ice formation mechanisms of silver iodide-type aerosols, Atmos. Res., 38, 63–99, URL http://www.sciencedirect.com/science/article/pii/016980959400088U, 1995.

DeMott, P. J., Prenni, A. J., Liu, X., Kreidenweis, S. M., Petters, M. D., Twohy, C. H., Richardson, M. S., Eidhammer, T., and Rogers, D. C.: Predicting global atmospheric ice nuclei distributions and their impacts on climate, PNAS, 107, 11 217–11 222, URL http://www.pnas.org/content/107/25/11217.abstract, 2010.

Diehl, K. and Mitra, S.: A laboratory study of the effects of a kerosene-burner exhaust on ice nucleation and the evaporation rate of ice crystals, Atmos. Env., 32, 3145–3151, URL http://www.sciencedirect.com/science/article/pii/S1352231097004676, 1998.

Diehl, K., Matthias-Maser, S., Jaenicke, R., and Mitra, S.: The ice nucleating ability of pollen:: Part II. Laboratory studies in immersion and contact freezing modes, Atmos. Res., 61, 125–133, URL http://www.sciencedirect.com/science/article/pii/S0169809501001326, 2002.

Djikaev, Y. S. and Ruckenstein, E.: Thermodynamics of Heterogeneous Crystal Nucleation in Contact and Immersion Modes, J. Phys. Chem. A, 112, 11 677–11 687, doi:10.1021/jp803155f, URL http://dx.doi.org/10.1021/jp803155f, 2008.

Durant, A. J. and Shaw, R. A.: Evaporation freezing by contact nucleation inside-out, Geophys. Res.Lett., 32, L20 814, doi:10.1029/2005GL024175, 2005.

Fornea, A. P., Brooks, S. D., Dooley, J. B., and Saha, A.: Heterogeneous freezing of ice on atmospheric aerosols containing ash, soot, and soil, J. Geophys.Res.: Atmos., 114, n/a–n/a, doi:10.1029/2009JD011958, URL http://dx.doi.org/10.1029/2009JD011958, d13201, 2009.

Foss, J., Frey, M., Schamberger, M., Peters, J., and Leong, K.: Collection of uncharged prolate spheroidal aerosol particles by spherical collectors: 2D motion, J. Aero. Sci., 20, 515 – 532, doi:10.1016/0021-8502(89)90098-0, 1989.

Fukuta, N.: A Study of the Mechanism of Contact Ice Nucleation, J. Atmos. Sci., 32, 1597–1603, doi:10.1175/1520-0469(1975)032⟨1597:ASOTMO⟩2.0.CO;2, URL http://dx.doi.org/10.1175/

1520-0469(1975)032<1597:ASOTMO>2.0.CO;2, 1975a.

Fukuta, N.: Comments on "A Possible Mechanism for Contact Nucleation", J. Atmos. Sci., 32, 2371–2373, doi:10.1175/1520-0469(1975)032⟨2371:COPMFC⟩2.0.CO;2, URL http://dx.doi.org/10.1175/1520-0469(1975)032<2371:COPMFC>2.0.CO;2, 1975b.

Gokhale, N. and Goold, J. J.: Droplet freezing by surface nculceation, J. Appl. Meteor, 7, 870–874, 1968.

Gokhale, N. R. and Lewinter, O.: Microcinematographic Studies of Contact Nucleation, J. Appl. Meteor., 10, 469–473, doi:10.1175/1520-0450(1971)010⟨0469:MSOCN⟩2.0.CO;2, URL http://dx.doi.org/10.1175/1520-0450(1971)010<0469:MSOCN>2.0.CO;2, 1971.

Gokhale, N. R. and Spengler, J. D.: Freezing of Freely Suspended, Supercooled Water Drops by Contact Nucleation, J. Appl. Meteor., 11, 157–160, doi:10.1175/1520-0450(1972)011⟨0157:FOFSSW⟩2.0.CO;2, URL http://dx.doi.org/10.1175/1520-0450(1972)011<0157:FOFSSW>2.0.CO;2, 1972.

Greenfield, S. M.: Rain scavenging of radioactive particulate matter from the atmopshere, J. Meteor., 14, 115–125, doi:10.1175/1520-0469(1957)014⟨0115:RSORPM⟩2.0.CO;2, 1957.

Gurganus, C., Kostinski, A. B., and Shaw, R. A.: Fast Imaging of Freezing Drops: No Preference for Nucleation at the Contact Line, J. Phys. Chem. Lett., 2, 1449–1454, doi:10.1021/jz2004528, URL http://dx.doi.org/10.1021/jz2004528, 2011.

Gurganus, C., Kostinski, A. B., and Shaw, R. A.: High-Speed Imaging of Freezing Drops: Still No Preference for the Contact Line, J. Phys. Chem. C, 117, 6195–6200, doi:10.1021/jp311832d, URL http://dx.doi.org/10.1021/jp311832d, 2013.

Gurganus, C. W., Charnawskas, J. C., Kostinski, A. B., and Shaw, R. A.: Nucleation at the Contact Line Observed on Nanotextured Surfaces, Phys. Rev. Lett., 113, 235 701, doi:10.1103/PhysRevLett.113.235701, URL http://link.aps.org/doi/10.1103/PhysRevLett.113.235701, 2014.

Hinds, W.: Aerosol Technology: Properties, Behavior, and Measurement of Airborne Particles, Wiley, URL https://books.google.ch/books?id=qIkyjPXfWK4C, 2012.

Hiranuma, N., Augustin-Bauditz, S., Bingemer, H., Budke, C., Curtius, J., Danielczok, A., Diehl, K., Dreischmeier, K., Ebert, M., Frank, F., Hoffmann, N., Kandler, K., Kiselev, A., Koop, T., Leisner, T., Möhler, O., Nillius, B., Peckhaus, A., Rose, D., Weinbruch, S., Wex, H., Boose, Y., DeMott, P. J., Hader, J. D., Hill, T. C. J., Kanji, Z. A., Kulkarni, G., Levin, E. J. T., McCluskey, C. S., Murakami, M., Murray, B. J., Niedermeier, D., Petters, M. D., O'Sullivan, D., Saito, A., Schill, G. P., Tajiri, T., Tolbert, M. A., Welti, A., Whale, T. F., Wright, T. P., and Yamashita, K.: A comprehensive laboratory study on the immersion freezing behavior of illite NX particles: a com-

parison of 17 ice nucleation measurement techniques, Atmos. Chem. Phys., 15, 2489–2518, doi:10.5194/acp-15-2489-2015, URL http://www.atmos-chem-phys.net/15/2489/2015/, 2015.

Hobbs, P. V. and Rangno, A. L.: Ice Particle Concentrations in Clouds, J. Atmos. Sci., 42, 2523–2549, doi:10.1175/1520-0469(1985)042⟨2523:IPCIC⟩2.0.CO;2, URL http://dx.doi.org/10.1175/1520-0469(1985)042<2523:IPCIC>2.0.CO;2, 1985.

Hoffmann, N., Duft, D., Kiselev, A., and Leisner, T.: Contact freezing efficiency of mineral dust aerosols studied in an electrodynamic balance: quantitative size and temperature dependence for illite particles, Faraday Discuss., pp. –, doi:10.1039/C3FD00033H, URL http://dx.doi.org/10.1039/C3FD00033H, 2013a.

Hoffmann, N., Kiselev, A., Rzesanke, D., Duft, D., and Leisner, T.: Experimental quantification of contact freezing in an electrodynamic balance, Atmospheric Measurement Techniques Discussions, 6, 3407–3437, doi:10.5194/amtd-6-3407-2013, URL http://www.atmos-meas-tech-discuss.net/6/3407/2013/, 2013b.

Holownia, D., Kwiatkowska, I., and Hupka, J.: An investigation on wetting of porous materials., Physicochemical Problems of Mineral Processing, 42, 251–262, 2008.

Hoose, C. and Möhler, O.: Heterogeneous ice nucleation on atmospheric aerosols: a review of results from laboratory experiments, Atmos. Chem. Phys., 12, 9817–9854, doi:10.5194/acp-12-9817-2012, URL http://www.atmos-chem-phys.net/12/9817/2012/, 2012.

Hoose, C., Lohmann, U., Erdin, R., and Tegen, I.: The global influence of dust mineralogical composition on heterogeneous ice nucleation in mixed-phase clouds, Environmental Research Letters, 3, 025 003, doi:10.1088/1748-9326/3/2/025003, 2008.

Hoose, C., Kristjaensson, J. E., Chen, J.-P., and Hazra, A.: A Classical-Theory-Based Parameterization of Heterogeneous Ice Nucleation by Mineral Dust, Soot, and Biological Particles in a Global Climate Model, J. Atmos. Sci., 67, 2483–2503, doi:10.1175/2010JAS3425.1, URL http://dx.doi.org/10.1175/2010JAS3425.1, 2010.

Hu, X. L. and Michaelides, A.: Ice formation on kaolinite: Lattice match or amphoterism?, Surface Science, 601, 5378 – 5381, doi:http://dx.doi.org/10.1016/j.susc.2007.09.012, URL http://www.sciencedirect.com/science/article/pii/S0039602807008692, 2007.

Hu, X. L. and Michaelides, A.: Water on the hydroxylated (0 0 1) surface of kaolinite: From monomer adsorption to a flat 2D wetting layer, Surface Science, 602, 960–974, URL http://www.sciencedirect.com/science/article/pii/S0039602807012484, 2008.

Ickes, L., Welti, A., Hoose, C., and Lohmann, U.: Classical nucleation theory of homogeneous freezing of water: thermodynamic and kinetic parameters, Phys. Chem. Chem. Phys., pp. –, doi:10.1039/C4CP04184D, URL http://dx.doi.org/10.1039/C4CP04184D, 2015.

IPCC: Climate Change 2013: The Physical Science Basis. Contribution of Working Group I to the Fifth Assessment Report of the Intergovernmental Panel on Climate Change, Cambridge University Press, Cambridge, United Kingdom and New York, NY, USA, doi:10.1017/CBO9781107415324, URL www.climatechange2013.org, 2013.

Kandler, K., Lieke, K., Benker, N., Emmel, C., Kuepper, M., Mueller-Ebert, D., Ebert, M., Scheuvens, D., Schladitz, A., Schuetz, L., and Weinbruch, S.: Electron microscopy of particles collected at Praia, Cape Verde, during the Saharan Mineral Dust Experiment: particle chemistry, shape, mixing state and complex refractive index, Tellus B, 63, 2011.

Koretsky, C. M., Sverjensky, D. A., Salisbury, J. W., and D'Aria, D. M.: Detection of surface hydroxyl species on quartz, Gamma alumina, and feldspars using diffuse reflectance infrared spectroscopy, Geochimica et Cosmochimica Acta, 61, 2193–2210, doi:10.1016/S0016-7037(97)00056-2, URL http://www.sciencedirect.com/science/article/pii/S0016703797000562, 1997.

Kulkarni, P., Baron, P., and Willeke, K.: Aerosol Measurement: Principles, Techniques, and Applications, Wiley, URL https://books.google.ch/books?id=ETvXooNW4-EC, 2011.

Laakso, L., Groenholm, T., Rannik, U., Kosmale, M., Fiedler, V., Vehkamaeki, H., and Kulmala, M.: Ultrafine particle scavenging coefficients calculated from 6 years field measurements, Atmospheric Environment, 37, 3605 – 3613, doi:10.1016/S1352-2310(03)00326-1, 2003.

Ladino, L.: Experiemntal study on collection efficiency and conatact freezing of aerosols in a new collision chamber, Ph.D. thesis, ETH, Zuerich, Switzerland, 2011.

Ladino, L., Stetzer, O., Hattendorf, B., Guenther, D., Croft, B., and Lohmann, U.: Experimental Study of Collection Efficiencies between Submicron Aerosols and Cloud Droplets, J. Atmos. Sci., 68, 1853–1864, doi:10.1175/JAS-D-11-012.1, 2011a.

Ladino, L., Stetzer, O., Luend, F., Welti, A., and Lohmann, U.: Contact freezing experiments of kaolinite particles with cloud droplets, J. Geophys. Res., 116, n/a–n/a, URL http://dx.doi.org/10.1029/2011JD015727, 2011b.

Ladino Moreno, L. A., Stetzer, O., and Lohmann, U.: Contact freezing: a review of experimental studies, Atmos. Chem. Phys., 13, 9745–9769, doi:10.5194/acp-13-9745-2013, 2013.

Lai, K.-Y., Dayan, N., and Kerker, M.: Scavenging of Aerosol Particles by a Falling Water Drop, J. Atmos. Sci., 35, 674–682, doi:10.1175/1520-0469(1978)035⟨0674:SOAPBA⟩2.0.CO;2, 1978.

Leong, K. H., Beard, K. V., and Ochs, H. T.: Laboratory Measurements of Particle Capture by Evaporating Cloud Drops, J. Atmos. Sci., 39, 1130–1140, doi:10.1175/1520-0469(1982)039⟨1130:LMOPCB⟩2.0.CO;2, 1982.

Leong, K. H., Beard, K. V., and Stukel, J. J.: The Collision of Nonspherical Aerosol Particles with Small Evaporating Water Drops, Aerosol Science and Technology, 4, 445–454, doi:

10.1080/02786828508959069, 1985.

Levin, Z. and Yankofsky, S. A.: Contact Versus Immersion Freezing of Freely Suspended Droplets by Bacterial Ice Nuclei, J. Climate Appl. Meteor., 22, 1964–1966, doi: 10.1175/1520-0450(1983)022⟨1964:CVIFOF⟩2.0.CO;2, URL http://dx.doi.org/10.1175/1520-0450(1983)022<1964:CVIFOF>2.0.CO;2, 1983.

Lohmann, U.: A glaciation indirect aerosol effect caused by soot aerosols, Geophys. Res. Lett., 29, 11–1–11–4, URL http://dx.doi.org/10.1029/2001GL014357, 2002.

Lohmann, U. and Diehl, K.: Sensitivity Studies of the Importance of Dust Ice Nuclei for the Indirect Aerosol Effect on Stratiform Mixed-Phase Clouds, J. Atmos. Sci., 63, 968–982, doi: 10.1175/JAS3662.1, 2006.

Lohmann, U. and Feichter, J.: Indirect aerosol effects: a review, Atmos. Chem. Phys., 5, 715 – 737, 2005.

Lohmann, U. and Hoose, C.: Sensitivity studies of different aerosol indirect effects in mixed-phase clouds, Atmos. Chem. Phys., 9, 8917–8934, doi:10.5194/acp-9-8917-2009, 2009.

Lohmann, U., Lüönd, F., and Fabian, M.: An introduction to clouds: from the microscale to climate, Cambridge University Press, 2016.

Lüönd, F., Stetzer, O., Welti, A., and Lohmann, U.: Experimental study on the ice nucleation ability of size-selected kaolinite particles in the immersion mode, Journal of Geophysical Research: Atmospheres, 115, n/a–n/a, doi:10.1029/2009JD012959, 2010.

Marcolli, C., Gedamke, S., Peter, T., and Zobrist, B.: Efficiency of immersion mode ice nucleation on surrogates of mineral dust, Atmos. Chem. Phys., 7, 5081–5091, doi:10.5194/acp-7-5081-2007, URL http://www.atmos-chem-phys.net/7/5081/2007/, 2007.

Marcolli, C., Nagare, B., Welti, A., and Lohmann, U.: Ice nucleation efficiency of silver iodide: review and new insights, In preparation for ACPD, 2016.

Maria, S. F. and Russell, L. M.: Organic and Inorganic Aerosol Below-Cloud Scavenging by Suburban New Jersey Precipitation, Environmental Science & Technology, 39, 4793–4800, doi: 10.1021/es0491679, pMID: 16053076, 2005.

Maring, H., Savoie, D. L., Izaguirre, M. A., Custals, L., and Reid, J. S.: Mineral dust aerosol size distribution change during atmospheric transport, J. Geophys. Res., 108, 8592–, URL http://dx.doi.org/10.1029/2002JD002536, 2003.

Murray, B. J., O'Sullivan, D., Atkinson, J. D., and Webb, M. E.: Ice nucleation by particles immersed in supercooled cloud droplets, Chem. Soc. Rev., 41, 6519–6554, doi:10.1039/C2CS35200A, URL http://dx.doi.org/10.1039/C2CS35200A, 2012.

Nagare, B., Marcolli, C., Stetzer, O., and Lohmann, U.: Comparison of measured and calculated collision efficiencies at low temperatures, Atmos. Chem. Phys., 15, 13 759–13 776, doi:10.5194/acp-15-13759-2015, URL http://www.atmos-chem-phys.net/15/13759/2015/, 2015a.

Nagare, B., Marcolli, C., Welti, A., Stetzer, O., and Lohmann, U.: Comparing contact and immersion freezing from continuous flow diffusion chamber, submitted to ACPD, 2015b.

Nicolet, M., Stetzer, O., Lüönd, F., Möhler, O., and Lohmann, U.: Single ice crystal measurements during nucleation experiments with the depolarization detector IODE, Atmos. Chem. Phys., 10, 313–325., 2010.

Niedermeier, D., Hartmann, S., Shaw, R. A., Covert, D., Mentel, T. F., Schneider, J., Poulain, L., Reitz, P., Spindler, C., Clauss, T., Kiselev, A., Hallbauer, E., Wex, H., Mildenberger, K., and Stratmann, F.: Heterogeneous freezing of droplets with immersed mineral dust particles - measurements and parameterization, Atmos. Chem. Phys., 10, 3601–3614, doi:10.5194/acp-10-3601-2010, URL http://www.atmos-chem-phys.net/10/3601/2010/, 2010.

Niehaus, J. and Cantrell, W.: Contact freezing of water by salts, J. Phys.Chem. Lett., 6, 3490–3495, doi:10.1021/acs.jpclett.5b01531, URL http://dx.doi.org/10.1021/acs.jpclett.5b01531, pMID: 26291340, 2015.

Niehaus, J., Becker, J., Kostinski, A., and Cantrell, W.: Laboratory measurements of contact freezing by dust and bacteria at temperatures of mixed phase clouds, J. Atmos. Sci., pp. –, doi:10.1175/JAS-D-14-0022.1, URL http://dx.doi.org/10.1175/JAS-D-14-0022.1, 2014.

Ovchinnikov, M., Korolev, A., and Fan, J.: Effects of ice number concentration on dynamics of a shallow mixed-phase stratiform cloud, J. Geophys. Res., 116, n/a–n/a, URL http://dx.doi.org/10.1029/2011JD015888, 2011.

Park, S., Jung, C., Jung, K., Lee, B., and Lee, K.: Wet scrubbing of polydisperse aerosols by freely falling droplets, Journal of Aerosol Science, 36, 1444 – 1458, doi:10.1016/j.jaerosci.2005.03.012, 2005.

Philips, V. T. J., Donner, L. J., and Garner, S. T.: Nucleation Processes in Deep Convection Simulated by a Cloud-System-Resolving Model with Double-Moment Bulk Microphysics, J. Atmos. Sci., 64, 738–761, doi:10.1175/JAS3869.1, URL http://dx.doi.org/10.1175/JAS3869.1, 2007.

Pinti, V., Marcolli, C., Zobrist, B., Hoyle, C. R., and Peter, T.: Ice nucleation efficiency of clay minerals in the immersion mode, Atmospheric Chemistry and Physics, 12, 5859–5878, doi:10.5194/acp-12-5859-2012, URL http://www.atmos-chem-phys.net/12/5859/2012/, 2012.

Pitter, R. L. and Pruppacher, H. R.: A wind tunnel investigation of freezing of small water drops falling at terminal velocity in air, Q.J.R. Meteorol. Soc., 99, 540–550, URL http://dx.doi.org/10.1002/qj.49709942111, 1973.

Prodi, F., Santachiara, G., Belosi, F., Vedernikov, A., and Balapanov, D.: Phoretic forces on aerosol particles surrounding an evaporating droplet in microgravity conditions, Atmospheric Research, 142, 40 – 44, doi:10.1016/j.atmosres.2013.09.001, the 16th International Conference on Clouds and Precipitation, 2014.

Pruppacher, H. R. and Klett, J. D.: Microphysics of Clouds and Precipitation., Kluwer : Dordrecht, The Netherlands, 1997.

Radke, L. F., Hobbs, P. V., and Eltgroth, M. W.: Scavenging of Aerosol Particles by Precipitation, J. Appl. Meteor., 19, 715–722, doi:10.1175/1520-0450(1980)019⟨0715:SOAPBP⟩2.0.CO;2, 1980.

Rau, W.: Ueber die Wirkungsweise der Gefrierkerne im unterkuehlten Wasser, Zeitschrift fuer Naturforschung, 5, 667–675, URL http://zfn.mpdl.mpg.de/data/Reihe_A/5/ZNA-1950-5a-0667.pdf, 1950.

Reid, E. A., Reid, J. S., Meier, M. M., Dunlap, M. R., Cliff, S. S., Broumas, A., Perry, K., and Maring, H.: Characterization of African dust transported to Puerto Rico by individual particle and size segregated bulk analysis, J. Geophys. Res., 108, URL http://dx.doi.org/10.1029/2002JD002935, 2003.

Rogers, D. C.: Development of a continuous flow thermal gradient diffusion chamber for ice nucleation studies, Atmospheric Research, 22, 149–181, doi:10.1016/0169-8095(88)90005-1, 1988.

Santachiara, G., Prodi, G., and Belosi, F.: A Review of Termo- and Diffusio-Phoresis in the Atmospheric Aerosol Scavenging Process. Part 1: Drop Scavenging, Atmospheric and Climate Sciences, 2, 148–158, doi:10.4236/acs.2012.22016, 2012.

Schuttlefield, J. D., Cox, D., and Grassian, V. H.: An investigation of water uptake on clays minerals using ATR-FTIR spectroscopy coupled with quartz crystal microbalance measurements, J. Geophys. Res., 112, n/a–n/a, URL http://dx.doi.org/10.1029/2007JD008973, 2007.

Sear, R. P.: Nucleation at contact lines where fluid fluid interfaces meet solid surfaces, Journal of Physics: Condensed Matter, 19, 466 106, URL http://stacks.iop.org/0953-8984/19/i=46/a=466106, 2007.

Seifert, P., Ansmann, A., Groeay, S., Freudenthaler, V., Heinold, B., Hiebsch, A., Mattis, I., Schmidt, J., Schnell, F., Tesche, M., Wandinger, U., and Wiegner, M.: Ice formation in ash-influenced clouds after the eruption of the Eyjafjallajakull volcano in April 2010, J. Geophys. Res., 116, n/a–n/a, URL http://dx.doi.org/10.1029/2011JD015702, 2011.

Seinfeld, J. H. and Pandis, S. N.: Atmospheric Chemistry and Physics: From Air Pollution to Climate Change:, John Wiley & Sons, Inc., 2006.

Seinfeld, J. H. and Pandis, S. N.: Atmospheric chemistry and physics: from air pollution to climate change, John Wiley & Sons, 2012.

Shang, J., Flury, M., Harsh, J. B., and Zollars, R. L.: Contact angles of aluminosilicate clays as affected by relative humidity and exchangeable cations, Colloids and Surfaces A: Physicochemical and Engineering Aspects, 353, 1–9, URL http://www.sciencedirect.com/science/article/pii/S0927775709006165, 2010.

Shaw, R. A., Durant, A. J., and Mi, Y.: Heterogeneous surface crystallization observed in undercooled water, J. Phy. Chem., 109(20), 9865–9868, 2005.

Slinn, W. G. N.: Precipitation scavenging, in: Atmospheric Sciences and Power Production, chap. 11, Division of Biomedical Environmental Research,U.S. Department of Energy, Washington DC, USA, 1983.

Slinn, W. G. N. and Hales, J. M.: A Reevaluation of the Role of Thermophoresis as a Mechanism of In- and Below-Cloud Scavenging, J. Atmos. Sci., 28, 1465–1471, doi:10.1175/1520-0469(1971)028⟨1465:AROTRO⟩2.0.CO;2, 1971.

Stetzer, O., Baschek, B., Lüönd, F., and Lohmann, U.: The Zurich Ice Nucleation Chamber (ZINC)-A New Instrument to Investigate Atmospheric Ice Formation, Aerosol Science and Technology, 42, 64–74, doi:10.1080/02786820701787944, 2008.

Suzuki, S., Nakajima, A., Yoshida, N., Sakai, M., Hashimoto, A., Kameshima, Y., and Okada, K.: Freezing of water droplets on silicon surfaces coated with various silanes, Chemical Physics Letters, 445, 37 – 41, doi:http://dx.doi.org/10.1016/j.cplett.2007.07.066, URL http://www.sciencedirect.com/science/article/pii/S0009261407010032, 2007.

Svensson, E. A., Delval, C., von Hessberg, P., Johnson, M. S., and Pettersson, J. B. C.: Freezing of water droplets colliding with kaolinite particles, Atmos. Chem. Phys., 9, 4295–4300, doi:10.5194/acp-9-4295-2009, URL http://www.atmos-chem-phys.net/9/4295/2009/, 2009.

Szyszka, D.: Study of conatact angle of liquid in solid surface and solid on liquid surface, Mining Science, 135, 131–146, doi:DOI:10.5277/gig121810, 2012.

Tabrizy, V. A., Hamouda, A. A., and Denoyel, R.: Influence of Magnesium and Sulfate Ions on Wettability Alteration of Calcite, Quartz, and Kaolinite: Surface Energy Analysis, Energy & Fuels, 25, 1667–1680, doi:10.1021/ef200039m, URL http://dx.doi.org/10.1021/ef200039m, 2011.

Tegen, I. and Schepanski, K.: The global distribution of mineral dust, in: IOP Conf. Ser.: Earth Environ. Sci. 7 012001, vol. 7, doi:10.1088/1755-1307/7/1/012001, 2009.

Tinsley, B. A.: Electric charge modulation of aerosol scavenging in clouds: Rate coefficients with Monte Carlo simulation of diffusion, J. Geophys. Res. Atmos., 115, doi:10.1029/2010JD014580, 2010.

Tinsley, B. A. and Leddon, D. B.: Charge modulation of scavenging in clouds: Extension of Monte Carlo simulations and initial parameterization, J. Geophys. Res. Atmos., 118, 8612–8624, doi:

10.1002/jgrd.50618, 2013.

Tinsley, B. A., Rohrbaugh, R. P., Hei, M., and Beard, K. V.: Effects of Image Charges on the Scavenging of Aerosol Particles by Cloud Droplets and on Droplet Charging and Possible Ice Nucleation Processes, J. Atmos. Sci., 57, 2118–2134, doi:10.1175/1520-0469(2000)057⟨2118:EOICOT⟩2.0.CO;2, 2000.

Tinsley, B. A., Zhou, L., and Plemmons, A.: Changes in scavenging of particles by droplets due to weak electrification in clouds, Atmospheric Research, 79, 266 – 295, doi:10.1016/j.atmosres.2005.06.004, 2006a.

Tinsley, B. A., Zhou, L., and Plemmons, A.: Changes in scavenging of particles by droplets due to weak electrification in clouds, Atmospheric Research, 79, 266–295, doi:10.1016/j.atmosres.2005.06.004, 2006b.

Tobo, Y., DeMott, P. J., Raddatz, M., Niedermeier, D., Hartmann, S., Kreidenweis, S. M., Stratmann, F., and Wex, H.: Impacts of chemical reactivity on ice nucleation of kaolinite particles: A case study of levoglucosan and sulfuric acid, Geophysical Research Letters, 39, doi:10.1029/2012GL053007, URL http://dx.doi.org/10.1029/2012GL053007, 2012.

Twohy, C. H., DeMott, P. J., Pratt, K. A., Subramanian, R., Kok, G. L., Murphy, S. M., Lersch, T., Heymsfield, A. J., Wang, Z., Prather, K. A., and Seinfeld, J. H.: Relationships of Biomass-Burning Aerosols to Ice in Orographic Wave Clouds, J. Atmos. Sci., 67, 2437–2450, doi:10.1175/2010JAS3310.1, URL http://dx.doi.org/10.1175/2010JAS3310.1, 2010.

Twomey, S.: Pollution and the planetary albedo, Atmospheric Environment (1967), 8, 1251 – 1256, doi:http://dx.doi.org/10.1016/0004-6981(74)90004-3, URL http://www.sciencedirect.com/science/article/pii/0004698174900043, 1974.

Ulmke, H., Wriedt, T., and Bauckhage, K.: Piezoelectric Droplet Generator for the Calibration of Particle-Sizing Instruments, Chemical Engineering & Technology, 24, 265–268, doi:10.1002/1521-4125(200103)24:3⟨265::AID-CEAT265⟩3.0.CO;2-4, 2001.

Šolc, R., Gerzabek, M. H., Lischka, H., and Tunega, D.: Wettability of kaolinite (001) surfaces Molecular dynamic study, Geoderma, 169, 47–54, URL http://www.sciencedirect.com/science/article/pii/S0016706111000401, 2011.

Vali, G.: Nucleation terminology, Journal of Aerosol Science, 16, 575 – 576, doi:http://dx.doi.org/10.1016/0021-8502(85)90009-6, URL http://www.sciencedirect.com/science/article/pii/0021850285900096, 1985.

Vonnegut, B.: Nucleation of Supercooled Water Clouds by Silver Iodide Smokes., Chemical Reviews, 44, 277–289, doi:10.1021/cr60138a003, URL http://dx.doi.org/10.1021/cr60138a003, pMID: 18140559, 1949.

Wang, P. K. and Pruppacher, H. R.: An Experimental Determination of the Efficiency with Which Aerosol Particles are Collected by Water Drops in Subsaturated Air, J. Atmos. Sci., 34, 1664–1669, doi:10.1175/1520-0469(1977)034⟨1664:AEDOTE⟩2.0.CO;2, 1977.

Wang, P. K., Grover, S. N., and Pruppacher, H. R.: On the Effect of Electric Charges on the Scavenging of Aerosol Particles by Clouds and Small Raindrops, J. Atmos. Sci., 35, 1735–1743, doi:10.1175/1520-0469(1978)035⟨1735:OTEOEC⟩2.0.CO;2, 1978.

Wang, X., Zhang, L., and Moran, M. D.: Uncertainty assessment of current size-resolved parameterizations for below-cloud particle scavenging by rain, Atmos. Chem. Phys., 10, 5685–5705, doi:10.5194/acp-10-5685-2010, 2010.

Welti, A., Lüönd, F., Kanji, Z. A., Stetzer, O., and Lohmann, U.: Time dependence of immersion freezing: an experimental study on size selected kaolinite particles, Atmos. Chem. Phys., 12, 9893–9907, doi:10.5194/acp-12-9893-2012, 2012.

Wex, H., DeMott, P. J., Tobo, Y., Hartmann, S., Rösch, M., Clauss, T., Tomsche, L., Niedermeier, D., and Stratmann, F.: Kaolinite particles as ice nuclei: learning from the use of different kaolinite samples and different coatings, Atmos. Chem. Phys., 14, 5529–5546, doi:10.5194/acp-14-5529-2014, URL http://www.atmos-chem-phys.net/14/5529/2014/, 2014.

Young, K. C.: The Role of Contact Nucleation in Ice Phase Initiation in Clouds, J. Atmos. Sci., 31, 768–776, doi:10.1175/1520-0469(1974)031⟨0768:TROCNI⟩2.0.CO;2, 1974.

Yun, Y. and Penner, J. E.: Global model comparison of heterogeneous ice nucleation parameterizations in mixed phase clouds, J. Geophys. Res. Atmos., 117, n/a–n/a, doi:10.1029/2011JD016506, 2012.

Zhou, L., Tinsley, B. A., and Plemmons, A.: Scavenging in weakly electrified saturated and subsaturated clouds, treating aerosol particles and droplets as conducting spheres, J. Geophys. Res. Atmos., 114, n/a–n/a, doi:10.1029/2008JD011527, 2009.

Zielke, S. A., Bertram, A. K., and Patey, G. N.: Simulations of Ice Nucleation by Kaolinite (001) with Rigid and Flexible Surfaces, The Journal of Physical Chemistry B, 0, null, doi:10.1021/acs.jpcb.5b09052, URL http://dx.doi.org/10.1021/acs.jpcb.5b09052, pMID: 26524230, 0.

Zobrist, B., Koop, T., Luo, B. P., Marcolli, C., and Peter, T.: Heterogeneous Ice Nucleation Rate Coefficient of Water Droplets Coated by a Nonadecanol Monolayer, J. Phys. Chem. C, 111, 2149–2155, doi:10.1021/jp066080w, URL http://dx.doi.org/10.1021/jp066080w, 2007.

Acknowledgements

Firstly, I would like to express my gratitude to Prof. Ulrike Lohmann, Dr. Claudia Marcolli and Dr. Olaf Stetzer for giving me a chance to work for my Ph.D. here at IAC, ETH and for their support. I would like to thank especially Claudia for accepting to supervise my work after Olaf left the institute, her patience, motivation and insightful ideas. Her guidance helped me in writing my thesis and I could not have imagined having better supervisor.

My special thanks goes to Zamin Kanji, Andre Welti and Joel Corbin for helping me in my initial stages in lab and for stimulating discussions all this time. I thank my officemate Jan Henneberger being patience with my questions which annoyed him sometimes. My special thanks to Luisa Ickes for reading introduction chapter and abstract translation to German. I thank my fellow colleagues, Monika Kohn, Yvonne Boose, James Atkinson, Lukas Kauffmann, Anand kumar and group members, for insightful discussions and their inputs on my work. I also want to thank all my group member where they kept their patience while talking to me which can be easily be perceived as impolite. I assure, that was never the intension. I should specially acknowledge Hannes Wydler and Peter Isler for their machine workshop and IT support and Eva Choffat for her administrative support.

I would like to thank P. Pradeep Kumar, Maheshkumar for the inspiration they gave me to pursue my Ph.D. I would like to thank Gokul, Preshanth, Malhar for their support though out this span and before that too. I would also like to thank Elizabeth Gusdek for giving me a home away from home.

Lastly, I would like to thank my parents, Bai and Appa, and family, for their sacrifices towards my education, without their support this would not have possible.

Curriculum vitae

Baban Nagare
born 9 Septrmber 1984, Sarole Thadi, Nashik, India
citizen of India

Education

09/2011 – present	Ph.D. at ETH Zurich, Switzerland
06/2005 – 05/2007	M.Sc. at University of Pune, Pune, India
06/2003 – 05/2005	B.Sc. at University of Pune, Pune, India

Professional Experience

06/2007 – 05/2009 Research assistant at University of Pune, Pune, India
07/2009 – 06/2011 Research assistant at Florida International University, Miami, Florida, USA

Conferences

Nagare, B., Marcolli, C.,Stetzer, O., Lohmann, U.: Freezing efficiency of silver Iodide, ATD and kaolinite in the contact freezing mode, EGU Vienna, 2014
Nagare, B., Stetzer, O., Lohmann, U.: Contact freezing of silver iodide and kaolinite particles, DACA, Davos, Switzerland. 2013
Nagare, B., Stetzer, O., Lohmann, U.: Comparing ice nucleation ability of different kaolinite types in the contact freezing mode, 16th International conference on clouds and precipitation, Leipzig, 2012

Publications

Marcolli, C., Nagare, B., Welti, A., Lohmann, U.: Ice nucleation efficiency of silver iodide: review and new insights, In preparation for ACPD

Nagare, B., Marcolli, C., Welti, A., Stetzer, O., Lohmann, U: Comparing contact and immersion freezing from continuous flow diffusion chamber, In preparation for ACPD
Nagare, B., Marcolli, C.,Stetzer, O., Lohmann, U.: Comparison of theoretical and experimental collision efficiency at low temperatures, Atm. Chem. and Phy, 2015
Patade, S, Nagare, B., Wagh, S., Maheshkumar, R., Prabha, T.V., Pradeep Kumar, P.: Deposition ice nuclei observations over the Indian region during CAIPEEX; Atmospheric Research, 2014